WARWICK
THE UNIVERSITY OF WARWICK

Library Declaration and Deposit Agreement

1. **STUDENT DETAILS**

   Panayiota Argyrou

   .....

2. **THESIS DEPOSIT**

   2.1 I understand that under my registration at the University, I am required to deposit my thesis with the University in BOTH hard copy and in digital format. The digital version should normally be saved as a single pdf file.

   2.2 The hard copy will be housed in the University Library. The digital version will be deposited in the Universitys Institutional Repository (WRAP). Unless otherwise indicated (see 2.3 below) this will be made openly accessible on the Internet and will be supplied to the British Library to be made available online via its Electronic Theses Online Service (EThOS) service. [At present, theses submitted for a Masters degree by Research (MA, MSc, LLM, MS or MMedSci) are not being deposited in WRAP and not being made available via EthOS. This may change in future.]

   2.3 In exceptional circumstances, the Chair of the Board of Graduate Studies may grant permission for an embargo to be placed on public access to the hard copy thesis for a limited period. It is also possible to apply separately for an embargo on the digital version. (Further information is available in the Guide to Examinations for Higher Degrees by Research.)

   2.4 (a) Hard Copy I hereby deposit a hard copy of my thesis in the University Library to be made publicly available to readers immediately.
   I agree that my thesis may be photocopied.

   (b) Digital Copy I hereby deposit a digital copy of my thesis to be held in WRAP and made available via EThOS.
   My thesis can be made publicly available online.

3. **GRANTING OF NON-EXCLUSIVE RIGHTS**

Whether I deposit my Work personally or through an assistant or other agent, I agree to the following: Rights granted to the University of Warwick and the British Library and the user of the thesis through this agreement are non-exclusive. I retain all rights in the thesis in its present version or future versions. I agree that the institutional repository administrators and the British Library or their agents may, without changing content, digitise and migrate the thesis to any medium or format for the purpose of future preservation and accessibility.

4. **DECLARATIONS**

(a) I DECLARE THAT:

- I am the author and owner of the copyright in the thesis and/or I have the authority of the authors and owners of the copyright in the thesis to make this agreement. Reproduction of any part of this thesis for teaching or in academic or other forms of publication is subject to the normal limitations on the use of copyrighted materials and to the proper and full acknowledgement of its source.
- The digital version of the thesis I am supplying is the same version as the final, hardbound copy submitted in completion of my degree, once any minor corrections have been completed.
- I have exercised reasonable care to ensure that the thesis is original, and does not to the best of my knowledge break any UK law or other Intellectual Property Right, or contain any confidential material.
- I understand that, through the medium of the Internet, files will be available to automated agents, and may be searched and copied by, for example, text mining and plagiarism detection software.

(b) IF I HAVE AGREED (in Section 2 above) TO MAKE MY THESIS PUBLICLY AVAILABLE DIGITALLY, I ALSO DECLARE THAT:

- I grant the University of Warwick and the British Library a licence to make available on the Internet the thesis in digitised format through the Institutional Repository and through the British Library via the EThOS service.
- If my thesis does include any substantial subsidiary material owned by third-party copyright holders, I have sought and obtained permission to include it in any version of my thesis available in digital format and that this permission encompasses the rights that I have granted to the University of Warwick and to the British Library.

5. **LEGAL INFRINGEMENTS**

I understand that neither the University of Warwick nor the British Library have any obligation to take legal action on behalf of myself, or other rights holders, in the event of infringement of intellectual property rights, breach of contract or of any other right, in the thesis.

Please sign this agreement and return it to the Graduate School Office when you submit your thesis.

Student's signature: .....Date: .....

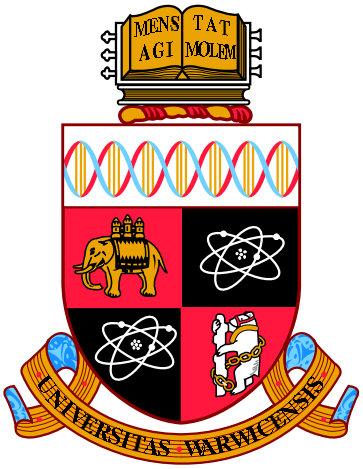

Investigation of Superconductivity in Non-centrosymmetric Compounds Nb_xRe_{1-x} in the range $0.22 \leq x \leq 0.34$.

by

Panayiota Argyrou

Thesis

Submitted to the University of Warwick

for the degree of

Master of Sciences

Physics Department

December 2016

Contents

List of Tables

List of Figures

Acknowledgments

I would like to thank some people who were connected to both the experimental investigations and the writing of this thesis. I truly believe that without their help, it could not be possible to complete this course. Firstly, I would like to thank my supervisors Geetha Balakrishnan and Martin Lees for co-supervising this project, providing me with support, guidance and their knowledge regarding the experimental research on superconductors. My previous knowledge expanded by learning new techniques and the necessary training on experimental instruments and software.

I would also like to separately thank Martin Lees for his help with performing laboratory measurements and for being able to answer questions on my research and also offering guidance when I struggled along the way. Special thanks to Paul Goddard for being my feedback supervisor and giving me his advice with any written document. A big thank you to Daniel Brunt and Monica Ciomaga Hatnean for giving me their valuable assistance with sample preparation and useful advice throughout the project. Additionally, thanks to Steve York for performing the EDAX measurements and Michael Smidman for allowing the use of his sample created during his Doctorate of Philosophy.

Thanks also to the other members of the Superconductivity and Magnetism Group, particularly to Simon Riberolles, Daniel Brunt and Natalia Parzyk-who I shared an office with- Talha Ahmad, Will Blackmore and Daniel Mayoh. I enjoyed being a part of this group. All of you made me feel welcome, shared your knowledge

with me and were a great group of people to work with.

The biggest thank you and appreciation goes to my family and friends for standing by my side through the good and bad moments during this year and have always encouraged me to keep going until the end. Lastly but not least, I would like to thank the two most important people in my life who have raised me with valuable morals which have made me a capable person to get through any obstacle in my way.

Mum and Dad, thank you for your love, care and patience, I hope I have made you proud!!!

This thesis is in memory of all young men who drove their motorbikes to heaven. I wish you were here to finish this together with me. Rest in Peace my friends...

Declarations

This thesis is submitted to the University of Warwick in support of my application for the degree of Masters of Sciences by Research. It has been written by me and has not been submitted in any previous application for any degree. All the work took place between October 2015 and September 2016. It was carried out by the author except in the cases outlined below.

All the polycrystalline samples of the compounds $Nb_{0.22}Re_{0.78}$ were prepared by me. All the polycrystalline samples of the compounds $Nb_{0.29}Re_{0.71}$ and $Nb_{0.34}Re_{0.66}$ were prepared by Dr. Michael Smidman during his Doctor of Philosophy. EDAX measurements of all the compounds were performed by Steve York at the University of Warwick. Powder x-ray diffraction measurements were performed with the help of Simon Riberolles and the analysis of the data collected was performed with the help of Daniel Brunt. The physical properties measurements were performed by myself at University of Warwick under the supervision of Dr. Martin Lees.

Abstract

In non-centrosymmetric superconductors, the lack of inversion symmetry along with anti-symmetric spin-orbit coupling, allow the Cooper pairs to be an admixture of spin-singlet and spin-triplet states. The Niobium-Rhenium system is interesting as it crystallizes in two different structures, the σ structure and the non-centrosymmetric α-Mn type. α-Mn structure has a homogeneity range of 0.38 to 0.13 Niobium. The Nb_xRe_{1-x} compounds have been investigated previously for $x =$ 0.18, 0.25, 0.29 and 0.31 with more in-depth research done on $Nb_{0.18}Re_{0.82}$. In this study, the superconductivity of non-centrosymmetric polycrystalline annealed and as-cast samples of Nb_xRe_{1-x} when $x = 0.22$, 0.29 and 0.34 were investigated using resistivity, magnetic susceptibility, magnetization and specific heat measurements of each composition as a function of temperature and applied field. The superconducting transition temperature, (T_c) is seen to decrease as x increases. The ρ(T) data exhibits metallic behaviour. The lower critical field, (B_{c1}) and the upper critical field, (B_{c2}) also decrease as x increases. These are used to determine κ, ξ and λ which indicate the materials are strong type-II superconductors. The critical fields observed in the annealed samples were higher than those observed in as-cast samples. The specific heat (C/T) measured on one of the samples, the as-cast polycrystalline $Nb_{0.22}Re_{0.78}$ sample demonstrates exponential behaviour at low temperatures and can not be fitted by one-gap BCS model. The Sommerfeld coefficient γ in the superconducting state shows a linear field dependence. Some observations indicate that the materials are type-II superconductors for Nb_xRe_{1-x} ($0.22 \leq x \leq 0.34$).

Chapter 1

Introduction

"*Superconductivity remains one of the most fascinating and intriguing phases of matter even a hundred years after its first observation.*" as Manfred Sigrist stated in 2011 [1]. Since the discovery of superconductivity in mercury in 1911 by the Dutch scientist Heike Kamerlingh Onnes, many other superconducting materials have been discovered and the theory of superconductivity has been developed. Superconductivity results from the condensation of pairs of electrons, bound by an attractive interaction [2, 3]. Superconductivity is the complete disappearance of electrical resistance in a substance below a particular temperature called the superconducting transition temperature, T_c and for a material to behave as a superconductor, low temperatures are usually required. After the discovery of the isotope effect [4, 5], the idea that the electron phonon interaction was responsible for the formation of the superconducting condensate, was strongly supported. The superconductivity of some materials with different isotopes of the element or one of the elements if it is a compound suggests that there is a change in the transition temperature associated with the increase in atomic mass [6, 7].

The description of superconductivity according to the microscopic theory of Bardeen, Cooper and Schrieffer (BCS) has been successfully used to explain the occurrence of superconductivity of many materials [8]. In this theory, key element is the pairing of electrons close to the Fermi level into Cooper pairs through interaction with the crystal lattice. An isotropic energy gap opens in the single particle excitation system as a result of the formation of the electron pairs in the spin singlet s-wave. In 1957 Matthias proposed a number of empirical rules that explained the variation of superconductivity in the elements and the alloys in the periodic table. This set of empirical rules explained the variation of transition temperatures (T_c) of elements

and alloys [9, 10]. These rules stated that superconductivity can be observed only for metallic systems and that the transition temperature (T_c) depends on the average number of valence electrons (z) and the electron density (N_e) in the solid. Elements for which $2 < z < 8$ or with z approximately 2 or slightly greater than 8 can be superconductors. Transition temperature increases for a given average number of valence electrons (z) as the power of the inter-electron spacing, r_s, increases. For metals with $z = 2$ or 8 these rules are not applied. It is important to note that some of these empirical rules have not been able to explain the superconductivity in some materials discovered since.

Superconductivity was reported in several non-centrosymmetric compounds with α-Mn and hexagonal structures [11]. Although, the crystal structure was considered to be less important in determining the superconducting properties, cubic or hexagonal structures were more preferable. After BCS theory was introduced, most of the Matthias rules could be explained using this theory [9].

1.1 Unconventional superconductivity

Conventional superconductors are materials that display superconductivity as described by BCS theory and they can be either type-I or type-II [12]. Superconductors can be penetrated by a strong magnetic field and a phenomenon called Meissner effect occurs when the magnetic flux is expelled from a superconductor during its transition to the superconducting state. When the applied magnetic field exceeds a certain value, superconductivity breaks down. In type-I superconductors, superconductivity is destroyed via a first order phase transition when the strength of the applied field rises above a critical value (B_c). This type of superconductivity is exhibited by pure metals like aluminium, zinc, tin etc. When a field is applied to a type-I superconductor and increased gradually, the magnetization increases linearly with the field up to a critical value, B_c as shown in the left side of fig. 1.1. The superconductor is in the superconducting state between zero and the critical field value and after this, it is in the normal state. The temperature dependence of the applied field for a type-I superconductor is shown in the right side of fig. 1.1. At zero temperature the applied field reaches the critical value, where in contrast at the transition temperature it reaches zero.

For type-II superconductors, there are two critical fields, the lower B_{c1} and the upper B_{c2}. These superconductors are characterized by the formation of magnetic

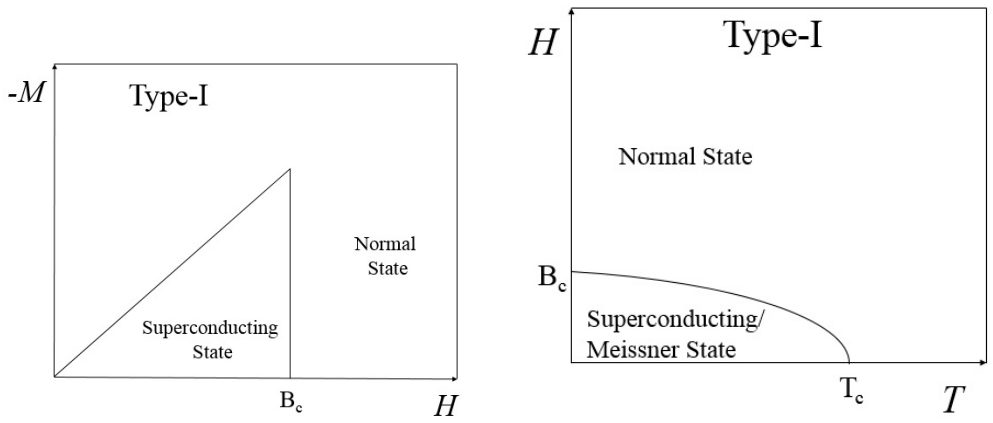

Figure 1.1: (a) Magnetization as a function of the applied field and (b) the applied field as a function of temperature for a type-I superconductor.

vortices in an applied magnetic field, which occurs above the lower critical field, B_{c1}. The vortex density increases as field strength increases and at a higher critical field, B_{c2}, superconductivity is destroyed as shown in fig. 1.2 (a) [13]. The magnetic flux is completely expelled only up to the lower critical field. Below B_{c1}, type-II superconductor shows the same behaviour as type-I superconductor below B_c. Type-II superconductors exhibit a partially completed Meissner effect. For applied fields greater than the lower critical field, B_{c1} the magnetic flux partially penetrates into the material up to the upper critical field, B_{c2}. Above this critical field and up to the upper critical field, B_{c2}, the superconductor is in the mixed state. Above B_{c1} and generally in the mixed state, there are superconducting vortices in the material. The temperature dependence of the applied field for a type-II superconductor is shown in fig. 1.2 (b). At zero temperature the applied field reaches a lower critical value, B_{c1} and decreases non-linearly as it approaches the transition temperature. As you can see in fig. 1.2, below the lower critical field the Meissner effect occurs. For applied fields above the upper critical field, the superconductor returns to the normal state. Most compounds and alloy superconductors are type-II materials.

The Ginzburg-Landau theory is based on a phenomenological order parameter [14], which can solve many problems including the spatial variation of the order parameter. Order parameter is usually considered as a variable which describes changes in temperature below a transition temperature or changes in magnetic field below a critical field. The success of BCS theory is based on a controlled expan-

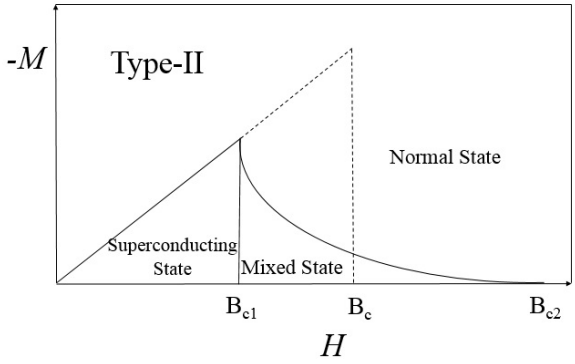

(a)

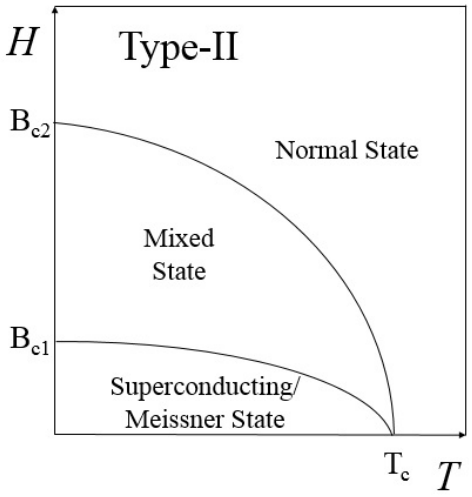

(b)

Figure 1.2: (a) The magnetization as a function of the applied field and (b) the temperature dependence of the applied field for a type-II superconductor.

sion of the electron-phonon interaction [15]. BCS theory introduced the concept of Cooper pairs [16]. In a Cooper pair, a weak attractive interaction between electrons could result in the formation of quasi-bound electron pairs. The existence of an energy gap can be explained using Cooper's suggestion [17]. Cooper pairs can be constructed in momentum space, where one pair relates an electron at $\mathbf{k}$ with its time reversed partner at $-\mathbf{k}$. In real space, pairs extend to a distance called coherence length. In momentum space, the formation of Cooper pairs exist in an energy shell close to the Fermi surface. The BCS theory is the heart of weak coupling field theory.

In the BCS theory the important mechanism is the electron-phonon interaction. An electron polarizes the surrounding lattice of phonons. The polarization continues as the electron moves away. Therefore, a second electron can move in the system and take the advantage of this attractive polarization. Ignoring the large Coulomb repulsion, the electrons can attract each other. The electrons can stay at the same position at different times which consequently predicts that the electrons are in an s-wave pair state. In that case, the large Coulomb repulsion is normalised to a smaller value when moving from an energy scale E_{F} (Fermi level energy) down to a scale $\hbar\omega_{\mathrm{D}}$ (ω_{D} is the Debye frequency) [18] allowing an overall attraction. This procedure limits transition temperature, T_{c}. In conventional superconductors, inversion symmetry is important for the formation of the Cooper pairs [4] due to an attractive interaction among electrons.

A superconducting function has both a spin and an orbital component. The spin component can be in a singlet state or in a triplet state. The Cooper pairs have opposite spin, $S = 0$ in a singlet state and same spin, $S = 1$ in a triplet state. The orbital component can have angular momentum $l = 0$ (s), $l = 1$ (p). An s-wave superconductor has an isotropic superconducting gap in all directions, Cooper pairs of opposite spin $S = 0$ and an orbital component of angular momentum $l = 0$. A p-wave superconductor has Cooper pairs of same spin $S = 1$ and an orbital component of angular momentum $l = 1$.

The superconductivity observed in the most superconductors before the discovery of the cuprate superconductors could be broadly explained by the electron-phonon coupling mechanism [1]. In 1963, Balian and Werthamer considered superconductors with non-zero angular momentum [19]. As a consequence, there is interest in the unconventional superconductivity which is condensation of Cooper pairs of lower symmetries. The term 'unconventional' indicates a pair state that is not isotropic s-wave state and/or where the interaction is different to the conventional electron-phonon interaction was described in the 1950s [20]. The strong coupling theory was developed by Schrieffer in order to describe pairing in some real systems [20]. The prediction of anomalies in tunnelling spectra produced by the frequency dependence of the pairing self-energy connected with phonons is the proof that conventional superconductivity is originated from the electron-phonon interaction [21]. Using this theory the superconducting transition temperatures could be estimated [22].

In 1987, superconductivity was observed in cuprates giving the requirement to include new mechanisms due to the high transition temperature observed in these materials [23]. Many classes of cuprates superconductors were investigated with high transition temperature [13, 12, 23]. The discovery of superconductivity in cuprates violates most of Matthias' rules. According to Scalapino, Cooper pairs can be found in the quasi-two-dimensional systems which are called spin singlet $d_{x^2-y^2}$ wave structures [24]. If the spins are aligned, there is no gain in the free energy by the Pauli exclusion principle. If the spins are anti-aligned, one of the spins can gain energy by virtual jumps. Superconductivity is also observed in electron doped cuprates [25]. The origin of superconductivity in the electron doped side is the same as the hole doped as the properties of the two are similar. The magnetic correlations are responsible for the pairing supported by the statement above. The crystal structure can have great influence on superconductivity, if inversion symmetry is missing. Inversion symmetry associated with the time reversal invariances plays an important role for Cooper pair formation [1]. Unconventional superconducting phases are responsible for the material disorder effect.

1.2 Non-centrosymmetric superconductors

Superconductors without inversion symmetry in their crystal structure are called non-centrosymmetric superconductors (NCS) [26]. The lack of inversion symmetry in a crystal structure can influence superconductivity. The non-centrosymmetric superconductors can break the gauge symmetry due to electrons pairing but also inversion symmetry, which allows several physical effects that were previously forbidden. A variety of unconventional features can be observed such as line nodes in the superconducting gap function or the involvement of spin-triple pairs in the superconductor condensate. In non-centrosymmetric superconductors the lack of inversion symmetry along with an antisymmetric spin-orbit coupling (ASOC) lifts the degeneracy of the conduction band electrons [27]. This in turn can produce superconducting states that are spin-singlet (even-parity), spin-triplet (odd-parity) or admixture of the two [28, 29]. In the presence of a finite ASOC, parity is no longer a good quantum number and as a result the superconducting states may no longer be classified as spin-singlet or triplet but an admixture of the two [2]. Mixed pairing allows NCS to show unusual phenomena including critical fields exceeding the Pauli limit and time-reversal symmetry breaking [30]. Materials explored until now can be distinguished in groups where strong correlations occur between electrons and those which behave like simple metals. Superconductivity has been observed in several

non-centrosymmetric compounds with cubic α-Mn and hexagonal structures [11].

Many of the recently discovered non-centrosymmetric superconductors are heavy fermions like $CePt_3Si$ which was the first non-centrosymmetric heavy fermion superconductor to be studied in detail [2]. This material is an antiferromagnetic heavy fermion that has a magnetic ordering temperature T_N of 2.2 K and a superconducting transition temperature T_c of 0.75 K. Heavy fermion materials are a subset of the intermetallic compounds containing f-electron elements [31]. Most of the heavy fermion non-centrosymmetric superconductors investigated consist of $4f$ electron elements like Ce [32]. In heavy fermion materials, the $4f$ electrons might mask the effects of broken inversion symmetry. Additionally, the only known heavy fermion non-centrosymmetric superconductors are $CePt_3Si$, $CeTGe_3$ (T = Rh, Ir), $CeXSi_3$ (X = Pt, Pd) and UIr as stated in Ref. [2]. Some difficulties were faced previously in order to separate the effects of unconventional pairing states and coexistent magnetic order or strong electronic correlations. In $CePt_3Si$, line nodes and measurements of spin susceptibility may indicate mixed singlet or triplet pairing states. The line nodes can also be a result of coupling with magnetic order [33]. Furthermore strong electronic correlations enhance the spin susceptibility to the normal state value in all directions [34]. In order to avoid these effects, the present work is based on some weakly correlated non-centrosymmetric materials.

1.2.1 Weakly correlated non-centrosymmetric superconductors

The properties of weakly correlated non-centrosymmetric superconductors will be explained in this section. Mixed pairing states result from the loss of inversion symmetry. A considerable number of NCS superconductors which have simple metallic normal state without any evidence of magnetic ordering or strong electron correlations have been investigated previously [2, 11, 26, 30].

The observations of a spin-singlet state in an s-wave superconductor have been the 'precursor' of the study of superconductivity lacking inversion symmetry. Standard examples of such compounds are Li_2Pd_3B and Li_2Pt_3B with transition temperatures 7 and 2.7 K, respectively which are also good examples for studying the effect of antisymmetric spin-orbit coupling (ASOC) on superconductivity and the related phenomena which may show novel properties. Both compounds crystallize in the cubic non-centrosymmetric perovskite type structure indicating an absence of strong electron correlations. There is an increase in ASOC by the substitution of the heavier Pt for Pd [35]. They also exhibit a quadratic temperature dependence of

the electronic specific heat and a linear temperature dependence of the penetration depth, at low temperatures which indicates the presence of line nodes. The magnetic penetration depth for these two compounds is modelled with a superconducting gap which consists of an admixture of an isotropic singlet and a triplet state [36]. This in turn agrees with the spin-orbit coupling of the crystal structure. Additionally, in the orthorhombic compound $LaNiC_2$, unconventional superconductivity was reported. The transition temperature of this compound is 2.7 K [37]. The presence of point nodes [38] and a fully two gap structure [39] was indicated by the magnetic penetration depth measurements. The nodal gap structure is very interesting in metallic NCS superconductors because it indicates the unconventional nature of the superconductivity.

One of the important consequences of the coupling is the upper critical field. In NCS superconductors the upper critical field can not be explained using the weak-coupling Werthamer-Helfand-Hohenberg (WHH) model. For example, for Li_2Pd_3B and Li_2Pt_3B the $H-T$ phase diagram for different Pt-contents remains the same although the pairing state changes with the Pt-doping concentration [40]. As a result, the upper critical field could be scaled with T_c. According to Ref. [40], the upper critical field increases linearly with decreasing temperature near T_c and at low temperatures it shows an upturn in the curvature. These features indicate the importance of broken inversion symmetry on superconductivity in which the spin-triplet state can increase the upper critical field.

Several non-centrosymmetric superconductors have been reported with similar superconducting properties as BCS s-wave superconductivity. Some of these compounds are $LaPt_3Si$ [41], Re_3W [42], $Re_{24}Ti_5$ [43] and X_2Ga_9 where X = Rh, Ir) [44, 45]. Some type-II superconductors containing $5d$ transition metals are $SrPdGe_3$, $SrPtGe_3$ [46], $BaPtSi_3$ [47], $CaPtSi_3$, $CaIrSi_3$ [48] and $LaIrSi_3$ [49] with transition temperatures 1.49, 1, 2.25, 2.3, 3.6 and 0.9 K, respectively. The normal and superconducting state properties of these compounds are given in table 1.1. The compounds $BaPtSi_3$, $CaPtSi_3$ and $CaIrSi_3$ have specific heat values consistent with an isotropic superconducting gap of the magnitude predicted by BCS theory. The presence of $5d$ states may indicate that the bands will be significantly affected by spin-orbit coupling. For $BaPtSi_3$, the relativistic calculations indicated that there is significant spin-orbit splitting of the bands at approximately -1.5 eV [47]. In the latter, electrons are condensed to form Cooper pairs and as a result spin-orbit coupling does not need to be considered in order to determine the superconducting

Compounds	**Transition Temperature (T_c)**	**Space Group**	**γ (mJ/molK^2)**	**Superconducting State**	**References**
$BaPtSi_3$	2.25	$I4mm$	5.7	One gap.	52,53
$CaIrSi_3$	3.6	$I4mm$	5.8	One gap.	54
$CaPtSi_3$	2.3	$I4mm$	4	One gap.	54
$Re_{24}Ti_5$	5.8	$I\bar{4}3m$\$	111.8	One gap.	49
Re_3W	7.8	$I\bar{4}3m$\$	15.9	One gap.	48
$CePt_3$	0.75	$I4mm$	390	Line nodes, isotropic $B_{c2} > H_p$.	3, 36, 37, 38, 47
$LaIrSi_3$	0.77	$I4mm$	4.5	Anisotropic, one gap.	55
$LaNiC_2$	2.7	$Amm2$	7.7	TRSB. Two gaps/ point nodes.	41, 42, 43, 45
$LaPt_3B$	0.64	$P4mm$	0.5	Isotropic gap.	47
Li_2Pt_3B	2.7	$P4_332$	7	Anisotropic fully gapped.	38, 39, 40
Li_2Pd_3B	7	$P4_332$	9	Anisotropic, line nodes.	38, 39, 40
Re_6Zr	6.75	$I\bar{4}3m$\$	26	TRSB, fully gapped.	46
$SrPdGe_3$	1.49	$P4mm$	5	s-wave fully gapped.	52
$SrPtGe_3$	1	$P4mm$	4	s-wave fully gapped.	52
Rh_2Ga_9	1.95	Pc	7.64	Fully isotropic gap.	50, 51
Ir_2Ga_9	2.25	Pc	7.32	Fully isotropic gap.	50, 51

Table 1.1: Superconducting and normal state properties of selected non-centrosymmetric superconductors which are reported in this section. The values given were observed at ambient pressure. Time reversal symmetry breaking is denoted with TRSB.

properties of this compound.

The weakly correlated NCS superconductors can give information about the role of broken symmetry. The superconducting pairing state may change by increasing the ASOC strength due to the broken symmetry. The range of the properties observed in the weakly correlated non-centrosymmetric superconductors is explained above. This range varies from systems where spin-orbit coupling leads to unusual nodal gap structures, to those where fully gapped, two-band behaviour is observed and those which are single band BCS superconductors [2]. A two gap structure was expected to be a general characteristic of non-centrosymmetric superconductors but for a weak spin-orbit coupling both gaps can be isotropic and have similar magnitudes. For example, $LaNiC_2$ shows unconventional behaviour but this is not because of strong ASOC. Also theoretical calculations show that the non-unitary state is permitted only when the ASOC is weak. However, the studies of weakly correlated non-centrosymmetric superconductors allowed progress to be made in the effects of electron correlations and inversion symmetry breaking.

1.2.2 Time-reversal symmetry breaking

Time-reversal symmetry breaking is an interesting property of superconductors. The spin or orbital moments of the Cooper pairs are non-zero in superconductors with broken time-reversal symmetry. Evidence of time-reversal symmetry breaking is the existence of a small spontaneous magnetic field for a superconductor in zero field. The inhomogeneous ground state of a superconductor may be increased by a finite hyperfine field. Time-reversal symmetry breaking has been observed in only a few non-centrosymmetric compounds, Re_6Zr [50], $LaNiC_2$ [37, 38, 39, 51] and La_7Ir_3 [52]. Table 1.2 shows information about these compounds such as the crystal structures, the space groups, and the transition temperatures.

Time reversal symmetry breaking is a result of a subset of spin-triplet states known as non-unitary and the Cooper pairs are spin polarised [53]. Although there are three non-unitary states which agree with the crystal structure, none of these are allowed if there is a sizeable ASOC [51]. $LaNiC_2$ is in a superconducting state below its transition temperature which is 2.7 K and crystallizes in a non-centrosymmetric $CeNiC_2$-structure. In this compound, the spin-orbit coupling is weak and the unconventional pairing state occurs despite the non-centrosymmetric crystal structure. The potential gap functions indicated by a point group analysis for this compound are 12 but only 4 of them allow the time-reversal symmetry breaking. The al-

Compounds	Transition Temperature T_c (K)	Space Group	Crystal Structure	Structure Type	References
$LaNiC_2$	2.7	$Amm2$	Orthorombic	$CeNiC_2$	37, 38, 39, 50
Re_6Zr	6.75	$I\bar{4}3m$	Cubic	α-Mn	54
La_7Ir_3	2.25	$P6_3mc$	Orthorombic	Th_7Fe_3	51

Table 1.2: Non-centrosymmetric superconductors with broken time-reversal symmetry.

lowed potential gap functions describe only a non-uniform superconductor with a weak spin-orbit coupling [51, 54]. The appearance of nodes in the superconducting gap functions identify the unconventional behaviour of the superconductivity in $LaNiC_2$ [38].

Time reversal breaking was also reported for non-centrosymmetric Re_6Zr with the α-Mn structure [50]. The crystal structure contains a large number of heavy atoms which are located in non-centrosymmetric positions and as a consequence, a negligible ASOC is unlikely. In this case if there is ASOC, the non-unitary subset of singlet states is protected, as a result of the higher symmetry of the cubic α-Mn structure and a state with the mixture of singlet and triplet states was indicated. The non-centrosymmetric Re_6Zr has a transition temperature of 6.75 K and it crystallizes in a non-centrosymmetric α-Mn cubic structure. The group representation analysis of this compound also shows unconventional behaviour [50]. In Re_6Zr evidences of strong electron-phonon coupling and of broken time-reversal symmetry were observed [50].

1.3 Niobium Rhenium Series

1.3.1 α-Mn and σ structures

In 1961, Matthias reported several superconducting compounds, with a non-centrosymmetric cubic α-Mn structure [55]. These compounds include Re_3Ta, Re_6Zr and NbRe with transitions temperatures 1.46, 7.4 and 9.7 K, respectively [11]. Transition temperatures reflect the influence of the valence electron concentration. The Niobium-Rhenium series is particularly interesting. In this system two phases occur, one with σ structure and the other with an α-Mn type [56]. The non-centrosymmetric composition investigated in the present work is Nb_xRe_{1-x} for x = 0.22, 0.29 and 0.34. The σ structure forms at around 0.57 Rhenium and exists over a small range of composition and temperatures at 2450 °C as shown in Fig. 1.3. A flat minimum produced close to 0.5 Niobium corresponding to the eutectic tem-

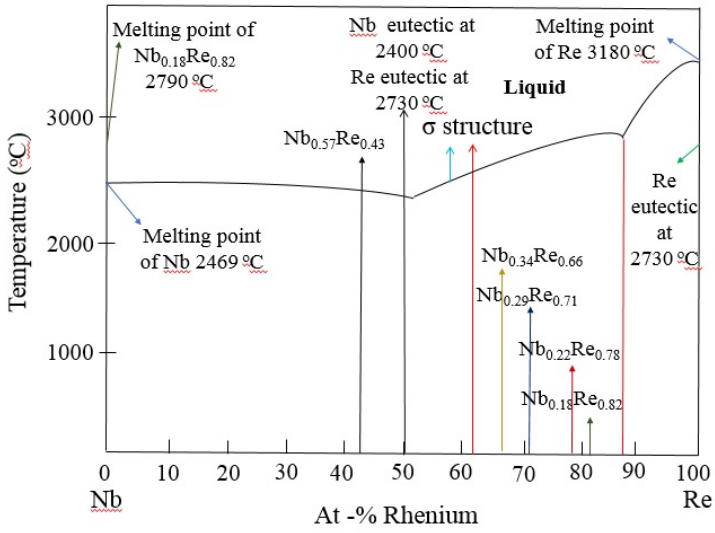

Figure 1.3: A Niobium-Rhenium system diagram indicating the melting points and eutectic temperatures.

perature between the Niobium based solid solution and the σ phase. A second small minimum occurs near 0.12 Niobium corresponding to the eutectic temperature between the Niobium and the α-Mn phase (Fig. 1.3). The α-Mn structure melts at approximately 2800 °C and has a homogeneity range of 0.13 to 0.38 Niobium as illustrated in Fig. 1.3. Above 0.48 Niobium, there is a coexistence of a solid solution with Niobium with the eutectic temperature at 1000 °C [56]. The maximum solid solubility of Rhenium in Niobium is 0.46 at the eutectic temperature falling at 0.43 at 1000 °C. Below 0.13 Niobium, there is a solid solution with Rhenium and the eutectic temperature at 2730 °C. The maximum solid solubility of Niobium in Rhenium is very low. The melting points of Niobium and Rhenium are 2468 °C and 2800 °C.

Western and Phragmen are the prime investigators of α-Mn structure [57]. According to their research and experimental data, this structure has a cubic cell whose side is 8.894 Å and each unit cell contains 56 atoms. Subsequently, these results were proved to be inaccurate as stated in [58]. Using the data collected previously, an accurate analysis was made by Bradley and Thewlis [58]. They determined that the number of atoms per unit cell is 58 as the α-Mn structure is body centred with an even number of atoms per unit cell. The atoms positions depend on a large number of parameters. The structure of α-Mn is stable for Niobium-Rhenium system at room temperature. The data shown in Ref. [58], suggested that the planes with

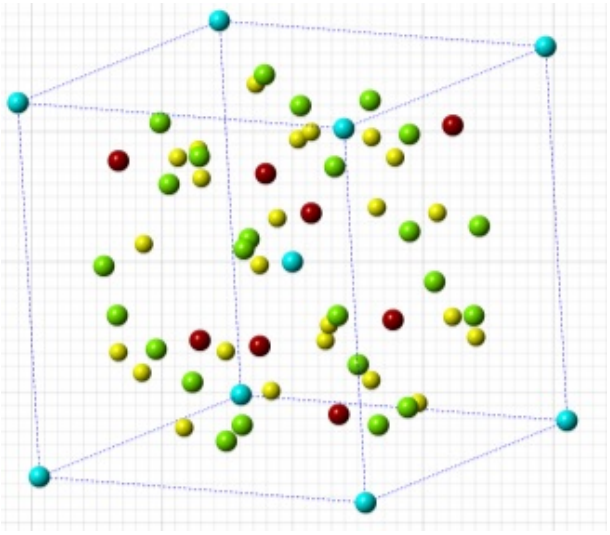

Figure 1.4: Crystal structure of Nb_xRe_{1-x} corresponding to $x = 0.17$, where the Re atoms located at $24g$ sites are represented in green and yellow. Nb atoms of sites $2a$ and $8c$ are shown in blue and red, accordingly.

$(h + k + l)$ equals to an odd number have their spacings halved compared with the planes with even number and all other spacings are normal. Therefore, there is a limited number of space groups applicable which are T^3, T_h^5, T_d^3, O^5 and O_h^9. The positions of the atoms are defined by five parameters which are denoted as a, d, e, f and g states. The interatomic distances vary between 2.75 Å to 2.95 Å, indicating an unequal distribution of electrons between the atoms.

In the α-Mn structure the 58 atoms in the unit cell have four distinct crystallographic sites of 2, 8, 24 and 24 atoms [58]. Two of these sites have positions of $2a$ and $8c$ which according to Ref. [56, 58] are occupied by niobium atoms. The remaining sites have the label $24g$ and are occupied by a distribution of niobium and rhenium atoms. Rhenium atoms are all placed in non-centrosymmetric positions [58]. The space group (No. 217) is $I\bar{4}3m$ and the structure is based on a single body centred cubic lattice but each lattice point is substituted by atoms with tetrahedral symmetry [58]. Fig. 1.4 shows the crystal structure for composition Nb_xRe_{1-x} for $x = 0.17$ [2] where both sites of $24g$ are occupied by rhenium atoms only.

1.3.2 Niobium-Rhenium compounds

Only a few papers have been published on the physical properties of the various compositions in this system. Superconductivity in non-centrosymmetric compounds

Compounds	T_c (K)	GL Theory $B_{c2}(0)$ (kG)	BCS Theory $B^p_{c2}(0)$ (kG)	WHH Model $B^{orb}_{c2}(0)$ (kG)	γ_n mJ/molK^2
$Nb_{0.18}Re_{0.82}$	8.8	230	166	161	4.8
$Nb_{0.25}Re_{0.75}$	6.5	145	126	105	4.2
$Nb_{0.29}Re_{0.71}$	5.1	118	104	86	3.5
$Nb_{0.31}Re_{0.69}$	4.4	90	91	63	3.0

Table 1.3: Magnetic and thermodynamic properties of the non-centrosymmetric polycrystalline compounds Nb_xRe_{1-x} in the range $0.13 \leq x \leq 0.38$. Data taken from Refs. [2, 28, 59].

Nb_xRe_{1-x} in the range $0.13 \leq x \leq 0.38$ according to BCS theory was reported in 2013 and T_c ranges from approximately 8.8 K for $x = 0.18$ to around 3.5 K for $x = 0.38$ [28]. Some of the reported compounds are $Nb_{0.18}Re_{0.82}$, $Nb_{0.25}Re_{0.75}$, $Nb_{0.29}Re_{0.71}$, $Nb_{0.31}Re_{0.69}$, with transitions temperatures of 8.8, 6.5, 5.1, 4.4 K, respectively [2, 28, 29, 59]. The critical temperature T_c of the constituent materials Nb and Re are 9.3 and 2.42 K [60]. Nb_xRe_{1-x} is reported to exhibit an isotropic s-wave superconducting state according to the investigations presented in these references. Table 1.3 below shows the magnetic and thermodynamic properties of the compounds reported in Ref. [28].

The upper critical field, estimated according to the Ginzburg-Landau (GL) theory, BCS theory and Werthamer-Helfand-Hohenberg (WHH) model for $x = 0.18, 0.25, 0.29, 0.31$ are given in Table 1.3. According to WHH model, B^{orb}_{c2} values are smaller than the B_{c2} values estimated by GL theory. Similar values were estimated for B^p_{c2} according to BCS theory and they are presented also in Table 1.3. Additionally, the Sommerfeld coefficient, γ_n, which can be derived from the first term in the polynomial fits of the normal-state specific heat which is known as the electron contribution, C_e, is also presented in Table 1.3 for the compounds $x = 0.18, 0.25, 0.29, 0.31$. The Sommerfeld coefficient value decreases with increasing x.

1.3.3 $Nb_{0.18}Re_{0.82}$

More in-depth research was reported on the physical properties of polycrystalline and single crystals of $Nb_{0.18}Re_{0.82}$ [59, 2]. These properties are illustrated in Table 1.4. The transition temperature of this compound is found to be 8.8 K in good agreement with magnetization and resistivity measurement with which the compound is confirmed as a type-II superconductor. The X-ray diffraction measurements showed that the compound has a non-centrosymmetric α-Mn structure

Properties	Units	Polycrystalline $Nb_{0.18}Re_{0.82}$	Single Crystal $Nb_{0.18}Re_{0.82}$
T_c	K	8.8 ± 0.1	8.8 ± 0.2
$B_{c1}(0)$	G	55.67 ± 0.68	55 ± 2
ρ_0	$\mu\Omega$/cm	189 ± 1.89	135 ± 2.30
$B_{c2}(0)$	kG	173	148
$\gamma(0)$	mJ/mol K^2	4.8 ± 0.17	5.4 ± 0.6

Table 1.4: Superconducting and other physical properties of non-centrosymmetric polycrystalline and single crystal of $Nb_{0.18}Re_{0.82}$ [2, 27, 28, 61].

type. The lower critical field, B_{c1} was extracted from the magnetization measurements to be approximately 55 G [2, 27]. The single crystal of this compound was aligned along the [100] direction. Fig. 1.5 shows the magnetization measurements and the extracted lower critical field for a single crystal of $Nb_{0.18}Re_{0.82}$.

According to Werthamer-Helfand-Hohenberg (WHH) model in the dirty limit, the upper critical field, B_{c2} of this compound is estimated from the resistivity measurements. The upper critical field estimations for the single crystal are presented in Fig. 1.6 (a).The dashed line curve follows the WHH model when the Maki parameter, α_m and the spin orbit coupling parameter, λ_{so} are zero and the solid line is the fitting when the parameters are non-zero but follows the WHH model in the dirty

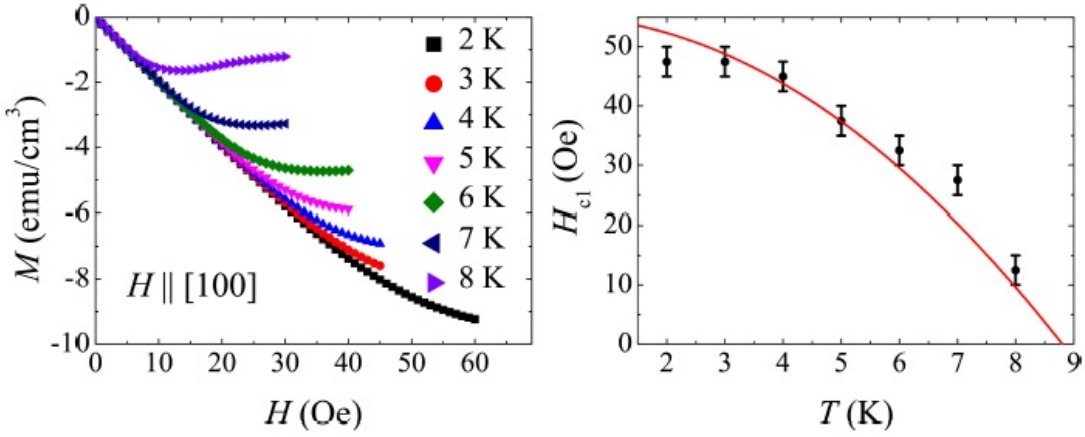

Figure 1.5: (Left) Magnetization as a function of field of a single crystal $Nb_{0.18}Re_{0.82}$. (Right) Lower critical fields, H_{c1} extracted from the data on H (Left) as a function of temperature, corrected with the demagnetization factor. The diagram was adapted from Ref. [2].

limit. By assuming, $\alpha_{\rm m} = 0$ and $\lambda_{\rm so} = 0$, $B_{\rm c2}$ was estimated to be 169 kG. According to the solid line, the $\alpha_{\rm m}$ and $\lambda_{\rm so}$ were obtained to be 1.52 ± 0.2 and 2.2 ± 0.6 and the estimated value for the upper critical field, was approximately 148 kG while the value estimated for the polycrystalline sample was approximately 173 kG.

The specific heat of the $Nb_{0.18}Re_{0.82}$ crystal in zero field and an applied field of 90 kOe is shown in Fig. 1.6 (b).The specific heat in zero field shows the onset bulk superconductivity with $T_{\rm c} = 8.8$ K. In an applied 90 kOe, $T_{\rm c}$ was smaller than the one determined at zero field applied but a bulk superconductivity was still observed. The inset shows C/T against T^2. Linear behaviour of specific heat was not observed in zero field data above $T_{\rm c}$. In an applied field of 90 kOe, linear behaviour of C/T against T could be fitted and the Sommerfeld constant, γ value was obtained [59, 2, 27]. γ value is allowed to vary with recorded values 5.49 and 4.94 mJ/molK^2.

For polycrystalline and single crystal samples of $Nb_{0.18}Re_{0.82}$, $\gamma = 4.8 \pm 0.17$ and 5.4 ± 0.6 mJ/molK^2, respectively. The jump in the specific heat at the transition is $\Delta C = 82.53$ mJ/molK and $\frac{\Delta C}{\gamma T_{\rm c}}$ is 1.75 and 1.91for $\gamma = 5.40$ and 4.94 mJ/molK^2, respectively. In 2015 point contact spectroscopy was combined with specific heat measurements to investigate the superconducting state of a single crystal of this composition [61]. The conductance spectra exhibited a two-peak structure which was in good agreement with a two-band model with isotropic gaps. The analysis of the specific heat derivative at low temperatures and close to the transition temperature in the normal state, confirmed the observations made from the point contact spectroscopy. As a result, the analyses provided strong evidence of double-gap superconductivity in non-centrosymmetric $Nb_{0.18}Re_{0.82}$ single crystals.

Following the work done on $Nb_{0.18}Re_{0.82}$, several compounds of Niobium-Rhenium system will be investigated in this project.This will include investigations of polycrystalline samples of $Nb_{0.22}Re_{0.78}$, $Nb_{0.29}Re_{0.71}$ and $Nb_{0.34}Re_{0.66}$ [1].

[1]The polycrystalline annealed sample of $Nb_{0.22}Re_{0.78}$ and non-annealed samples of $Nb_{0.29}Re_{0.71}$ and $Nb_{0.34}Re_{0.66}$ were synthesised by M. Smidman [61].

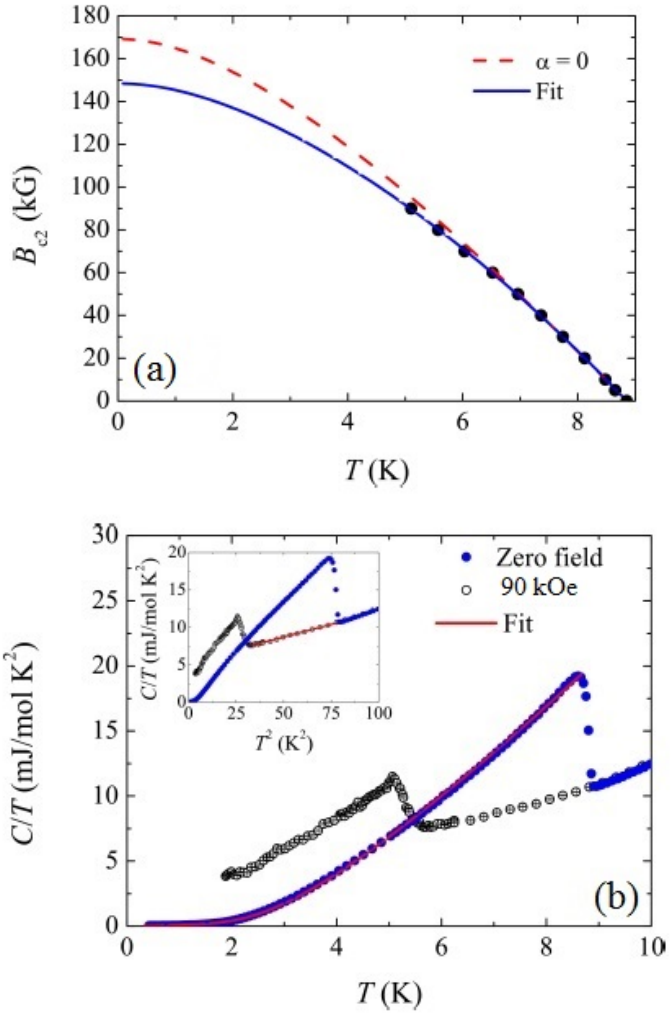

Figure 1.6: (a) Temperature dependence of the upper critical field of a single crystal of $Nb_{0.18}Re_{0.82}$ for fields applied along [100]. The values were extracted from the onset of the resistivity measurements. The dashed line indicates an estimation of B_{c2} using the WHH model with $\alpha_m = 0$ and $\lambda_{so} = 0$, while the solid line shows a fit with non-zero α_m and λ_{so}. (b) Specific heat as a function of temperature for a single crystal of $Nb_{0.18}Re_{0.82}$ in zero field and an applied field of 90 kOe. The red curve shows the fit to BCS theory for a single gap. The inset shows C/T against T^2 with a linear fit to the 90 kOe data in the normal state. The diagrams were adapted from Ref. [2].

1.4 Summary and Thesis Outline

This section introduced the concept of unconventional superconductors with particular attention given to the class of non-centrosymmetric superconductors. The superconducting properties of the non-centrosymmetric superconductors are discussed taking into account weakly correlated non-centrosymmetric superconductors and superconductors with broken time reversal symmetry as they are directly relevant to this project. The superconductors in Niobium-Rhenium series are presented in detail with attention given to the α-Mn and σ structures which are the reported structures in this system. Additionally, the previous work done, including magnetic, transport and thermal properties of several non-centrosymmetric compositions in Nb_xRe_{1-x} for $0.13 \leq x \leq 0.34$ were presented, with a more in-depth presentation of the previously research on the composition $Nb_{0.18}Re_{0.82}$ which was observed to have the highest value of transition temperature (T_c = 8.8 K) compared with the other superconductors investigated in the range $0.13 \leq x \leq 0.34$.

To be precise, the magnetic susceptibility, resistivity and specific heat capacity measurements were previously investigated for the polycrystalline compositions of $Nb_{0.18}Re_{0.82}$, $Nb_{0.25}Re_{0.75}$, $Nb_{0.29}Re_{0.71}$, $Nb_{0.31}Re_{0.69}$ and the single crystal composition of $Nb_{0.18}Re_{0.82}$. In the following work, the thermal and superconducting properties of polycrystalline non-centrosymmetric compositions of Nb_xRe_{1-x} for x = 0.22 (annealed and as-cast), 0.29 and 0,34 will be discussed. The magnetic, thermal and transport properties of the polycrystalline compositions $Nb_{0.22}Re_{0.78}$ and $Nb_{0.34}Re_{0.66}$ will be introduced for the very first time. However, a satisfying comparison between the previously reported superconducting properties and those presented in this work for the polycrystalline composition $Nb_{0.29}Re_{0.71}$ will be discussed in the following sections. Additionally, the fact that the non-centrosymmetric composition Nb_xRe_{1-x} ($0.13 \leq x \leq 0.34$) is considered as an s-wave BCS-type superconductor with negligible contributions from the spin-triplet component, despite of the heavy atomic mass of Re will be also investigated along with the previously published observation of s-wave superconductivity with a very large upper critical field ($B_{c2}(0)$) in the composition Nb_xRe_{1-x} ($0.13 \leq x \leq 0.34$).

The outline and the layout of the thesis are presented below. Chapter 2 contains the background theory required for this project including a discussion of superconductivity with a focus on non-centrosymmetric unconventional phenomena. Chapter 3 describes the various scientific experimental techniques used to collect the data presented in this research. Chapter 4 presents the superconducting properties of

several non-centrosymmetric compositions of Nb_xRe_{1-x} for $x = 0.22$, 0.29 and 0.34. Finally, Chapter 5 will provide a summary of the concepts covered and the conclusions extracted from the results obtained. In this section, the future investigations which need to be carried out in order to improve the results of this work will also be discussed.

Chapter 2

Theoretical Background

Heike Kamerlingh-Onnes, in 1908 liquified helium which gave the ability to cool materials down to temperatures very close to absolute zero [3] and the discovery of superconductivity followed. Walther Meissner and Robert Ochsenfield, observed in 1933, a phenomenon known as the Meissner effect which occurs when an applied field is expelled from a superconductor on cooling through the transition temperature for a material [62]. A few years later, in 1950, Ginzburg and Landau introduced an approach to superconductivity based on Landau's theory of a second order phase transitions [63]. Finally, in 1957, Bardeen, Cooper and Schrieffer introduced the BCS theory which gives a good explanation of conventional superconductors and provide a complete microscopic description of superconductivity [5, 8].

In this chapter, an overview of the superconductivity of non-centrosymmetric superconductors will be given and the phase transitions in superconductors will be discussed. A discussion on Ginzburg-Landau and BCS theories will be presented. The aim is to provide a good understanding of the superconducting and thermodynamics properties of superconductors, concentrating more on the effects that a non-centrosymmetric structure has on their behaviour.

2.1 Introduction to superconductivity

Early studies of superconductivity were motivated by the key experimental signatures such as perfect diamagnetism [2] and the loss of resistivity [3]. In the case of perfect diamagnetism, an applied field is unable to penetrate beyond the surface of superconducting material but during cooling through the transition temperature, T_c, magnetic flux is expelled from the bulk of the sample. In the absence of a thermodynamic or microscopic theory of the superconducting state, the electrodynamic

properties were modelled by London equations 2.1 and 2.2,

$$\mathbf{E} = \frac{m}{n_{\mathrm{s}} e^2} \frac{d\mathbf{J}_{\mathrm{s}}}{dt}, \tag{2.1}$$

$$\nabla \times \mathbf{J}_{\mathrm{s}} = -\frac{n_{\mathrm{s}} e^2}{m} \mathbf{B}, \tag{2.2}$$

where $\mathbf{E}$ is the electric field, $\mathbf{B}$ is the magnetic flux density, $\mathbf{J}_{\mathrm{s}}$ is the supercurrent density, n_{s} is proportional to the superfluid density, m is the electron mass and e is the charge of an electron and proton [64]. Eq. 2.1 describes a perfect conductor, since in the absence of an electric field, a finite current solution is allowed. Electric fields are required to change the current. The usefulness of the second equation is found from substituting in Amperes law for J_{s} which results in

$$\nabla^2 \mathbf{B} = \frac{\mathbf{B}}{\lambda_{\mathrm{L}}^2}, \tag{2.3}$$

where λ_{L} is London penetration depth and is given by

$$\lambda_{\mathrm{L}}^2 = \frac{m_{\mathrm{e}} c^2}{4\pi n_{\mathrm{s}} e^2}. \tag{2.4}$$

If the magnetic field applied to an infinite superconducting solid is constant, then the solution is a decaying exponential of the internal magnetic field with a decay constant λ_{L} [2]. Except from a region at a depth of order λ_{L} from the surface, magnetic fields were excluded completely.

2.2 Phase transitions

The nature of superconducting phase transition can give important information about the material. The Ginzburg-Landau theory follows from the Landau theory of phase transitions which describes the change from an ordered to a disordered system. For a system that orders, the order parameter, M is zero in the disordered phase and non-zero in the ordered phase. Each state of a system corresponds to a minimum in the free energy, F [65]. At the transition temperature, T_{c}, the minimum in the free energy moves from a disordered state with $M = 0$ to an ordered state with $M \neq 0$. The order parameter changes continually at T_{c} in a second-order phase transition, and as a result, F can be expanded in even powers of M as shown in

$$F = a(T - T_c)M^2 + bM^4 + ..., \tag{2.5}$$

where it is assumed that M is homogeneous and $a, b > 0$ [65]. The free energy for $T > T_c$ is minimized only for $M = 0$. On the other hand, for $T < T_c$ there is a non-zero solution given by the following equation,

$$M^2 = \frac{a(T_c - T)}{2b}. \tag{2.6}$$

According to this equation, on cooling below the transition, M increases from zero and $M \propto (T_c - T)^{\frac{1}{2}}$. The magnetization in the mean field model of an anti-ferromagnet close to the second order phase transition should dhow this behaviour. When fluctuations cannot be neglected, there is a different temperature dependence but it follows $M \propto (T_c - T)^{\beta}$, where β is a critical exponent available for a wide range of phase transitions with the same dimensionality of the system and order parameter [65]. There is a continuity in the first derivative of Eq. 2.5 with respect to magnetization at the phase transition and a discontinuity in the second derivative, which results in a discontinuity at a second order transition in quantities dependent on the second derivative of free energy like specific heat. The first order transition can be described by Eq. 2.7, where $b < 0$ and $c > 0$, if the order parameter is enough small close to the transition.

$$F = a(T - T_c)M^2 + bM^4 + cM^6 + ..., \tag{2.7}$$

At high temperatures, the free energy has a minimum only at $M = 0$. At lower temperatures the minima do not develop continuously from zero and at the phase transition the order parameter jumps from zero to a finite value. For the above model if $B^2 > 3\alpha(T - T_c)$, there are local

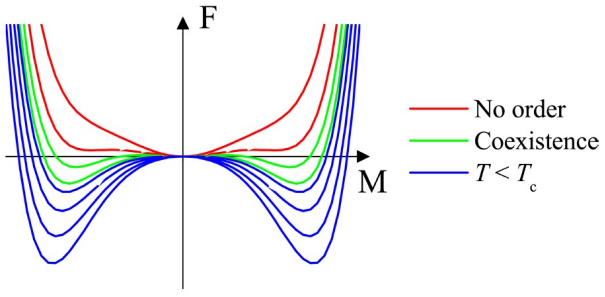

Figure 2.1: The free energy of the first order phase transition described by eq. 2.7.The minima exist first at finite M.The green lines show curves with metastable states.There is coexistence between ordered and disordered phases.The red lines show curves with the only minimum at $M = 0$. The blue lines show minima only at $M \neq 0$. Taken from [2].

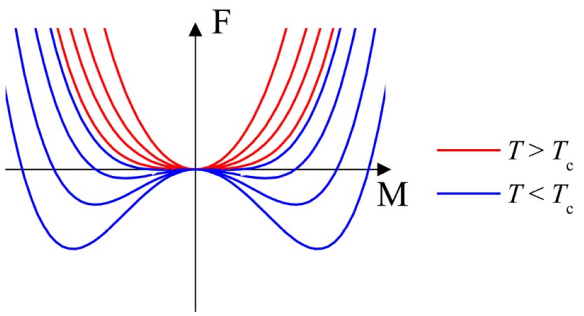

Figure 2.2: The free energy of the second order phase transition described by eq. 2.5. The minima exist continuously from $M = 0$. The red lines show curves with the only minimum at $M = 0$. The blue lines show minima only at $M \neq 0$. Taken from [2].

minima for $M = 0$ and $M \neq 0$. As a consequence, there are metastable states which is the origin of superheating and supercooling phenomena, where the system does not exist in a global minimum of the free energy but in a metastable local minimum. Figs. 2.2 and 2.1 show the free energies for the first and second order transitions, respectively. From Fig. 2.1, it can be observed that the minima emerge initially at finite M and a jump exists from $M = 0$ to finite M. From Fig. 2.2, it is clear that below T_c, the minima begins at $M = 0$ and increase continuously. In the regions of coexistence shown in green, there are local minima at both zero and non-zero order parameter.

2.3 Ginzburg-Landau theory

Ginzburg-Landau suggested a phenomenological approach to understand superconductivity, which was based on Landau's theory of second order phase transitions. This theory introduced an expansion of the free energy, which describes isotropic superconductors and superconductors with a spatially varying superfluid density. Using this theory the penetration depth (λ), the coherence length (ξ) and the critical fields can be derived with suitable boundary conditions and they are considered as 'natural' parameter of the theory. In Ginzburg-Landau theory, a complex order parameter ψ is assumed by applying a similar principle to the superconducting transition. The free energy has a similar form to Eq. 2.5 but with extra terms considering the gradient of ψ and the coupling to the magnetic field. According to Refs. [2, 66], the Gibbs free energy density of the superconducting state f_s is represented by

$$f_{\mathrm{s}} = f_{\mathrm{n}} + \alpha|\psi|^2 + \frac{\beta}{2}|\psi|^4 + \frac{1}{2m}\left|\left(\frac{\hbar}{i}\nabla - \frac{2e}{c}\mathbf{A}\right)\psi\right|^2 + \frac{\left(\mathbf{B}-\mathbf{B}_{\mathrm{app}}\right)^2}{2\mu_0}, \tag{2.8}$$

where f_{n} is the normal state free energy density, $\mathbf{B}$ is the total magnetic field, $\mathbf{B}_{\mathrm{app}}$ is the contribution from the external magnetic field, $\mathbf{A}$ is the magnetic vector potential and α, β are independent variables of temperatures [66].The gradient term is negligible for a homogeneous solution and the minimum solution similar to Eq. 2.6 can be determined. The substitution of the minimum solution to the Eq. 2.8 shows that there is a critical field $B_{\mathrm{app}} = B_{\mathrm{c}}$ at which the free energy of the Meissner state is larger than f_{n}. This results in a phase transition from the superconducting to the normal state at B_{c}, which is the thermodynamic critical field. Eq. 2.9 gives the temperature dependence of this critical field [23, 67].

$$B_{\mathrm{c1}}(T) = B_{\mathrm{c1}}(0)\left[1 - \left(\frac{T}{T_{\mathrm{c}}}\right)^2\right]. \tag{2.9}$$

The Ginzburg-Landau theory introduced two length scales, the London penetration depth, λ_{L} and the Ginzburg-Landau coherence length, ξ. If $|\psi|^2$is considered as corresponding to the superfluid density, then an effective penetration depth, λ_{eff} is connected to λ_{L} which introduces the theory via Eq. 2.4 [2]. In the superconducting state, n_{s} is non-zero and a relationship between n_{s} and the order parameter is expected. However, since ψ is a complex number, the order parameter is not the density of superconducting electrons but it is describing currents in the superconducting state. The Ginzburg-Landau coherence length is the characteristic distance over which ψ varies. Both length scales are proportional to $|\psi|^{-2}$ and therefore they diverge approaching the transition temperature, T_{c}. The Ginzburg-Landau parameter, κ is given by Eq. 2.10 and it is almost temperature independent in this theory.

$$\kappa = \frac{\lambda_{\mathrm{eff}}}{\xi}, \tag{2.10}$$

The form of F in Eq. 2.8 does not necessary include the existence of a superconducting state with internal magnetic fields. As mentioned previously, at $B_{\mathrm{app}} = B_{\mathrm{c}}$, the energetic cost of producing the Meissner state is great. In the case of a non-zero $\mathbf{B}$, the superconducting state can remain energetically favourable even for large applied fields and this depends on the value of κ. The boundary energy between the superconducting and normal states is positive if $\kappa > \frac{1}{\sqrt{2}}$ and this exists in type-II

superconductors. If $\kappa < \frac{1}{\sqrt{2}}$, then the material is a type-I superconductor while when $\kappa \approx \frac{1}{\sqrt{2}}$, then there is an attractive interaction between magnetic fields and the material is considered as a type 1.5 superconductor [68]. For type-I superconductors, the reduction in energy from the increased penetration of flux does not reduce the order parameter to zero. The samples exhibit a first order transition from the Meissner state to the normal state when the applied field is large enough. Demagnetization factors can be finite according to Ref. [69] and for this case, there is an intermediate state with macroscopic domains between the superconducting and normal phases.

For type-II superconductors, there is no limitation to the boundary area between the normal and the superconducting state, when the boundary energy is negative. Because of the complex nature of ψ, the flux passing through a normal region must be a multiple of the magnetic flux quantum, $\Phi_0 = 2.067834 \times 10^{-15}$ Wb. There is a Meissner state for applied fields less than the lower critical field given by

$$\mu_0 B_{\mathrm{c1}}\big(T\big) = \frac{\Phi_0}{4\pi\lambda_{\mathrm{eff}}^2}\big(\ln\kappa + \alpha\big(\kappa\big)\big), \tag{2.11}$$

which is valid for type-II superconductors, where $\alpha\big(\kappa\big)$ is an independent variable of κ and can be calculated by Ref. [63, 67]. If the magnetic field is greater than this value, flux can penetrate through the sample via thin tubes and the mixed state occurs.There is a repulsive force between flux lines which are placed in the minimum energy configuration [70]. In 1957 Abrikosov found an approximation of the Ginzburg-Landau equations corresponding to homogeneous type-II superconductors in magnetic fields below the upper critical field, B_{c2} [71]. When the orbital upper critical field, $B_{\mathrm{c2}}^{\mathrm{orb}}$ is reached, the flux lines overlap, which means that all the material is in the normal state (100%). The orbital upper critical field $B_{\mathrm{c2}}^{\mathrm{orb}}$ is given by Eq. 2.12 and its relationship with the critical field in type-I superconductor, B_{c} is shown in Eq. 2.13, which illustrates how the mixed state remains energetic for type-II superconductors for applied fields higher than B_{c} considerably. According to Ref. [72, 73], Eq. 2.14 is estimating the Ginzburg-Landau parameter, κ using the lower (B_{c1}) and upper critical field (B_{c2}).

$$B_{\mathrm{c2}}^{\mathrm{orb}} = \frac{\Phi_0}{2\pi\xi^2}, \tag{2.12}$$

$$B_{\mathrm{c2}}^{\mathrm{orb}} = \sqrt{2}\kappa B_{\mathrm{c}}, \tag{2.13}$$

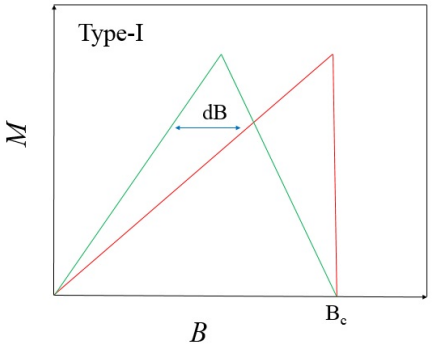

Figure 2.3: Magnetization as a function of internal field for an ideal type-I superconductor.The red curve shows the behaviour when demagnetization factor, D is zero and green curve shows non-zero D, where the curve has been shifted by an amount of dB indicated by the blue arrow.

$$\frac{B_{c2}^{\mathrm{orb}}}{B_{c1}} = \frac{2\kappa^2}{\ln \kappa}, \tag{2.14}$$

The magnetic properties of type-I and type-II superconductors are particularly interesting, including the magnetization and the internal magnetic field distribution. For a type-I superconductor, according to Fig. 2.3, in the absence of demagnetization effects, there is a discontinuity in the magnetization at B_c. However, this is only the case when a field is applied parallel to the surface of an infinitely thin superconducting sheet. In reality, a sample has a finite demagnetization factor, D. For a uniform magnetization, M when Eq. 2.15

$$\mathbf{B}_c = \mathbf{H} - D\mathbf{M}. \tag{2.15}$$

is valid, flux penetrates the sample and it enters the intermediate state. For the Meissner state, $\mathbf{M} = \mathbf{H}$ which occurs when $\big(1 - D\big)H = B_c$, where H is the applied field.The magnetization as a function of the applied fields for an ideal type-II superconductor is illustrated in Fig. 2.4. Up to B_{c1}, the magnetization is linear. Above B_{c1} flux penetrates the sample until the magnetization reaches zero at B_{c2}.

The existence of type-I and type-II superconductivity depends only on the value of the dimensionless parameter κ. Ginzburg-Landau theory can be used to quantitatively describe inhomogeneous systems which in this case is the mixed state of a type-II superconductor. However, Landau theory is valid when the order parameter is small and as a result it may not be applicable away from the phase boundary.

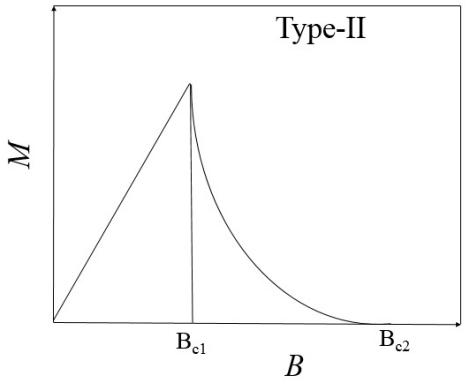

Figure 2.4: Magnetization as a function of internal field for an ideal type-II superconductor.

2.4 BCS Theory

In this section the microscopic BCS theory will be explained. In 1957, the microscopic theory of superconductivity was developed by Bardeen, Cooper and Schrieffer (BCS). This theory describes well conventional superconductors. After its proposal, it was clear that the Ginzburg-Landau equations could be derived from BCS theory in a temperature region close to $T_{\rm c}$ [74] which shows a relation between the phenomenological parameters in the Ginzburg-Landau free energy and the microscopic BCS parameters. One result is the identification that $|\psi|^2$ is proportional to the superfluid density $n_{\rm s}$ [65, 75]. The microscopic BCS theory of superconductivity needs a system at which the ground state of a metal is not the normal state and as a result, it will be possible to look for means at which electrons in a free band can exhibit a phase transition to an ordered system. According to Ref. [76], when an attractive interaction exists between two electrons just above the Fermi level, there can be a bound state between them. In conventional superconductors there is an attractive interaction between the electrons rising from interactions with the lattice (electron-phonon interaction). In the simplest BCS models, there is a constant attractive interaction within $\hbar\omega_{\rm D}$ of the Fermi surface, where $\omega_{\rm D}$ is the Debye frequency which is the maximum phonon frequency. The BCS wave function is given in Eq. 2.16 [5, 8, 62],

$$| \text{BCS} >= \prod_{\rm k} \left(u_{\rm k} + e^{i\theta} v_{\rm k} c^{\dagger}_{\rm k+s,\uparrow} c^{\dagger}_{\rm -k+s,\downarrow}\right) | 0 > . \tag{2.16}$$

where θ is the angle between $u_{\mathbf{k}}$ and $v_{\mathbf{k}}$, c is the electron creation operator of momentum k and spin s which is either up ($\uparrow$) or down ($\downarrow$).

The normalization of the wave function postulates that $u_{\mathbf{k}}^2 + ^2 = 1$, where $u_{\mathbf{k}}^2$ and $v_{\mathbf{k}}^2$ are the Bogoliubov coherence factors. The pairs of electrons with opposite crystal momenta $\mathbf{k}$ and $-\mathbf{k}$, a centre of mass momentum $2\hbar s$ and opposite spins known as Cooper pairs in the s-wave state, are described by the second term of the equation, $v_{\mathbf{k}}^2$. That is valid for an isotropic interaction where the lowest energy wave function is spherically symmetric. The Cooper pairs require opposite spins in order to show that the overall pair wave function is antisymmetric under particle exchange. The quasi-particle excitation energy $\big(E_{\mathrm{k}}\big)$ is illustrated in

$$E_{\mathrm{k}} = \sqrt{\epsilon_{\mathrm{k}}^2 + \Delta_{\mathrm{k}}^2}, \tag{2.17}$$

where ϵ_{k} is the band energy measured from the chemical potential. The excitation spectrum is gapped with a k dependent energy gap Δ_{k} which is determined by solving the gap equation shown in

$$\Delta_{\mathrm{k}} = -\sum_{\mathrm{k}'} \big(1 - 2f_{\mathrm{k}'}\big) \frac{\Delta_{\mathrm{k}'}}{2E_{\mathrm{k}'}} V_{\mathrm{kk}'}, \tag{2.18}$$

where f is the Fermi-Dirac function, $V_{\mathrm{kk}'}$ is the matrix element for the interaction between electrons in the $\mathbf{k}$ and $\mathbf{k}'$ states. The Fermi-Dirac function is shown in

$$f = \left(1 + e^{\frac{E}{k_{\mathrm{B}}T}}\right)^{-1}. \tag{2.19}$$

Considering the isotropic weakly coupled BCS theory, an attractive potential $-V$ within $\hbar\omega_{\mathrm{D}}$ of the Fermi surface is observed. The energy gap is independent of $\mathbf{k}$ within this region and at $T = 0$ the magnitude of the gap $\big(\Delta_0\big)$ is given by

$$\Delta_0 = 1.764 k_{\mathrm{B}} T_{\mathrm{c}}. \tag{2.20}$$

An approximate formula of $\Delta\big(T\big)$ for non-zero T given in Ref. [77] is presented in Eq. 2.21 and shown schematically in Fig. 2.5.

$$\Delta\big(T\big) = 1.764 k_{\mathrm{B}} T_{\mathrm{c}} \tanh\left(1.82\left[1.018\left(\frac{T}{T_{\mathrm{c}}} - 1\right)\right]^{0.51}\right), \tag{2.21}$$

It is desirable to calculate the gap function for superconductors with anisotropic gaps or for stronger coupling, which requires a self consistent solution to Eq. 2.18 for an approximate value of $V_{\mathrm{kk}'}$. Experimental data are analysed usually using the α-model of superconductivity [2, 5]. The temperature dependence of the gap is the same as in weakly coupled isotropic BCS theory, but in this situation the

factor of 1.764 is replaced by a variable α as shown in Eq. 2.22, where $\alpha_{\mathrm{BCS}} = 1.764$ corresponds to BCS theory.

$$\Delta_0 = \alpha k_{\mathrm{B}} T_{\mathrm{c}}. \tag{2.22}$$

As shown in Ref. [78], $\alpha > \alpha_{\mathrm{BCS}}$ corresponds to strong electron-phonon coupling and $\alpha < \alpha_{\mathrm{BCS}}$ indicates an anisotropic superconducting gap. The electron-phonon coupling parameter, λ_{ep} gives the strength of the attractive interaction for BCS superconductors [12, 13]. The weak coupling limit is determined by $\lambda_{\mathrm{ep}} << 1$.However, superconductors with $\lambda_{\mathrm{ep}} < 0.5$ are weakly coupled. The transition temperature can be obtained using Eq. 2.23 for strong coupling theory,

$$T_{\mathrm{c}} = \frac{\Theta_{\mathrm{D}}}{1.45} exp\left[- \frac{1.04\big(1 + \lambda_{\mathrm{ep}}\big)}{\lambda_{\mathrm{ep}} - \mu^{*}\big(1 + 0.62\lambda_{\mathrm{ep}}\big)} \right], \tag{2.23}$$

where μ^* is a constant produced due to Coulomb repulsion normally varying between 0.1 and 0.15 and Θ_{D} is the Debye temperature which is given by:

$$\Theta_{\mathrm{D}} = \left(\frac{12\pi^4 R n}{5\beta} \right)^{\frac{1}{3}}, \tag{2.24}$$

where β is the Debye T^3-law latice heat capacity coefficient, R is the molar constant and n is the number of atoms per formula unit (f.u). Important limits on the transition temperatures of conventional BCS superconductors are deduced from Eq. 2.23 [79].

For an isotropic attractive potential, an isotropic s-wave state with even parity $\big(meanfreepath(l) = 0\big)$ is formed by the Cooper pairs. The spin component of the pairing wave function must be antisymmetric under particle exchange as discussed previously and as a result this is a spin singlet state. Other pairing mechanisms might be able to pair states with higher values of l. For example, in p-wave superconductors, odd parity states $\big(l = 1\big)$ are formed by the Cooper pairs and therefore this is a spin triplet configuration, where pairs consists of two electrons in an $S = 1$ state [2]. In this situation, the pairing state is indicated by a vector $\mathbf{d}(\mathbf{k})$ and the gap is determined by $|\mathbf{d}(\mathbf{k})|^2$ [1, 80] which will be explained in the following section.

For triplet superconductors, the superconducting gap can be anisotropic becoming zero at certain points of the Fermi surface. Furthermore, it can be non-unitary triplet state which breaks time reversal symmetry in the superconducting state, where the

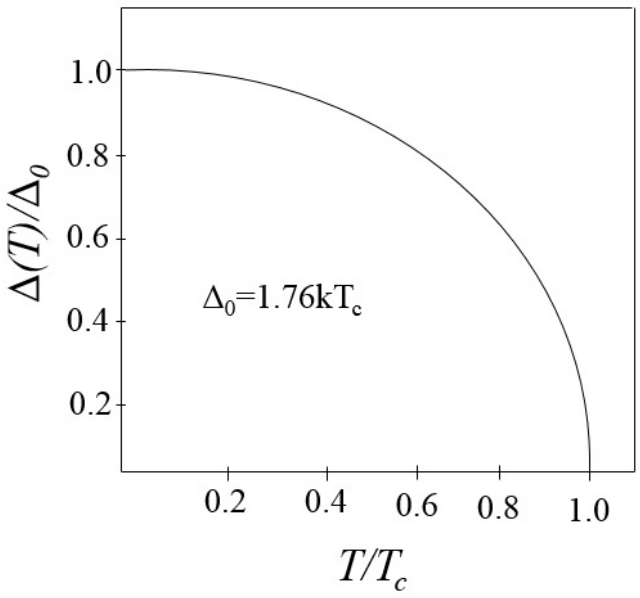

Figure 2.5: The approximation of the normalized temperature dependence of the BCS gap as a function of the reduced temperature $t = T/T_c$, according to Eq. 2.21.

Cooper pairs are spin polarised. On the other hand, there can be spin triplet states with higher order pairing angular momenta. Spin singlet state is formed by the fact that d-wave superconductors have even parity pairing $l = 2$. This is the pairing state for the cuprate superconductors which have nodes in the superconducting gap [81].

2.5 The gap structure of non-centrosymmetric superconductors

The paring states can be classified as either spin singlet or spin triplet. This is valid where the orbital part of the pair wave functions have either even or odd parity. The Cooper pairs may be singlet or triplet, as the wave function must be antisymmetric. In the presence of a finite antisymmetric spin-orbit coupling (ASOC) for non-centrosymmetric superconductors, the pairing states are classified as an admixture of singlet and triplet [82]. Eq. 2.25 shows the superconducting parameter $\mathbf{\Delta}(\mathbf{k})$ for this case, where ψ is the singlet component and $\mathbf{d}(\mathbf{k}) \cdot \sigma$ is the triplet component.

$$\mathbf{\Delta}(\mathbf{k}) = i(\psi + \mathbf{d}(\mathbf{k}) \cdot \sigma)\sigma_y. \tag{2.25}$$

The antisymmetric spin-orbit coupling (ASOC) is splitting the spin degenerate con-

duction band and the resulting superconducting gaps are given by

$$\mathbf{\Delta}_{\pm}(\mathbf{k}) = \psi \pm \mid \mathbf{d}(\mathbf{k}) \mid. \tag{2.26}$$

As a result the two gaps are given by the constructive and destructive interference of the singlet and triplet terms.

2.6 Thermodynamic properties of superconductors

Following the discussion made for the Ginzburg-Landau theory and BCS theory, the thermodynamic properties of superconductors can be examined. Many thermodynamic properties are influenced by the gap Δ_{k} which affect the density states around the Fermi level. For a metal, Eq. 2.27 determines the temperature dependence of the electronic contribution to the specific heat of a normal state, where $\frac{\pi^2}{3}N\big(E_{\mathrm{F}}\big)k_{\mathrm{B}}^2$ is usually written as a constant γ.

$$C_{\mathrm{el}} = \frac{\pi^2}{3}N\big(E_{\mathrm{F}}\big)k_{\mathrm{B}}^2 T, \tag{2.27}$$

The total specific heat at low temperatures includes the electronic and the phonon contributions is given by

$$C = \gamma T + \beta T^3, \tag{2.28}$$

where γ is the Sommerfeld electronic heat capacity coefficient and β is the Debye T^3-law lattice heat capacity coefficient which is related to Θ_{D} by Eq. 2.24 (see Section 2.5).

In order to determine the expression below T_{c}, the entropy of the superconducting state needs to be considered [83] and the expression is shown in

$$\frac{S}{\gamma T_{\mathrm{c}}} = -\frac{6\Delta_0}{\pi^2 k_{\mathrm{B}} T_{\mathrm{c}}}\int_0^{\infty}[f\ln f + \big(1-f\big)\ln\big(1-f\big)]dy, \tag{2.29}$$

where f is the Fermi-Dirac function with $E = \Delta_0\sqrt{y^2+\delta T^2}$. In this equation, y is the energy of the normal state electrons and $\delta(T)$ is the temperature dependence of the superconducting gap. The left hand side of Eq. 2.29 is normalised to the normal state entropy at T_{c}.

As explained in Section 2.2, the first derivative of the free energy is continuous for a second order phase transition, which means that the left hand side of this equation

is unity at the transition in zero-field. As a consequence, the electronic contribution to the specific heat is presented by Eq. 2.30 and it is discontinuous at the transition.

$$\frac{C_{\rm sc}}{\gamma T} = \frac{d\big(S/\gamma T_{\rm c}\big)}{dt}. \tag{2.30}$$

$\frac{\Delta C}{\gamma T_{\rm c}} = 1.426$ gives the magnitude of the jump in BCS theory. Generally, in the α-model, this magnitude is proportional to α^2 and the equation is modified to Eq. 2.31 [84].

$$\frac{\Delta C}{\gamma T_{\rm c}} = 1.426\left(\frac{\alpha}{\alpha_{\rm BCS}}\right)^2, \tag{2.31}$$

At low temperatures, there are no states within $\sim k_{\rm B}T$ of the Fermi level for a fully gapped superconductor and as a result there are no states for electrons to be excited. Therefore, the specific heat at low temperatures has a dependence with $C \propto \big(\Delta_0/k_{\rm B}T\big)^{\frac{3}{2}} e^{-\left(\Delta_0/k_{\rm B}T\right)}$ [8].

2.7 The clean and dirty limits

A microscopic theory which can reproduce the Ginzburg-Landau theory close to $T_{\rm c}$ was obtained and as a result it is of interest to relate the characteristic length scales of this theory to microscopic properties. ξ is a characteristic length with which the order parameter ψ varies. It should be related to a characteristic length of the extent of the Cooper pair wave function which is the BCS coherence length, ξ_0 given by

$$\xi_0 = \frac{\hbar \upsilon_{\rm F}}{\pi \Delta_0}, \tag{2.32}$$

where $\upsilon_{\rm F}$ is the Fermi velocity. This quantity is related to the coherence length in Ginzburg-Landau theory by $\xi \sim 0.74\xi_0$ if the elastic scattering of electrons from the lattice is negligible [1, 5, 8]. This is valid if the scattering rate is low and as a consequence the electrons have a long mean free path, l between the scattering events. If $\xi_0 << l$, the system is in this clean limit. If the scattering rate is high, ξ will change. In this case, the system is in the dirty limit where $l << \xi_0$, $\xi \propto \sqrt{\xi_0 l}$. In the clean limit, $\lambda_{\rm eff}$ is given by

$$\lambda_{\rm eff} = \frac{\lambda_{\rm L}}{\sqrt{2}}. \tag{2.33}$$

In the dirty limit,$\lambda_{\rm eff}$ is given by

$$\lambda_{\text{eff}} = \lambda_{\text{L}} \sqrt{\frac{\xi_0}{1.33l}}. \tag{2.34}$$

λ_{eff} increases due to the effect of strong scattering and as a result the effectiveness of the screening of the magnetic fields reduce from the expected. Considering the number of superconducting electrons, κ is given by

$$\kappa = 0.96 \frac{\lambda_{\text{L}}}{\xi_0}, \tag{2.35}$$

in the clean limit and by Eq. 2.36 in the dirty limit.

$$\kappa = 0.715 \frac{\lambda_{\text{L}}}{l}, \tag{2.36}$$

In the dirty limit, κ is independent of ξ_0 and it is inversely proportional to the mean free path.

2.8 Upper Critical Field

An applied field can destroy superconductivity in a type-II superconductor using one of two pair-breaking mechanisms. One is the orbital pair breaking, which exists when there is overlap of vortex cores and the orbital upper critical field is given by Eq. 2.12. The paramagnetic limiting effect also occurs and it can be understood by taking into account the effect of an applied field on a band of electrons [30]. The degenerate bands are split into spin-up and spin-down bands. This decreases the energy of the system by the Zeeman energy given by $\chi_{\text{n}} H^2/2$, where χ_{n} is the normal state susceptibility known as the Pauli susceptibility for an electron gas. Cooper pairs with spin-singlet behaviour have opposite spins, which means that $\chi_{\text{s}} = 0$ if at $T = 0$, the electrons on the Fermi surface are paired. As a result, there is an applied field at which there is a reduction in energy larger than the Zeeman energy. At this point the system will become normal. This field is known as the Pauli paramagnetic limit,H_{p} which is given by

$$\mu_0 H_{\text{p}} = \frac{\sqrt{2}\Delta_0}{g\mu_{\text{B}} \sqrt{\left(1 - \frac{\chi_{\text{s}}}{\chi_{\text{n}}}\right)}}, \tag{2.37}$$

where $g = 2$ for free electrons [30]. In the case of a spin triplet superconductor, $\chi_{\text{s}} = \chi_{\text{n}}$ and therefore, there is no Pauli paramagnetic limiting.

The upper critical field, B_{c2} within BCS theory in the dirty limit can be analysed using the Werthamer-Helfand-Hohenberg (WHH) model which considers both orbital and Pauli paramagnetic pair breaking effects [85, 86]. For several materials ξ_0 is large so that $B_{c2}^{orb} << \mu_0 H_p$ in the clean limit and therefore the dirty limit can be used in most cases where the paramagnetic limiting is considerable. In the dirty limit, because of the reduced l, ξ will be reduced and as a result B_{c2}^{orb} is large and the Pauli paramagnetic limiting should be considered. In the case of a superconductor which obeys the BCS theory in the dirty limit, the upper critical field can be calculated using

$$\ln\frac{1}{t} = \left(\frac{1}{2}+\frac{i\lambda_{so}}{4\delta}\right)\Psi\left(\frac{1}{2}+\frac{h+0.5\lambda_{so}+i\delta}{2t}\right)+\left(\frac{1}{2}-\frac{i\lambda_{so}}{4\delta}\right)\Psi\left(\frac{1}{2}+\frac{h+0.5\lambda_{so}-i\delta}{2t}\right)-\Psi(0.5), \tag{2.38}$$

where $t = T/T_c$ and h is a dimensionless form of the upper critical field given by

$$h = \frac{4B_{c2}}{\pi^2}\left(\frac{dB_{c2}}{dt}\right)^{-1}_{t=1}, \tag{2.39}$$

$\Psi(x)$ is the digamma function and δ is given by

$$\delta = \sqrt{(\alpha_M h)^2 - 0.25\lambda_{so}^2}, \tag{2.40}$$

where α_M is the Maki parameter and λ_{so} is the spin-orbit scattering parameter. These two parameters determine h.

A measure of the corresponding influence of Pauli paramagnetic pair breaking compared to orbital limiting is given by

$$\alpha_M = \sqrt{2}\left(\frac{B_{c2}^{orb}}{\mu_0 H_p}\right). \tag{2.41}$$

When there is no paramagnetic limiting or $B_{c2}^{orb} << \mu_0 H_p$, $\alpha_M = 0$. As a consequence, the upper critical field is given by

$$B_{c2}^{orb} \approx -0.693\left(\frac{dB_{c2}}{dt}\right)_{t=1}. \tag{2.42}$$

When α_M increases, the effect of paramagnetic pair limiting increases and as a consequence the upper critical field reduces below the orbital value. The scattering rate for spin flip processes is determined by λ_{so}. The paramagnetic limiting effect

is reduced by the effect of spin flip scattering. When $\alpha_{\mathrm{M}} = 0$, the upper critical field is not affected by λ_{so}. When α_{M} increases, the upper critical field reduces and the value of λ_{so} increases and as a result B_{c2} is moving towards the orbital value. By determining the gradient of the upper critical field close to the transition temperature from Eq. 2.39, the absolute values of the upper critical field within the WHH model can be obtained. The gradient is related to α_{M} by

$$\alpha_{\mathrm{M}} = 0.52758 \left(\frac{dB_{\mathrm{c2}}}{dT} \right)_{\mathrm{T=T_c}}, \tag{2.43}$$

where the slope is given in units of T/K. The WHH model can examine the role of paramagnetic limiting. When there is absence or decrease in H_{p}, evidence for unconventional pairing symmetries can be provided. The WHH model is derived from one band, weak coupling BCS theory and according to Eq. 2.37, H_{p} is more likely to increase in a strongly coupled system. Consequently, in order to decide whether paramagnetic pair breaking effects have been suppressed, a great orbital upper critical field is required.

2.9 Summary

This chapter outlines some of the properties of superconductors, focusing on theoretical ideas relevant to non-centrosymmetric superconductors. A brief overview of the phase transitions was provided in order to give a good understanding of ordered and disordered systems. The Ginzburg-Landau (GL) theory was presented and the BCS theory was introduced. This thesis is based on studies of non-centrosymmetric superconductors and as a consequence this chapter focuses on ideas relevant to studies undertaken in this area. The gap structure of non-centrosymmetric superconductors was presented briefly. The background theory of the thermodynamics properties of superconductors and the clean and dirty limits were explained. Lastly, the upper critical field was introduced in order to explain the general idea behind this term and state the main equations involved. This theoretical background chapter, together with the next one which introduces the experimental techniques used in this thesis, set the scene for the work presented in Chapter 4.

Chapter 3

Experimental Techniques

3.1 Sample Preparation

Polycrystalline samples of $Nb_{0.22}Re_{0.78}$ were produced by arc melting the constituent elements using a Centorr model 5TA tri-arc furnace. This furnace consists of upper and lower water-cooled sections separated by a pyrex observation tube. Three copper stinger rods are placed at the top section which carry tungsten electrodes. Each of these rods is mounted into a swivel ball in order to allow angular and vertical movement. The lower section has an opening allowing insertion of a variety of copper hearths as illustrated in Fig. 3.1 [2]. The appropriate amounts of the constituent materials corresponding to each compound, were placed on a water cooled copper hearth. The sample chamber was evacuated with a rotary pump and

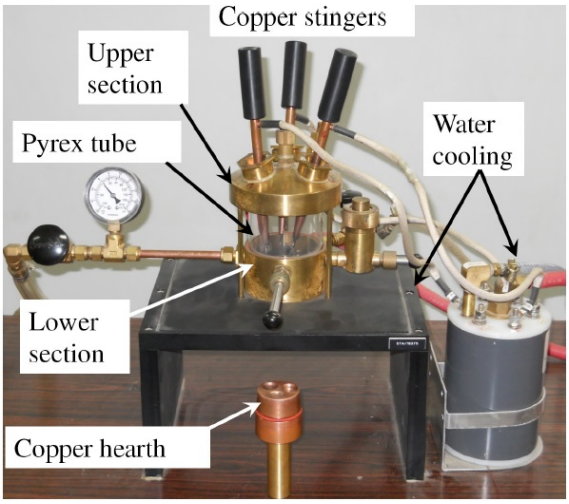

Figure 3.1: An annotated photograph of the Centorr model 5TA tri-arc furnace. The diagram was adapted from Ref. [2].

flushed with argon several times before melting began. A titanium (Ti) getter was melted before melting the constituent materials in order to ensure any oxygen is removed from the chamber. The samples were melted under a positive pressure of argon. The constituent materials of 99.99% purity are melted. Samples were flipped and remelted several times to improve homogeneity.

3.2 Sample Characterisation

There are several characterisation techniques that are used to identify the quality of the polycrystalline samples produced with the method introduced in the previous section. Two of the main techniques used are discussed in this section, Energy Dispersive X-ray Analysis (EDAX) which is used to determine the composition of the crystals and Powder X-ray Diffraction (XRD) which can be used to determine the structure including lattice parameters of carefully selected polycrystalline samples and also to check the phase purity of the materials.

3.2.1 Energy Dispersive X-ray Analysis

Energy Dispersive X-ray Analysis (EDAX) was used to determine the elemental composition of the alloys. EDAX measurements of the compounds were performed by Steve York at the University of Warwick using a JOEL6100 scanning electron microscope (SEM). The EDAX GENESIS analytical system was used and the spectra were taken at 10 kV, 2000 cps (cycles per second) and a count time of 100 s. The principle that this is based on is that the atoms of each cell have a unique electronic structure with characteristic binding energies of the electrons in different electronic levels. The number of x-ray photons and the energy of the same are measured with an energy dispersive analyser. The information from the analyser is used to provide a quantitative analysis of the elemental composition of the sample.

3.2.2 Powder X-ray Diffraction

Equipment Description

Powder X-ray Diffraction (XRD) was used to ascertain the phase purity and the lattice parameter, a, from a powder crystal diffractogram. The experiments on the materials were performed with the help of Simon Riberolles. For the presented diffractograms, a Bruker D5005 diffractometer was used which produces Cu K_α radiation. The average K_α wavelength of Cu element is around 1.5406 Å. The Bruker D5005 is equipped with standard Bragg-Brentano geometry, a diffracted

beam graphite monochromator and an Oxford Cryosystems PheniX low temperature stage which allows measurements to be carried out at down to room temperature. A typical 2θ scan ranged from 10 to 100 deg. The solid polycrystalline samples were ground into a fine powder by manually grinding them. The powder was carefully placed and packed into the sample holder.

Bragg's Law

The incident radiation is reflected by the parallel planes of atoms as given by Bragg's theory of diffraction. According to Bragg's law, constructive interference occurs when two waves are scattered in phase. In Fig. 3.2, a diagram of this principle is illustrated. If two waves, which penetrate a crystal lattice, are separated by an integer number of wavelengths, $n\lambda$ and the path difference of the two waves between the adjusted planes is δL, then the two waves will be in phase. The separation between successive planes is a distance indicated as d. The angle, θ of the incident x-ray is defined and as a result the scattering angle, 2θ can be calculated. Considering all of these statements, Eq. 3.1 illustrates Bragg's law and consequently, Bragg condition for constructive interference is:

$$n\lambda = 2d\sin\theta. \tag{3.1}$$

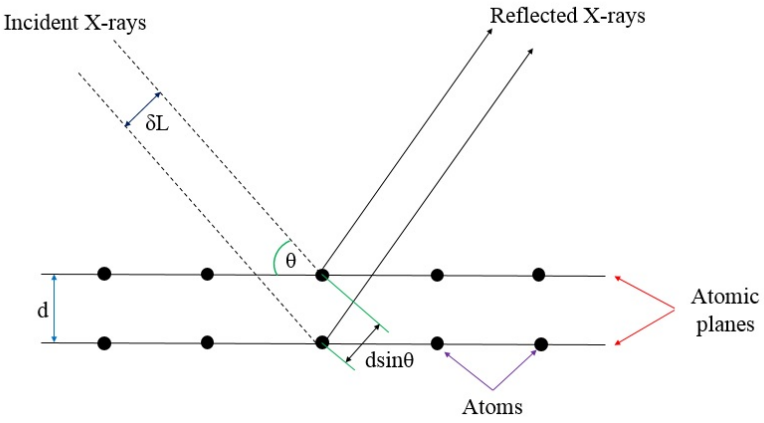

Figure 3.2: Two beams of x-rays scatter from atoms which are located on parallel planes within the crystal lattice and constructive interference occurs if $2d\sin\theta$ is equal to an integer value of the wavelength of the incident radiation.

3.3 Magnetization

3.3.1 SQUID Magnetometer

In the present work, magnetization measurements were carried out using a 50 kOe Quantum Design Magnetic Property Measurement System (MPMS-5S) Superconducting Quantum Interference Device (SQUID) magnetometer. The system was used to make high sensitivity DC magnetisation measurements in the temperature range 1.8 to 400 K. The system consists of a probe mounted in a dewar of helium-4, surrounded by a jacket filled with liquid nitrogen. Samples were mounted in a straw and were attached using Kapton tape and inserted vertically into the probe. The measurement system is illustrated in Fig. 3.3. The sample is moved in a second order gradiometer coil made of superconducting wire inducing a current. A typical measurement consists of measuring 32 points across a scan length of 4 cm. The change in current at each step is converted by the SQUID to an accurate voltage [87]. The output voltage as a function of position is fitted with a model of the response to a dipole field. The magnetization collected by the device was normalised for the density and mass of the sample. The maximum applied field that can be reached in the MPMS is 50 kOe.

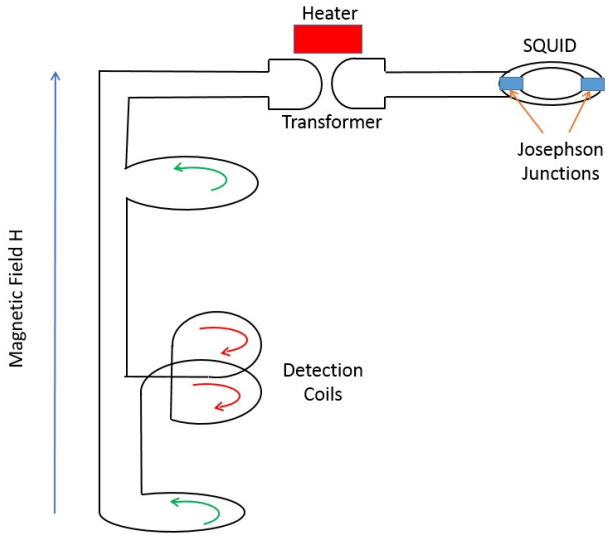

Figure 3.3: Schematic of the experimental configuration of the detection system in the MPMS-5S SQUID magnetometer. The green and red arrows show the flow of the induced current. The sample is placed between the two detection coils. The circuit is made of superconducting wire which is kept in the superconducting state, except when the heater is engaged [2].

3.3.2 Vibrating Sample Magnetometer

Magnetization versus field measurements at different temperatures were performed using an Oxford Instruments Vibrating Sample Magnetometer (VSM) with a 120 kOe superconducting solenoid. The system makes use of Oxford Instruments ITC503 temperature controller, IPS120 power supply and a Stanford Research Systems SR830 lock-in amplifier. The VSM can operate between 1.4 and 320 K using a standard Variable Temperature Insert (VTI). The sample is attached with General Electric (GE)-varnish to the Polyether Ether Ketone (PEEK) sample rod and then wrapped in Polytetrafluoroethylene (PTFE) tape to ensure that sample will remain in place. The sample oscillates vertically in a uniform magnetic field applied along the axis of vibration as shown in Fig. 3.4. The default settings of the sample's vibration frequency and amplitude are 55 Hz and 1.5 mm, respectively. The vibration of the sample causes a change in magnetic flux which induces a voltage in the detection coil. A lock-in technique is used in order to measure the induced voltage. Data were typically collected at a field sweep rate of 2.5 kOe/min.

There are many advantages of using the Vibrating Sample Magnetometer instead of the SQUID Magnetometer. The maximum applied field that can be reached

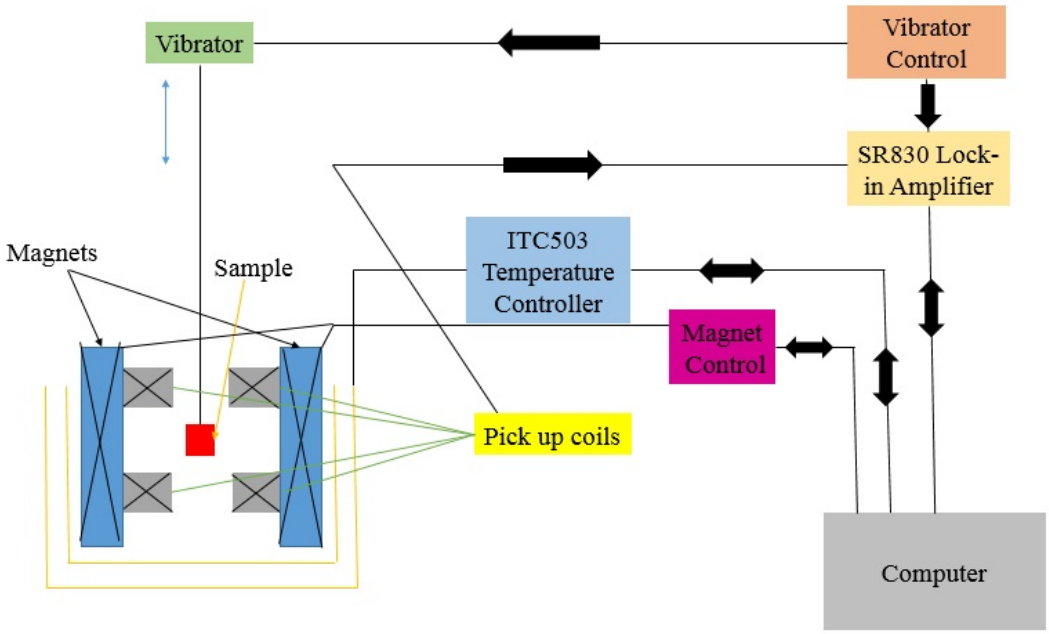

Figure 3.4: Schematic of the experimental configuration in the Vibrating Sample Magnetometer (VSM).

in the SQUID (50 kOe) is smaller than the one reached in the VSM (120 kOe). Additionally, the temperature range in the SQUID is 1.8 to 400 K while in the VSM is 1.4 to 320 K. However, it is quicker to change the applied field in the VSM compare with the SQUID. For example, if magnetisation measurements will be collected between 0 kOe to a maximum applied field and then from zero to a minimum applied field, it is preferable to use the VSM instead of the SQUID Magnetometer.

3.4 AC Resistivity

AC resistivity measurements were carried out using a Quantum Design Physical Properties Measurement System (AC Transport PPMS). The maximum field used was 90 kOe and the measurements were performed in the range 1.8 to 300 K. In this project, the four-probe technique is used. The materials were cut in bar shaped samples. Four silver wires of diameter 0.05 mm were attached to the surface, as illustrated in Fig. 3.5, using DuPont 4929N silver paste. Alternating current of 10 mA passes between the two outer contacts and the voltage is measured over a distance L between the two inner wires. According to Ohm's law, voltage, V equals

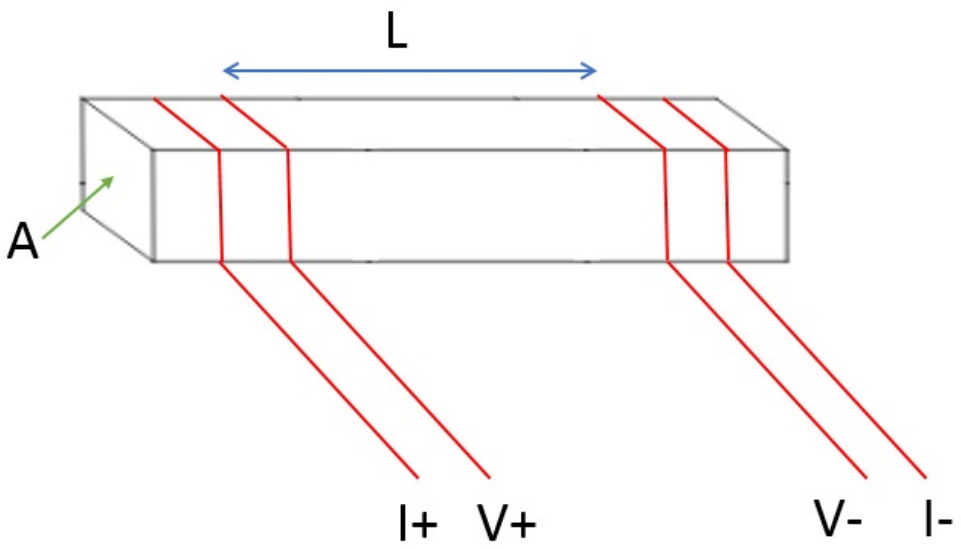

Figure 3.5: Schematic diagram of the sample for four probe resistivity measurement. Concept adapted from Ref. [2].

IR where I is the current and R is the resistance (Eq. 3.2). The resistivity (ρ) is calculated using the resistance (R) and the cross sectional area (A) as shown in Eq. 3.3.

$$R = \frac{V}{I} \tag{3.2}$$

$$\rho = \frac{RA}{L} \tag{3.3}$$

3.5 Specific Heat Capacity

The specific heat capacity was measured using a commercial Heat Capacity Quantum Design Physical Properties Measurement System (Heat Capacity PPMS). The temperatures used were between 1.8 and 300 K using a conventional Helium-4 system. Measurements were extended down to 0.4 K using a Helium-3 insert. Applied fields of up to 90 kOe were used with both set ups. The relaxation technique was used, whereby the sample is mounted on a sapphire platform using thermally conducting grease as illustrated in Fig. 3.6. This platform is supported by thin wires attached to a heat sink and a temperature sensor is mounted on the platform in order to monitor the temperature. A second thermometer is located in the puck frame. The wires allow an electrical connection to the components on the puck and also they create a thermal link between the isolated platform and the heat sink. The whole arrangement is covered by a thermal shield. The experiment is carried out in high vacuum.

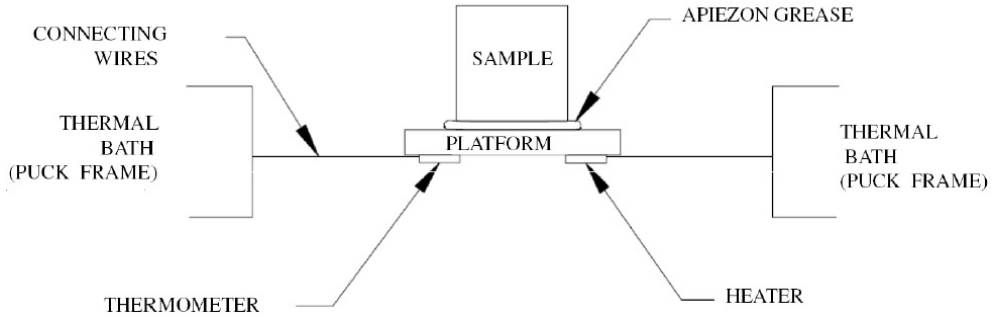

Figure 3.6: Schematic diagram of the sample mounting on the puck in PPMS Heat capacity. This diagram was adapted from Ref. [88].

The samples were polished in order to ensure that at least one face was completely flat. This flat polished face was mounted on the stage using Apiezon N grease to ensure a good thermal contact. The measurements were carried out by switching on the heater to heat the platform. The platform temperature was measured during the heating and cooling stages [2]. The relaxation of the platform and the sample can be fitted using exponential functions. In order to measure the accurate specific heat, addenda measurements of the stage and grease were made. The sample heat capacity was obtained by subtracting the measurements of heat capacity of the addenda from the total (stage+grease+sample). This procedure was repeated for each of the different fields applied.

Chapter 4

The compositions Nb_xRe_{1-x} in the range $0.22 \leq x \leq 0.34$.

4.1 Introduction

The non-centroymmetric compounds are interesting as they are good candidates for unconventional superconductors as explained above in Sections 1.1 and 1.2. The properties of polycrystalline Nb_xRe_{1-x} have been studied for some values of x [28, 59, 29] and indicated that Nb_xRe_{1-x} compounds display an isotropic s-wave superconducting state. The transition temperature ranges from around 3.5 K for $x = 0.38$ to around 8.8 K for $x = 0.18$. A moderately enhanced gap in $Nb_{0.18}Re_{0.82}$ was reported in Refs. [28, 59]. When the triplet component in non-centrosymmetric superconductors is small, the two gaps might be fully gapped and of a similar magnitude. In order to find out the gap structure in these materials, the superconducting and normal state properties of several compositions of Nb_xRe_{1-x} will be investigated.

In this chapter, carefully selected compositions of Nb_xRe_{1-x} for $0.22 \leq x \leq 0.34$ were prepared and their structure was investigated using powder x-ray diffraction. Additionally, the magnetic susceptibility, the lower critical field B_{c1}, the upper critical field B_{c2} and the thermal superconducting properties of these non-centrosymmetric compounds were studied using polycrystalline annealed and as-cast samples.

4.2 Sample preparation

Three compositions of Nb_xRe_{1-x} with close to the optimum transition temperatures, T_c were produced. $Nb_{0.18}Re_{0.82}$ has the highest obtained value of T_c compared with the other compositions when $x > 0.18$ [28, 2]. Polycrystalline samples of Nb_xRe_{1-x} for $x = 0.22$, 0.29, 0.34, where produced by arc-melting stoichiometric quantities of the constituent materials of 99.99% purity, in an argon atmosphere on a water cooled copper hearth as discussed in Section 3.1. The resulting samples were flipped and remelted to improve homogeneity. During arc-melting, the loss of mass of the materials was found to be negligible. The polycrystalline as-cast samples of Nb_xRe_{1-x} for $x = 0.29$, 0.34 and the polycrystalline annealed sample of $Nb_{0.22}Re_{0.78}$ were synthesized using the same method described by M. Smidman in reference [61]. The polycrystalline annealed sample was wrapped in tantalum foil and annealed at 900 °C for a week under a dynamic vacuum, better than 10^{-6} torr.

4.3 Sample characterization

4.3.1 Composition analysis

Composition analysis using EDAX was carried out on small pieces of polycrystalline samples in order to check that the samples produced were formed with the right amount of constituents. Data were obtained from different regions of each sample to ensure the homogeneity of the stoichiometry. Table 4.1 shows the results for Nb_xRe_{1-x} polycrystalline compounds with the nominal composition $x = 0.22$ (as cast and annealed), 0.29 and 0.34. The data suggested that the samples were formed with the correct stoichiometry for all the compositions.

Composition, x	**Nb**	**Re**
0.22 (as-cast)	21.7 ± 0.4	78.3 ± 1.6
0.22 (annealed)	20.5 ± 0.4	79.5 ± 1.6
0.29 (as-cast)	29.1 ± 0.6	70.9 ± 1.4
0.34 (as-cast)	33.3 ± 0.7	66.7 ± 1.3

Table 4.1: Representative compositions of polycrystalline samples of Nb_xRe_{1-x}, where $x = 0.22$ (as-cast and annealed), 0.29 and 0.34. All values are given in atomic percentages.

4.3.2 Structural characterization

In Ref. [28], powder x-ray diffraction (XRD) patterns were taken on the Nb_xRe_{1-x} samples with various x in the range $0.13 \leq x \leq 0.93$ at room temperature. According to these patterns, it was concluded that Nb_xRe_{1-x} crystallizes in three different structures. The three regions indicated are $0.13 \leq x \leq 0.38$ (region I), $0.38 < x \leq 0.52$ (region II) and $0.55 \leq x \leq 0.93$ (region III). For region II, Ref. [56] states that the Nb_7Re_8-type phase dominates (tetragonal, $P4_2/mnm$). The XRD patterns showed a Niobium phase with cubic $Im\bar{3}m$ space group for the region $0.55 \leq x \leq 0.93$ determining a maximum solubility of 46% Rhenium in Niobium. The region of interest is $0.13 \leq x \leq 0.38$ (region I) as the compounds produced in this project are in the range $0.22 \leq x \leq 0.34$. For this region, it was suggested that the XRD patterns showed that the samples had a single phase with a cubic Ti_5Re_{24} structure which was shown to be incorrect a few years later after an in-depth investigation of polycrystalline and single crystals of the composition $Nb_{0.18}Re_{0.82}$. As stated in Section 1.3, in Niobium-Rhenium series there are two phases occur, the σ and α-Mn structures. The α-Mn structure has a homogeneity range of $0.13 \leq x \leq 0.38$ [56]. As a result, the compounds investigated in this project are expected to have a single phase with cubic α-Mn structure.

In order to plot the unit cell volume as a function of x for various samples, the data from the patterns reported in Ref. [28] were used as the lattice parameter was only investigated for the as-cast polycrystalline sample of $Nb_{0.22}Re_{0.82}$ reported in this project. These data were extracted from the Rietveld refinements as shown in Ref. [28]. Fig. 4.1 represents the unit cell volume, V and the lattice parameter as a function of x. The unit cell volume is equal to the a^3 where a is the lattice parameter. In this project, the compounds used were $Nb_{0.22}Re_{0.78}$, $Nb_{0.29}Re_{0.71}$ and $Nb_{0.34}Re_{0.66}$. In Table. 4.2, the unit cell volume and the lattice parameter are shown for those compounds including the compound $Nb_{0.18}Re_{0.82}$.

Composition, x	**Volume,** V **(Å^3)**	**Lattice parameter,** a **(Å)**
0.18	898 ± 2.79	9.65 ± 0.01
0.22	910 ± 2.83	9.69 ± 0.01
0.29	920 ± 2.86	9.73 ± 0.01
0.34	930 ± 2.89	9.76 ± 0.01

Table 4.2: Unit cell volume and lattice parameter as a function of x for compositions Nb_xRe_{1-x} when $x = 0.18$, 0.22, 0.29 and 0.34.

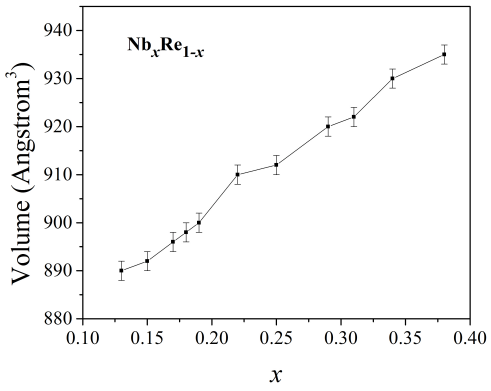

(a)

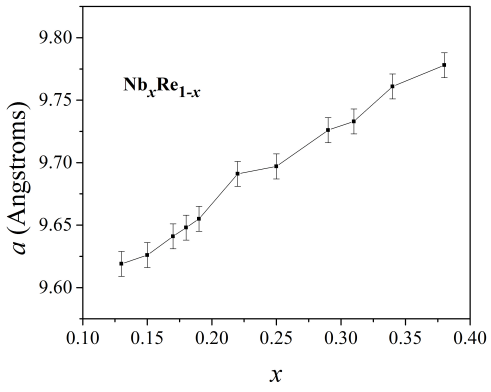

(b)

Figure 4.1: (a) Unit cell volume as a function of x for compositions Nb_xRe_{1-x} in the range $0.13 \leq x \leq 0.38$. The data were collected from Ref. [28]. (b) Lattice parameter as a function of x for compositions Nb_xRe_{1-x} in the range $0.13 \leq x \leq 0.38$.

The structure of the as-cast polycrystalline $Nb_{0.22}Re_{0.78}$ sample was investigated using powder x-ray diffraction, in order to verify that the lattice parameter value reported above in Table 4.2 is consistent with the one obtained for the produced as-cast polycrystalline $Nb_{0.22}Re_{0.78}$ sample. A small portion of the polycrystalline samples of this composition were isolated and ground into a fine powder for characterization. The room temperature powder x-ray pattern for fine powder of as-cast polycrystalline $Nb_{0.22}Re_{0.78}$ sample is shown in Fig. 4.2. The experimental data were analysed using the profile matching method which is based on Bragg's law (Eq. 3.1) and requires (i) the space group of the composition ($I\bar{4}3m$, No.217) and (ii) the wavelength of K_α radiation. In the figure, there are several peak positions

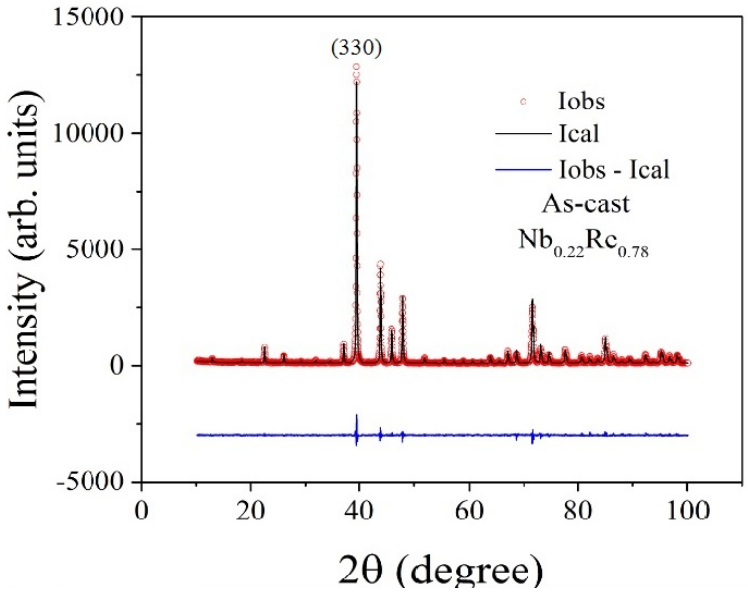

Figure 4.2: Powder x-ray diffraction measurements of as-cast polycrystalline $Nb_{0.22}Re_{0.78}$ sample measures using a Bruker D5005 difractometer. The black solid line through the experimental points show the data produced using profile matching. The blue solid line shows the differences between the experimental and calculated intensities.

shown. The profile matching confirmed the reported cubic α-Mn structure and the lattice parameter value calculated from peak position (330) is 9.67 ± 0.01 Å which agrees with the value of 9.65 ± 0.01 cited in literature [28]. The differences between the observed (I_{obs}) and calculated (I_{cal}) intensities for the profile matching to be ideal should be a horizontal straight line. In the figure below, the blue line indicates this difference (I_{obs}-I_{cal}). As you can see, it is almost a straight line and as a result the observed and calculated intensities match one another well.

4.4 Superconducting properties of Nb_xRe_{1-x} when $x = 0.22$, 0.29 and 0.34.

In this section, the properties that will be discussed are the transition temperatures, the lower and upper critical fields and the specific heat capacity of carefully selected compositions of Nb_xRe_{1-x} in the range $0.22 \leq x \leq 0.34$. For these compounds the properties will be compared in order to conclude in some general statements for the Niobium-Rhenium system.

4.4.1 Magnetic susceptibility

Magnetic susceptibility measurements as a function of temperature were used in order to determine the nature of superconducting phase transitions. Measurements were carried out on small pieces of the polycrystalline samples for each composition using a Quantum Design Magnetic Property Measurement System (MPMS) SQUID magnetometer. For more information about this measuring system refer to Section 3.2.1. Magnetization measurements were collected in an applied field of 20 Oe for a temperature range between 1.8 to 10 K.

Magnetic susceptibility is a dimensionless proportionality constant which indicates the degree of magnetization of a material with respect to an applied magnetic field as it is illustrated in the following relation,

$$\chi = \mathbf{M}/\mathbf{H}, \tag{4.1}$$

where $\mathbf{M}$ is the magnetization, $\mathbf{H}$ is the applied magnetic field and χ is the magnetic susceptibility. For the magnetization measurements, bar shaped samples were used which have well-defined dimensions in order to determine the demagnetization factors using the expression

$$\begin{aligned}
\pi D_z = \quad & \frac{b^2-c^2}{2bc}\ln\left(\frac{\sqrt{a^2+b^2+c^2}-a}{\sqrt{a^2+b^2+c^2}+a}\right) + \frac{a^2-c^2}{2ac}\ln\left(\frac{\sqrt{a^2+b^2+c^2}-b}{\sqrt{a^2+b^2+c^2}+b}\right) \\
+ \quad & \frac{b}{2c}\ln\left(\frac{\sqrt{a^2+b^2}+a}{\sqrt{a^2+b^2}-a}\right) + \frac{a}{2c}\ln\left(\frac{\sqrt{a^2+b^2}+b}{\sqrt{a^2+b^2}-b}\right) + \frac{c}{2a}\ln\left(\frac{\sqrt{b^2+c^2}-b}{\sqrt{b^2+c^2}+b}\right) \\
+ \quad & \frac{c}{2b}\ln\left(\frac{\sqrt{a^2+c^2}-a}{\sqrt{a^2+c^2}+a}\right) + 2\arctan\left(\frac{ab}{c\sqrt{a^2+b^2+c^2}}\right) \\
+ \quad & \frac{a^3+b^3-2c^3}{3abc} + \frac{a^2+b^2-2c^2}{3abc}\sqrt{a^2+b^2+c^2} + \frac{c}{ab}\left(\sqrt{a^2+c^2}+\sqrt{b^2+c^2}\right)
\end{aligned}$$

$$-\frac{\left(a^2+b^2\right)^{3/2}+\left(b^2+c^2\right)^{3/2}+\left(a^2+c^2\right)^{3/2}}{3abc}, \tag{4.2}$$

given in Ref. [69], where D_z is the demagnetization factor in z-axis, 2a, 2b, 2c are the dimensions of the sample along the x, y, z-axes. The field was applied along the z-axis. The estimations of demagnetization factors shown in Table 4.3 were applied to the collected data in order to correct the susceptibility where a value of -1 indicates the full flux expulsion.

Figure 4.4 shows the zero field cooled (ZFC) curves of the temperature dependence of magnetic susceptibility for annealed and as-cast polycrystalline samples of the composition Nb_xRe_{1-x} when $x = 0.22$, 0.29 and 0.34 without (a) and with (b) considering the demagnetization factors. The onset of superconductivity was indicated for annealed and as-cast $Nb_{0.22}Re_{0.78}$ samples at approximately 7.5 ± 0.2 K. For the as-cast samples of $Nb_{0.29}Re_{0.71}$ and $Nb_{0.34}Re_{0.66}$, superconductivity was observed at 5.1 ± 0.2 and 4.2 ± 0.2 K, respectively. The observed transition temperatures are in good agreement with the literature [28] as you can see in Fig. 4.3. The data shows that the superconducting transition temperature, T_c decreases with increasing x, with a maximum of 8.8 K for $x = 0.18$ reported to date. The transition

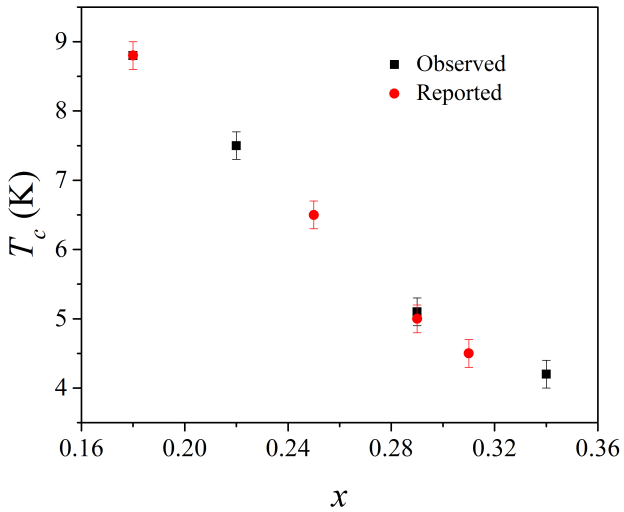

Figure 4.3: Illustration of the transition temperatures reported in Ref. [28] and the values observed in this project for several compositions of Nb_xRe_{1-x} in the range $0.18 \leq x \leq 0.34$ as a function of x.

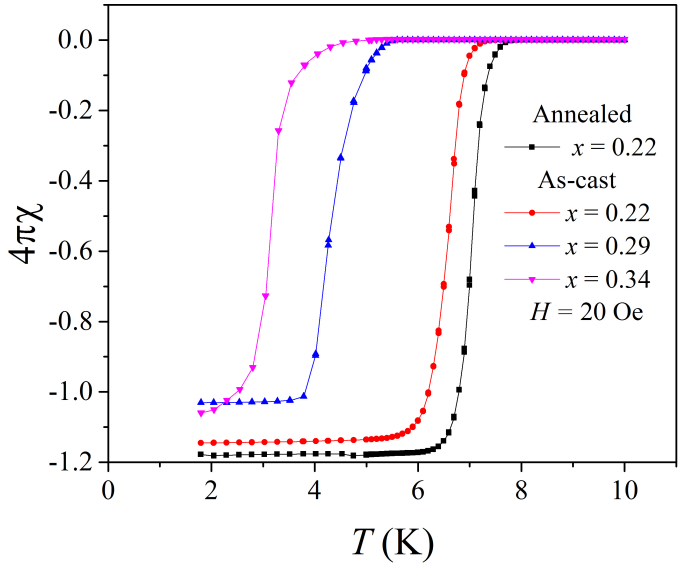

(a)

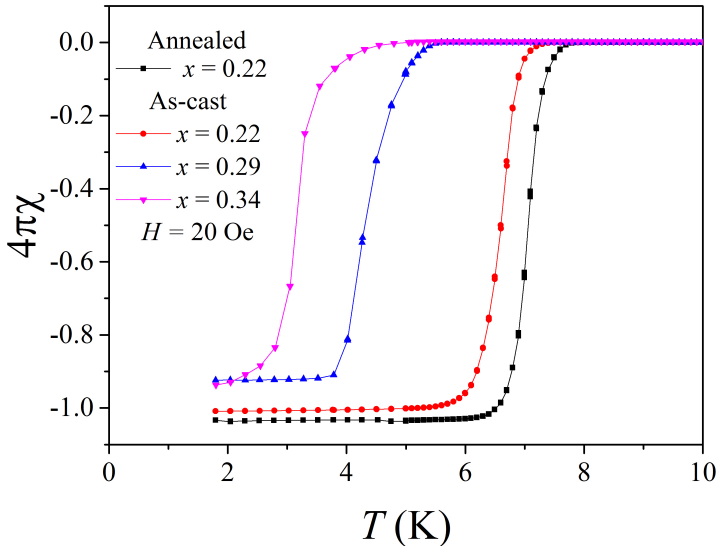

(b)

Figure 4.4: Zero field cooled (ZFC) curves of magnetic susceptibility as a function of temperature for the annealed $Nb_{0.22}Re_{0.78}$ and as-cast polycrystalline samples of Nb_xRe_{1-x} when $x = 0.22$, 0.29 and 0.34 without (a) and with (b) considering the demagnetization factors.

Composition, x	0.22 (as-cast)	0.22 (annealed)	0.29 (as cast)	0.34 (as-cast)
T_c ($\pm$0.2 K)	7.5	7.5	5.1	4.2
$4\pi\chi$ at 2 K ($\pm$0.02)	-1.17	-1.14	-1.03	-1.06
D_z	0.109	0.118	0.112	0.124
$4\pi\chi$ at 1.8 K	-1.03 ± 0.02	-1.03 ± 0.02	-0.92 ± 0.07	-0.94 ± 0.06

Table 4.3: Transition temperatures and magnetic susceptibility values with the estimations of demagnetization factors at which the superconducting transitions are observed for Nb_xRe_{1-x} in the range $0.22 \leq x \leq 0.34$.

temperatures of Rhenium and Niobium are 2.42 and 9.3 K which is suggesting that the transition temperature of the composition Nb_xRe_{1-x} would increases again until $x = 1$ [89].

According to Fig. 4.4(a), the curves reached $4\pi\chi = -1.17 \pm 0.02$ ($x = 0.22$ annealed), -1.14 ± 0.02 ($x = 0.22$ as-cast), -1.03 ± 0.02 ($x = 0.29$ as-cast) and -1.06 ± 0.02 ($x = 0.34$ as-cast) at 2 K. The demagnetization factors were applied to the curves so that $4\pi\chi = -1.03 \pm 0.02$ at 1.8 K for both annealed and as-cast samples of $Nb_{0.22}Re_{0.78}$ indicating complete flux expulsion. The susceptibility values of the as-cast $Nb_{0.29}Re_{0.71}$ and $Nb_{0.34}Re_{0.66}$ samples changed to $4\pi\chi = -0.92 \pm 0.07$ and -0.94 ± 0.06 at 1.8 K, respectively, indicating nearly complete flux expulsion within the error. A summary of the transition temperatures and the magnetic susceptibility values at which the superconducting transitions are observed for compositions Nb_xRe_{1-x} in the range $0.22 \leq x \leq 0.34$, are provided in Table 4.3.

4.4.2 Lower critical field

Type-II superconductors have two critical magnetic fields, the lower critical field, B_{c1} and the upper critical field, B_{c2}. As stated previously in Section 1.1, a superconductor is in the Meissner state below B_{c1} and T_c. The lower critical field indicates the onset of the mixed state. The lower critical magnetic field at 0 K $B_{c1}(0)$ can be estimated. The critical field decreases from this value with increasing temperature, reaching zero at the transition temperature.

The field dependence of magnetization for low applied fields at several temperatures for annealed and as-cast polycrystalline samples of Nb_xRe_{1-x} when $x = 0.22$, 0.29 and 0.34, were determined using a SQUID magnetometer. The data collected for an as-cast polycrystalline $Nb_{0.22}Re_{0.78}$ sample are presented in Fig. 4.5, as an example. The data collected for the four different samples have the same form. The

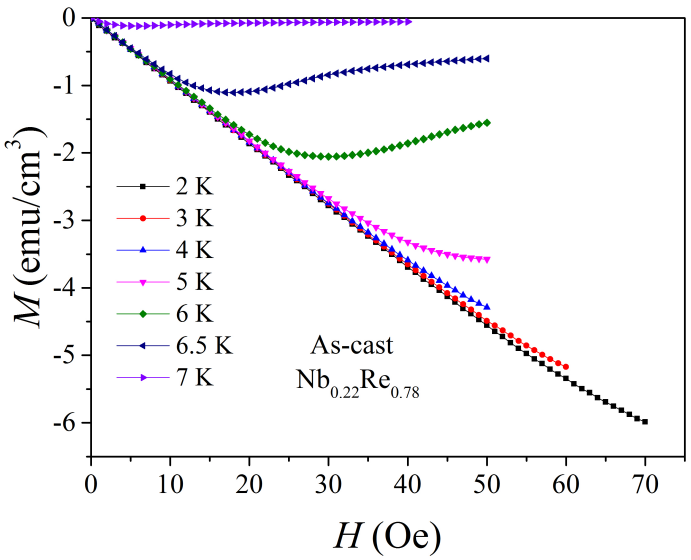

Figure 4.5: Magnetization as a function of field for low field applied at several temperatures for the as-cast polycrystalline $Nb_{0.22}Re_{0.78}$ sample.

curves are initially linear with gradient equivalent to full flux expulsion, i.e equivalent to a gradient -1 (see Fig. 4.5). When the applied fields exceed the lower critical field, magnetic flux penetrates the sample, perfect diamagnetism is lost and the susceptibility (gradient M/H) decreases before the curves eventually change gradient and turn up as discussed in Section 2.3.

The lower critical field, B_{c1} values were determined from the data collected at different temperatures by taking the field at which the curves deviate from the initial slope. The lower critical field, B_{c1} can be observed as a slight deviation from perfect diamagnetism. This deviation can be observed in our data by the subtraction of each point from the initial dependence of the magnetization on field as determined by the least-squares fit to the low-field data. Fig. 4.6 shows the deviation of magnetism from the initial linear behaviour for the data collected at 5 K shown in Fig. 4.5. It can be seen that the first deviation occurs at 29 ± 2 Oe, which is slightly smaller than the one observed in Fig. 4.5. Similar observations were made for each of the different temperatures applied for the four samples investigated.

This allowed the temperature dependence of the lower critical, $B_{c1}(T)$ to be determined for each composition as shown in Fig. 4.7. The applied field values were corrected using the demagnetization factors which actually means that the applied

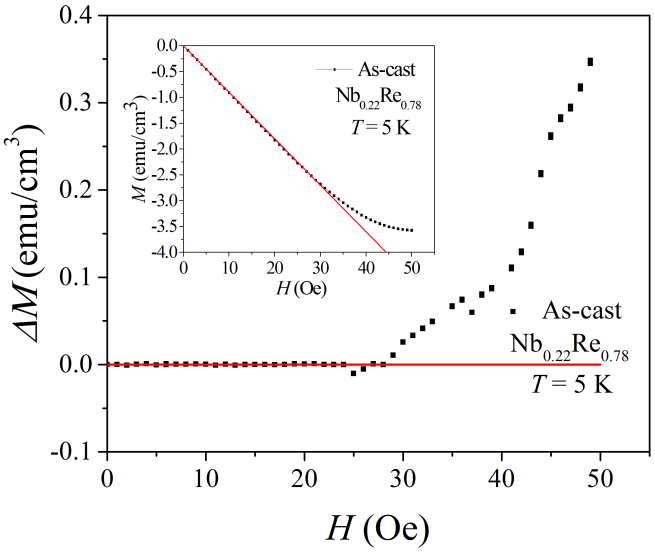

Figure 4.6: Deviation of the magnetization from the initial linear behaviour for the data collected at 5 K shown in Fig. 4.5. The inset presents the field dependence of magnetization at 5 K for the as-cast polycrystalline $Nb_{0.22}Re_{0.78}$ sample and the red solid straight line is a linear fit to the data with an initial slope of -0.09.

fields were scaled by a factor of $(1 - D)^{-1}$ to calculate B_{c1}. According to the well-defined dimensions the approximated values calculated for demagnetization factor, D are shown in Table 4.4. Using Eq. 2.9 for temperature dependence of lower critical field [2, 90] according to Ginzburg-Landau theory, the data were fitted in order to obtain the experimental values of the lower critical field at 0 K. The experimental values of $B_{c1}(0)$ obtained from the fitting for the annealed and as-cast samples of the compositions Nb_xRe_{1-x} for $x = 0.22$, 0.29 and 0.34, with the estimations of demagnetization factors calculated using demagnetization factor equation, are presented in Table 4.4. As you can see, there is a large difference at the lower critical field at 0 K between the annealed and the as-cast sample. This could be explained

Composition, x	**D-factor,** D_z	B_{c1}**(0) (G)**
0.22 (annealed)	0.118	78 ± 1
0.22 (as-cast)	0.109	66 ± 2
0.29 (as-cast)	0.112	47 ± 1
0.34 (as-cast)	0.124	42 ± 1

Table 4.4: Experimental values of $B_{c1}(0)$ for the annealed and as-cast samples of Nb_xRe_{1-x}, for $0.22 \leq x \leq 0.34$ with the estimations of demagnetization factor (D_z).

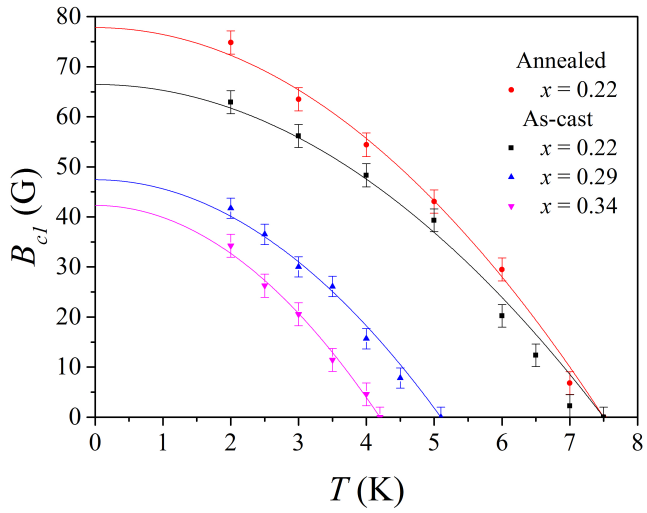

Figure 4.7: Lower critical field as a function of temperature for annealed and as-cast polycrystalline Nb_xRe_{1-x} samples when $x = 0.22$, 0.29 and 0.34 considering the demagnetization factors. The data were fitted using the expression 2.9 which can be derived using the Ginzburg-Landau theory.

as a result of the exposition of the sample at high temperatures which actually shows that after the annealing some of the superconducting properties of the sample are shown to be stronger.

4.4.3 Upper critical field

In this section, the transport properties of the non-centrosymmetric superconductors of Nb_xRe_{1-x} in the range $0.22 \leq x \leq 0.34$ will be discussed. The alternative current (AC) transport resistivity measurements were carried out using a Quantum Design Physical Properties Measurement System (PPMS) as explained in detail in Section 3.3. The resistivity as a function of temperature for several applied fields for all the samples used, was investigated in order to determine the upper critical field, B_{c2} (see Section 2.7). The applied fields ranged between 0 to 90 kOe. In Fig. 4.8 (a), the resistivity as a function of temperature for the polycrystalline annealed $Nb_{0.22}Re_{0.78}$ sample is illustrated as an example of the data collected. The data were normalised at 7 K for the compositions $Nb_{0.22}Re_{0.78}$ and $Nb_{0.29}Re_{0.71}$ in order to have a maximum normalised resistivity (ρ/ρ_{7K}) of 1. The normalised data for the polycrystalline annealed $Nb_{0.22}Re_{0.78}$ sample are presented in Fig. 4.8(b).

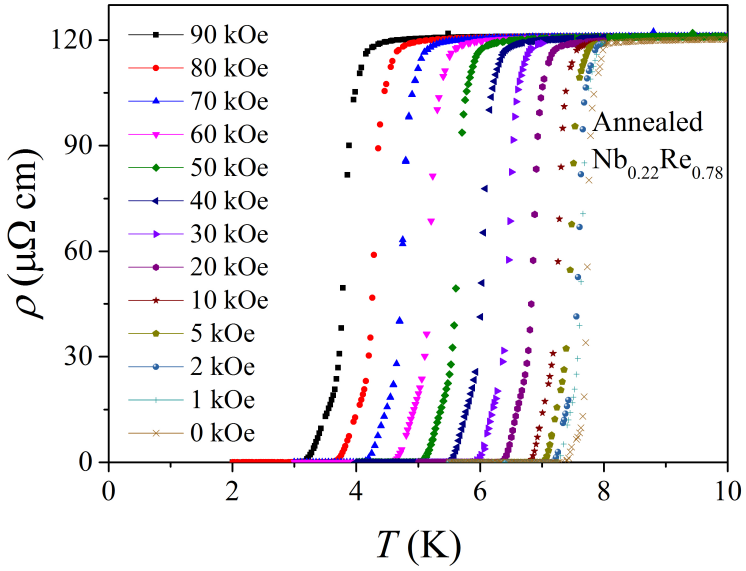

(a)

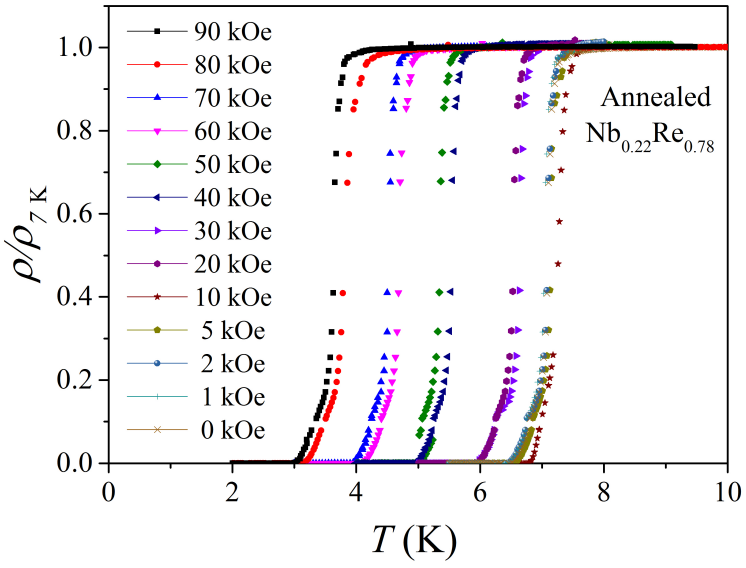

(b)

Figure 4.8: AC resistivity (a) and the normalised data at 7 K (b) as a function of temperature at different applied fields for the annealed polycrystalline $Nb_{0.22}Re_{0.78}$ sample.

The transition is relatively sharp in zero-field for the polycrystalline annealed $Nb_{0.22}Re_{0.78}$ sample (see Fig. 4.8) which within the error agrees with the magnetic susceptibility data. When the applied field increases, the transition broadens. The transition temperature T_c decreases as the applied field increases which shows an inverted symmetry between these two parameters. For example, when the applied field is 90 kOe, T_c^{onset} is 3.9 ± 0.2 K. Consequently, the transition temperature difference in zero and 90 kOe applied field, ΔT_c for the polycrystalline annealed $Nb_{0.22}Re_{0.78}$ sample is approximately 4 K. For the as-cast polycrystalline $Nb_{0.22}Re_{0.78}$ sample, the transition temperature is lower at around 7.7 ± 0.2 K which also within the error agrees with the magnetization measurements. This difference in transition temperature might be due to the variations of stoichiometry of the samples. According to Figs. 4.8(a) and 4.9, the maximum AC transport resistivity of the annealed polycrystalline sample of this composition reached in zero field applied, was $\rho_0 = 120 \pm 2$ $\mu\Omega$cm which is almost 40% greater than the maximum value observed for the as-cast polycrystalline $Nb_{0.22}Re_{0.78}$ sample ($\rho_0 = 88 \pm 1$ $\mu\Omega$cm). The annealed sample has a higher resistivity in zero field applied than the as-cast sample because It was annealed at 900 °C which it is assumed to affect some of the superconducting properties like this one.

The resistivity (ρ) as a function of temperature (T) of the annealed and as-cast polycrystalline samples of composition $Nb_{0.22}Re_{0.78}$ in zero-field ($H = 0$ kOe) from 300 K down to 2 K are shown in Fig. 4.9. A sharp zero-field superconducting transition is observed at 7.4 ± 0.3 K for both samples. For the annealed polycrystalline $Nb_{0.22}Re_{0.78}$ sample, the resistivity at 10 K before entering the superconducting state is $\rho_0 = 120 \pm 2$ $\mu\Omega$cm and the residual resistivity ratio $RRR = \rho(300\ K)/\rho(10\ K) = 1.1$. For the as-cast polycrystalline $Nb_{0.22}Re_{0.78}$ sample, $\rho_0 = 88 \pm 1$ $\mu\Omega$cm at 10 K in zero magnetic field applied and $RRR = \rho(300\ K)/\rho(10\ K) = 1.08$. The two residual resistivity ratios are in good agreement with each other. The residual resistivity ratios are close to 1 which shows that the samples are poor metals with a lot of disorder hence a lot of disorder scattering. A similar behaviour in the temperature dependence of resistivity for $0 \leq T \leq 300$ K it was reported in recent research findings on other Rhenium compounds including Re_6Hf, Re_3W and Re_6Zr [42, 50, 91]. For the compound Re_6Hf, the resistivity increases with temperature starting at $\rho(0) \approx 100$ $\mu\Omega$cm and reaching at around 159 $\mu\Omega$cm at 300 K. For the composition Re_3W two different phases were observed; however, the behaviour shown in Fig. 4.9 agrees only with the non-centrosymmetric cubic phase shown in Ref. [42].

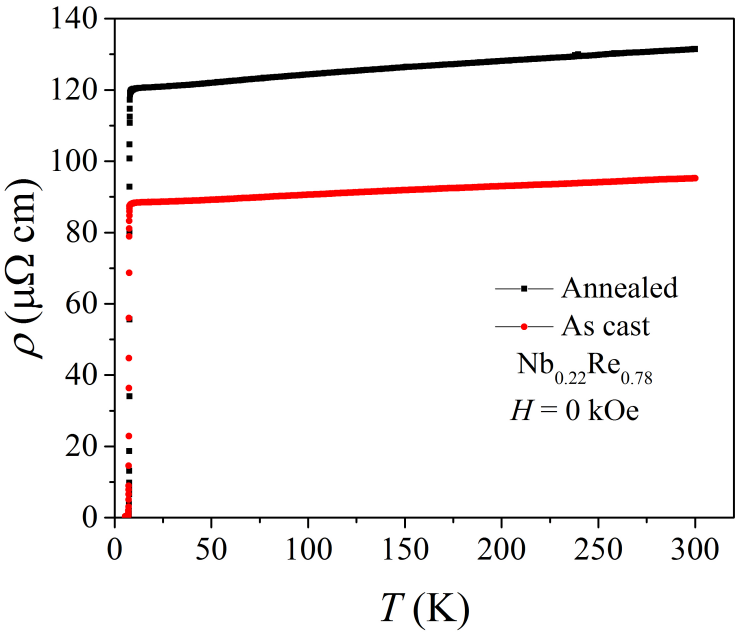

Figure 4.9: Electrical resistivity, ρ of annealed and as-cast polycrystalline $Nb_{0.22}Re_{0.78}$ samples versus temperature, T measured in zero applied magnetic field in the temperature range 2-300 K.

For the annealed and as-cast polycrystalline $Nb_{0.22}Re_{0.78}$ samples, the field dependence of resistivity was investigated at 8 and 10 K (see Figs. 4.10 and 4.9). At 8 K, the data were collected for the 0, 1, 2, 5, 10, 20, 40, 50, 70, 80 and 90 kOe fields applied and the curves are parabolic with positive gradient. Consequently, as the applied field increases, the AC resistivity decreases non-linearly. At 10 K, the curve shows only two points for low fields applied (0-50 kOe) and for high fields applied (50-90 kOe), the curve shows only 4 points. As a result it is difficult to comment on the form of the curve. When the applied field was 0 kOe and $T = 10$ K, the AC resistivity (ρ_0) is approximately 120 ± 2 and 88 ± 1 $\mu\Omega$cm for the annealed and as-cast polycrystalline $Nb_{0.22}Re_{0.78}$ samples, respectively. At $T = 8$ K and in zero field applied the AC resistivity (ρ_0) is approximately 119 ± 2 and 87 ± 1 $\mu\Omega$cm for the annealed and as-cast polycrystalline $Nb_{0.22}Re_{0.78}$ samples, respectively. The values of $\rho(0)$ at 8 and 10 K for both samples are in good agreement with the values observed from Figs. 4.8 and 4.9 above. The resistivity increases with applied field and as a result there is a small positive magnetoresistance (MR) of about 2% which is quite normal for this materials [92].

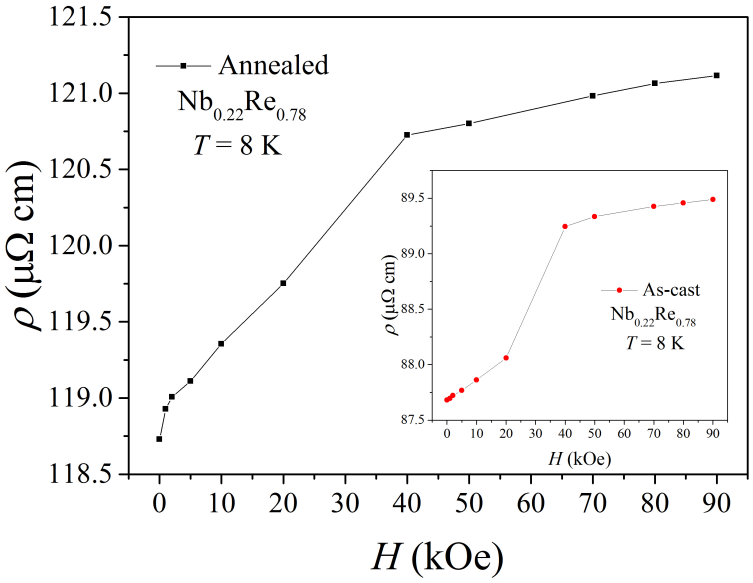

(a)

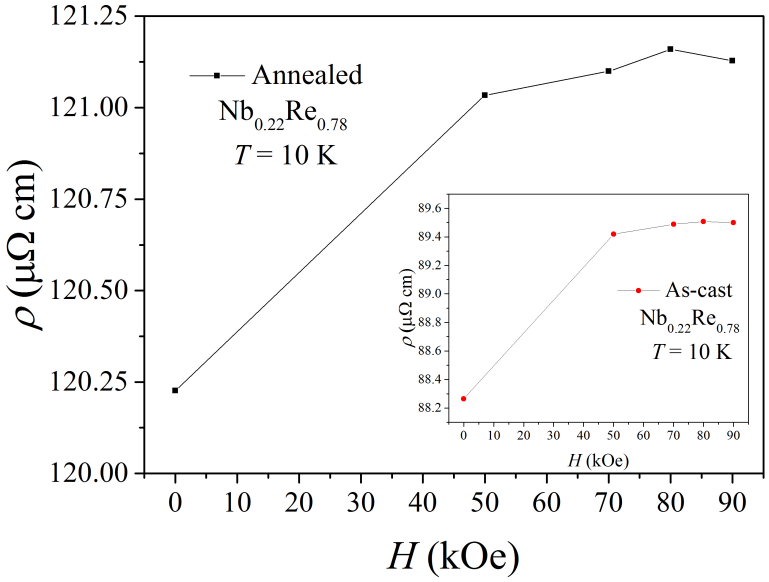

(b)

Figure 4.10: AC resistivity as a function of applied field at (a) 8 K and (b) 10 K when fields applied range between 0 and 90 kOe for the annealed and as-cast polycrystalline $Nb_{0.22}Re_{0.78}$ samples.

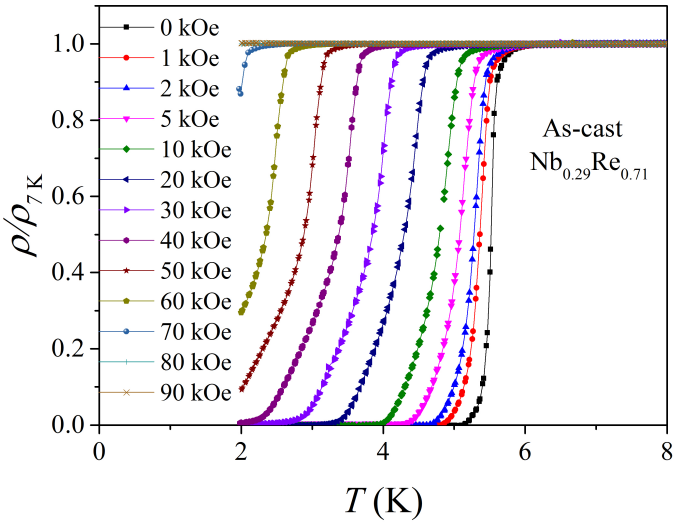

Figure 4.11: Temperature dependence of the normalised AC transport resistivity measurements at different applied fields range between 0 and 90 kOe for the as-cast polycrystalline $Nb_{0.29}Re_{0.71}$ sample. The data were normalised at 7 K.

For the as-cast polycrystalline $Nb_{0.29}Re_{0.71}$ sample, the resistivity normalised data as a function of temperature are illustrated in Fig. 4.11. The curves show similar behaviour with Fig. 4.8(b) for lower fields applied and slightly different behaviour for higher applied fields such as 90, 80 and 70 kOe. For this composition there is a sharp onset of superconductivity at around 5.5 ± 0.3 K which within the error it is consistent with magnetization data and the data reported in Ref. [28]. This composition has a lower transition temperature than the one observed for $x = 0.22$. Because of this, the form of the curves in Fig. 4.11 is different than the format observed for the $x = 0.22$ when large magnetic fields applied. To be precise, when the applied fields are above 70 kOe, the onset of superconductivity occurs below the minimum available temperature on AC Transport PPMS which is 2 K. The maximum AC transport resistivity value observed at zero field applied for the as-cast polycrystalline $Nb_{0.29}Re_{0.71}$ sample is $\rho_0 = 76 \pm 3$ $\mu\Omega$cm which is half the value reported in Ref. [28] which may be a result of the homogeneity this sample has. This sample is more homogeneous than the one investigated in Ref. [28].

Finally, the AC transport resistivity of the as-cast polycrystalline $Nb_{0.34}Re_{0.66}$ was investigated. In this case, the data were normalised at 6 K as the transition temperature of this compound is lower. For this compound, there is an onset of

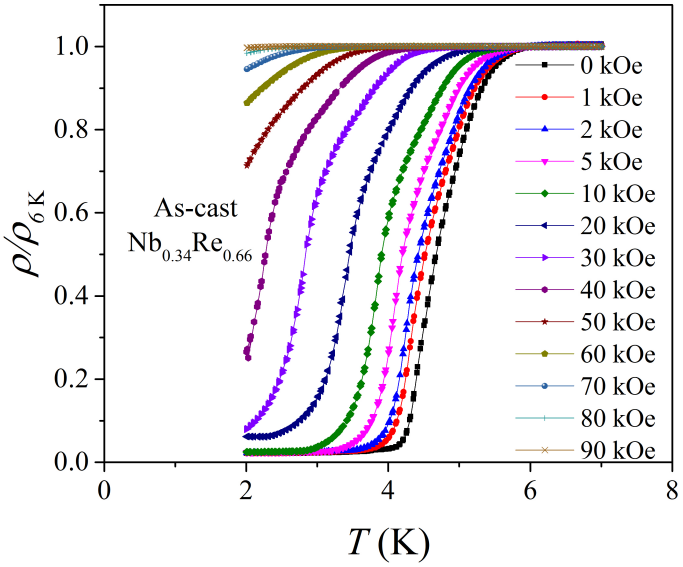

Figure 4.12: Temperature dependence of the normalised AC transport resistivity measurements at different applied fields range between 0 and 90 kOe for the as-cast polycrystalline $Nb_{0.34}Re_{0.66}$ sample. The data were normalised at 6 K.

superconductivity at around 4.7 ± 0.4 K as shown in Fig. 4.12, which agrees with the magnetic susceptibility and magnetization measurements within the error. The resistivity never reaches zero. Even at low applied fields the data are reaching a minimum of $\rho/\rho_{6K} = 0.02$. The origin of this effect is still not known. At an applied field of 20 kOe, there is a jump to a higher ρ/ρ_{6K} value. This shows that as the alternative current increases, the resistance increases according to Ohm's law.

The upper critical field can be verified by measuring the magnetization as a function of applied fields for constant temperatures using a Vibrating Sample Magnetometer(VSM). As an example, the magnetization as a function of applied fields at several temperatures for the annealed polycrystalline $Nb_{0.22}Re_{0.78}$ sample was investigated. The magnetization measurement collected at 5, 6, 6.5 and 7 K for this sample are presented in Fig. 4.13. The system is shown to be in a superconducting state up to 50 kOe at 5 K. There is a hysteresis loop of a type-II superconductor up to 5 kOe. In this field regime between 5 and 50 kOe the magnetization is reversible. The upper critical field, B_{c2} from these data can be determined by indicating the field at which the gradient of the loops change. This procedure was repeated for each different temperature used. At these temperatures, the upper critical field

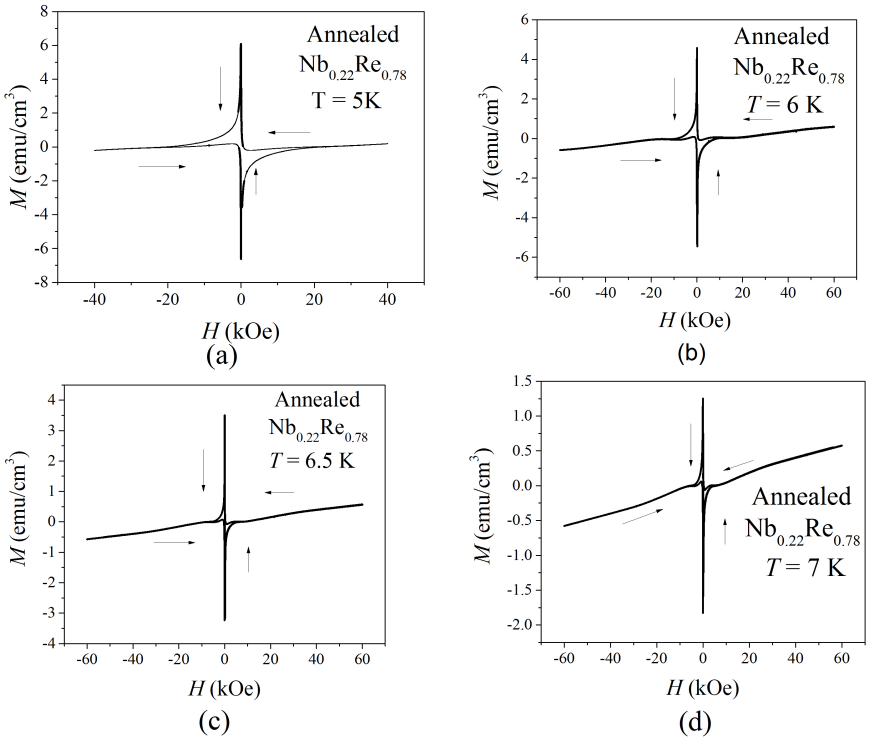

Figure 4.13: Magnetization as a function of applied field for an annealed polycrystalline sample of $Nb_{0.22}Re_{0.78}$ at 5, 6, 6.5 and 7 K. The arrows on the figures show how the data were collected starting from the first loop between 0 to 50 kOe, then 50 to 0 kOe (second loop), 0 to -50 kOe (third loop) and -50 to 0 kOe (fourth loop).

values determined for 6, 6.5 and 7 K are in good agreement with the values observed from resistivity measurements at these temperatures. For lower temperatures than 6 K, the upper critical field was located at fields outside the range of fields studied.

The upper critical field values for each different field applied were determined by the temperature at the onset of superconductivity (T_c^{onset}) for all the samples. The data were analysed using two different theories, the Ginzburg-Landau theory and the Werthamer-Helfand-Hohenberg (WHH) model in the dirty limit. By fitting the data according to the Ginzburg-Landau theory and consequently using equation,

$$B_{c2}(T) = B_{c2}(0)\left(\frac{1-\frac{T}{T_c}^2}{1+\frac{T}{T_c}^2}\right), \tag{4.3}$$

from Refs. [28, 63, 67, 70], the upper critical field values at 0 K, $B_{c2}(0)$ were determined. Fig. 4.14 shows the temperature dependence of upper critical field according to Ginzburg-Landau theory and Werthamer-Helfand-Hohenberg (WHH) model for

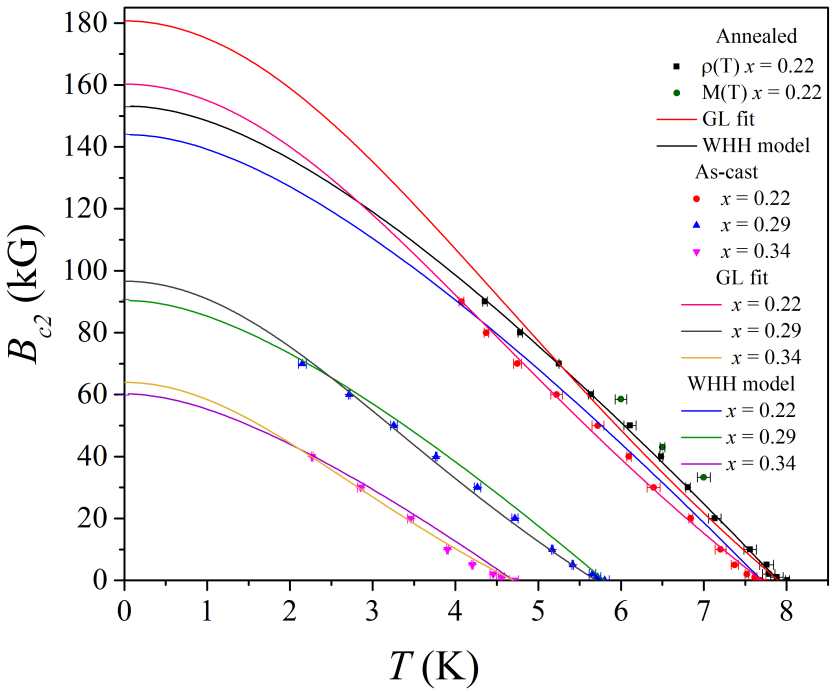

Figure 4.14: Temperature dependence of the upper critical field according to Ginzburg-Landau theory (GL Theory) and Werthamer-Helfand-Hohenberg (WHH) model for polycrystalline annealed and as-cast samples of composition of Nb_xRe_{1-x} in the range $0.22 \leq x \leq 0.34$. The upper critical field values observed from magnetization measurements for the annealed polycrystalline $Nb_{0.22}Re_{0.78}$ sample were also included in the plot. For the rest of the compounds, the upper critical field values plotted were collected only from resistivity measurements. In this figure simulations using the WHH model in the dirty limit when $\alpha = 0$, $\lambda = 0$ and $dB_{c2}/dT = 1$ for the temperature dependence of the upper critical field are shown.

annealed and as-cast composition Nb_xRe_{1-x} for $x = 0.22$, 0.29 and 0.34 using the data collected from all the methods described above. The $B_2(0)$ values obtained from the GL theory fitting for each compound are 181 ± 1, 160 ± 2, 97 ± 1 and 64 ± 2 kG for $x = 0.22$ (annealed and as-cast), 0.29 and 0.34, respectively. For the Ginzburg-Landau theory to fit the data the initial slope required is 1, consequently a straight line. As you can see, the formula generally fits the data for slightly lower temperatures than the transition temperature, (T_c). As it approaches T_c, the data are not fitted properly as they show a curvature.

As a consequence, a different approach to fit the upper critical field data was required. The WHH model in the dirty limit can be calculated using Eq. 2.38, as it is described in Section 2.8. A simulation of the model when $\alpha = 0$, $\lambda = 0$ and the

gradient of the data (dB_{c2}/dT) equals to 1, was created. Using this simulation and Eq. 2.42, an approximate value of the gradient for each set of data collected and the data were forced to fit the simulation of the model. The simulations with the experimental data collected for each composition used in this project are shown in Fig. 4.14. The values for upper critical field at 0 K, $B_{c2}^{orb}(0)$ for the four samples are 153 ± 17, 144 ± 14, 88 ± 17 and 60 ± 10 kG for $x = 0.22$ (annealed and as-cast), 0.29 and 0.34, respectively. In Ref. [28], the $B_2(0)$ and $B_{c2}^{orb}(0)$ values calculated for $x = 0.29$ were 118 kG and 86 kG, respectively. $B_2(0)$ value is greater than the one observed in the present work and $B_{c2}^{orb}(0)$ value agrees with the one observed. The upper critical field value using the Ginzburg-Landau theory reported in literature was calculated using the appropriate expression while in the present work this value was observed from the fittings. As you can see, the data are following the WHH model only for temperatures close to T_c for the annealed and as-cast samples of $Nb_{0.22}Re_{0.78}$. For the as-cast polycrystalline $Nb_{0.29}Re_{0.71}$ and $Nb_{0.34}Re_{0.66}$ samples, it is obvious that even when the data are forced to follow the WHH model in the dirty limit, they show a slightly different behaviour. This is more visible for the data collected for the as-cast polycrystalline $Nb_{0.34}Re_{0.66}$.

A number of important parameters can be calculated using the lower and upper critical fields such as coherence length (ξ), Ginzburg-Landau parameter (κ) and penetration depth (λ). Using the upper critical field values and Eq. 2.12, the Ginzburg-Landau coherence length ξ was calculated for the annealed and as-cast polycrystalline Nb_xRe_{1-x} samples for $x = 0.22$, 0.29 and 0.34. The coherence lengthvalues obtained for all the compounds investigated in this section are listed in Table 4.5. Using both critical fields (lower and upper), the Ginzburg-Landau parameter κ could be estimated. Parameter κ is exponentially proportional to the ratio of the lower

Composition x	**Coherence length, ξ (nm)**	**Ginzburg-Landau parameter κ (no units)**	**Penetration depth λ (nm)**
0.22 (annealed)	4.27 ± 0.02	70 ± 1	300 ± 6
0.18 (as-cast)	4.00 ± 0.02	79 ± 1	318 ± 2
0.22 (as-cast)	4.54 ± 0.06	72 ± 3	327 ± 7
0.29 (as-cast)	5.83 ± 0.06	66 ± 2	383 ± 5
0.34 (as-cast)	7.17 ± 0.22	55 ± 3	397 ± 4

Table 4.5: Derived superconducting and normal-state parameters for the annealed and as-cast polycrystalline Nb_xRe_{1-x} samples for $x = 0.18$, 0.22, 0.29 and 0.34 using the magnetization and AC transport resistivity data. The values presented for the polycrystalline as-cast $Nb_{0.18}Re_{0.82}$ sample are collected from Ref. [28]. ξ: Ginzburg-Landau coherence length; κ: Ginzburg-Landau parameter; λ: London penetration depth.

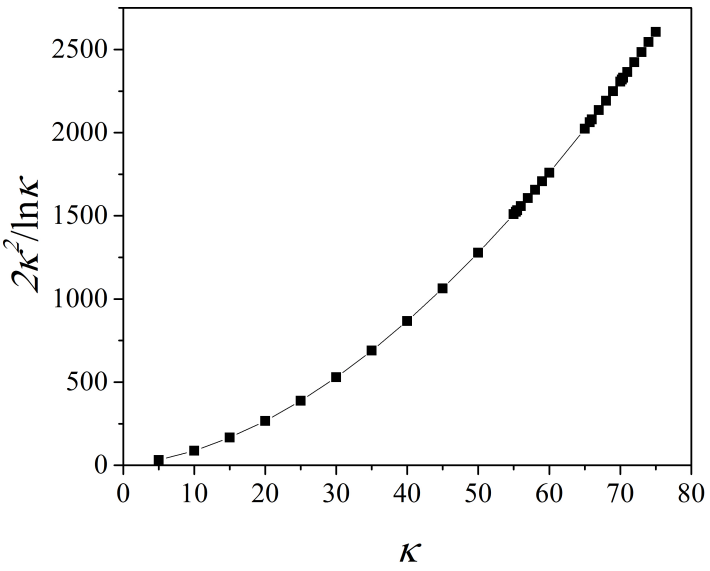

Figure 4.15: Ginzburg-Landau parameter, κ dependence of the fraction $2\kappa^2/\ln\kappa$ for $5 \leq \kappa \leq 75$.

and upper critical fields B_{c2}^{orb}/B_{c1} as shown in Eq. 2.14. Using this ratio and Fig. 4.15 which shows $2\kappa^2/\ln\kappa$ as a function of κ for $5 \leq \kappa \leq 75$, κ value were estimated for x = 0.22 (annealed and as-cast), 0.29 and 0.34 (see Table 4.5). In order to determine the penetration depth λ, the coherence length and parameter κ are required along with Eq. 2.10. The penetration depth values for the compounds Nb_xRe_{1-x} when x = 0.22 (annealed and as-cast), 0.29 and 0.34 are also presented in Table 4.5. The values of these parameters estimated for each of the compounds investigated in this Section are presented in Table 4.5. As the composition, x increases the values of these parameters increase as well.

4.4.4 Specific heat capacity

The specific heat capacity as a function of temperature for different applied fields of as-cast polycrystalline $Nb_{0.22}Re_{0.78}$ sample was investigated using a heat capacity Physical Properties Measurement System (Heat Capacity PPMS) which is discussed in Section 3.4. The applied fields range between zero and 90 kOe. In zero applied field, there is a jump in the specific heat as shown in fig. 4.16 which indicates the onset of bulk superconductivity with transition temperature, $T_c = 7.4 \pm 0.3$ K. This value is in good agreement with the magnetization and resistivity measurements reported in the previous sections. As the applied field increases, the transition

temperature decreases but a superconducting transition is still observed even at 90 kOe, which indicates that the upper critical field exceeds this value at 0 K. Fig. 4.16(a) shows C/T against T for the as-cast polycrystalline $Nb_{0.22}Re_{0.78}$ when the applied fields are 0, 10, 30, 50, 70 and 90 kOe. C/T against T^2 is shown in Fig. 4.16(b). For higher fields the peak shifts to lower temperatures and the $T_c(H)$ values agree well with the critical temperatures extracted from the resistivity measurements. At very low temperatures and in higher fields there is an upturn in C/T at base temperature. This appears most clearly in the 90 kOe data and is attributed to a hyperfine contribution to the heat capacity from the Rhenium [93].

A linear behaviour is observed in C/T versus T^2 above the transition temperature, T_c for each field applied. The data between 3.8 and 10 K were collected and presented in Fig. 4.17 with the appropriate fits. As you can see the jump shown in Fig. 4.16 is not visible in Fig. 4.17 because it exists at very small temperatures and at very small C/T ratios. If the figure was zoomed between 0 to 10 mJ/molK^2 and between 0 to 10 K, this jump will still be visible. The data were fitted using a slightly different version of Eq. 2.28. In this case the data were fitted using,

$$C = \gamma T + \beta T^3 + \delta T^5, \tag{4.4}$$

where δ is an additional constant term. As you can see the data were fitted for different temperature ranges in order to determine the heat capacity coefficients γ, β and δ. Sommerfeld electronic heat capacity coefficient, γ ranges between 4.00 ± 0.03 and 4.67 ± 0.04 mJ/molK^2, while Debye T^3-law lattice coefficient, β is in the range $0.06 \pm 0.01 \leq \beta \leq 0.04 \pm 0.01$ mJ/molK^4. The additional constant coefficient, δ values range between $1.01 \pm 0.01 \times 10^{-4}$ and $2.26 \pm 0.0001 \times 10^{-4}$ mJ/molK^6. These values are shown in Tab. 4.6.

Using the β values, the Debye temperature (Θ_D) can be calculated using Eq. 2.24, yielding Θ_D values that vary between 319 ± 20 to 365 ± 30 K for β equal to 0.06 ± 0.01 and 0.04 ± 0.01 mJ/molK^4, respectively. Fig. 4.18 shows the temperature dependence of the specific heat capacity of a polycrystalline as-cast $Nb_{0.22}Re_{0.78}$ sample for temperatures in the range 1.5 to 300 K. The measured normal state specific heat capacity at 300 K, $C_p(T = 300\text{ K}) = 24.07 \pm 0.26$ J/molK in Fig. 4.18 is close to the expected Dulong-Petit high-T limiting value $C_v = 3nR = 3R = 24.93$ J/molK.

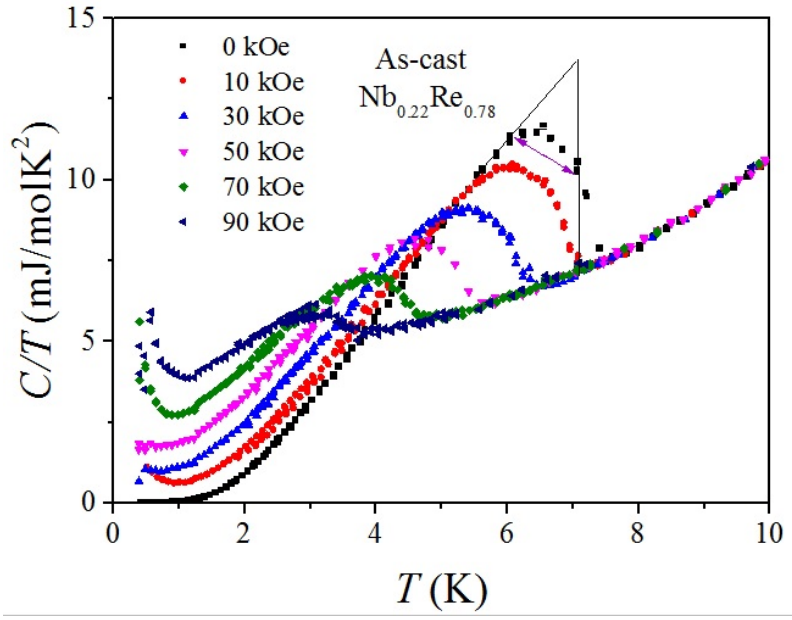

(a)

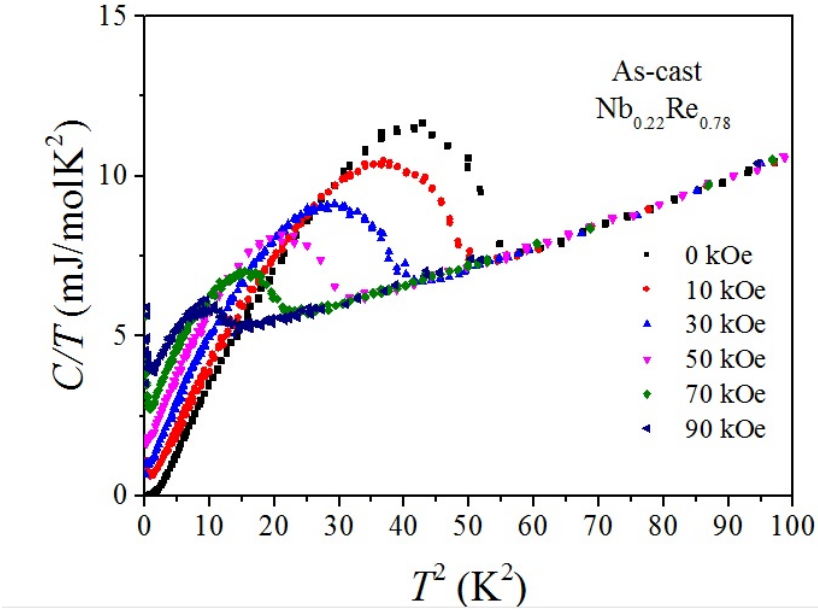

(b)

Figure 4.16: Temperature dependence of specific heat capacity of a polycrystalline as-cast sample of $Nb_{0.22}Re_{0.78}$ in applied fields between 0 to 90 kOe. C/T against T is illustrated in (a) and C/T against T^2 in (b). The purple arrow in (a) shows where the jump ΔC was obtained.

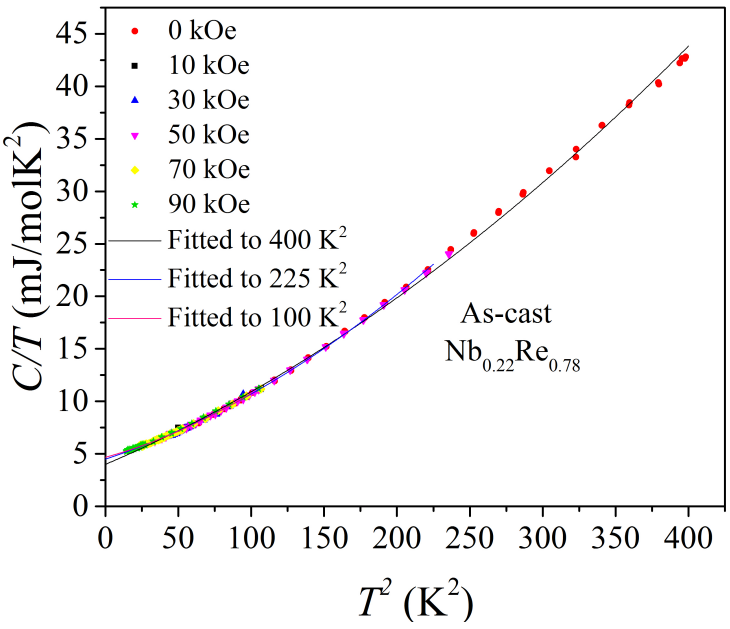

Figure 4.17: Temperature dependence of the specific heat capacity for temperatures in the range $3.8 \leq T \leq 10$ K of a polycrystalline as-cast sample of $Nb_{0.22}Re_{0.78}$ in applied fields between 0 to 90 kOe. The magenta, blue and black solid lines show the data fitted to Eq. 4.4 for $T^2 = 100$, 225 and 400 K^2.

Fitting using the full Debye expression gives a Debye temperature of 281 ± 10 K, in reasonable agreement with the values obtained from the low temperatures data discussed above. However, this fit gave a reduced γ value of 1.6 mJ/molK^2. Using the low temperature γ value and the expression

$$D_{\mathrm{C}}(E_{\mathrm{F}}) = \frac{3\gamma}{\pi^2 k_B^2}, \tag{4.5}$$

from Ref. [94] where k_{B} is the Boltzmann constant, the density of states at the Fermi energy for spin directions obtained from heat capacity measurements, $D_{\mathrm{C}}(E_{\mathrm{F}})$ was estimated and the observed values are illustrated in Table 4.6. This is also the density of states that enters the BCS equations for the transition temperature and for the BCS gap and the thermodynamic properties as a function of temperature.

From Fig. 4.16(a), the jump in the specific heat capacity was obtained as it is shown on the figure. The height of the jump was extrapolated to take into account the breadth of the transition. The jump in the specific heat capacity at the transition

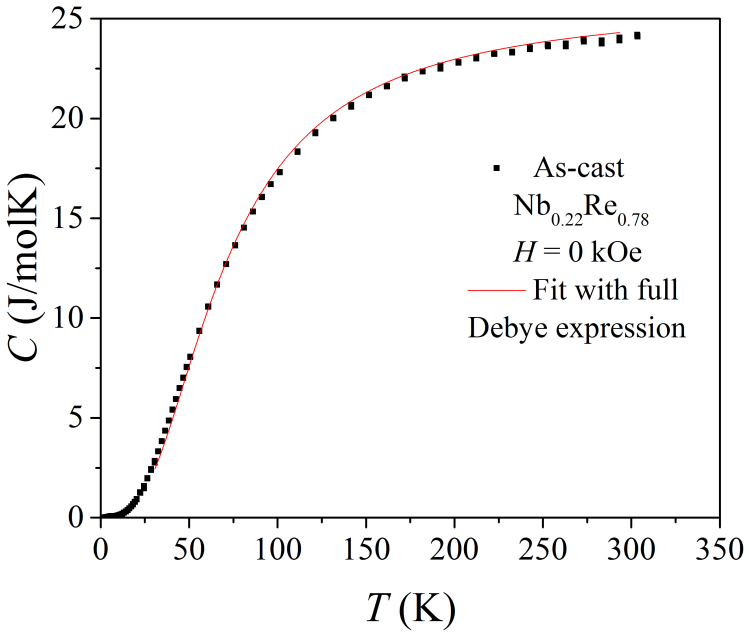

Figure 4.18: Temperature dependence of the specific heat capacity of a polycrystalline as-cast $Nb_{0.22}Re_{0.78}$ sample for $1.5 \leq T \leq 300$ K in zero magnetic field applied. The data were fitted using the full Debye expression.

in zero field applied was estimated to be between $\Delta C/T = 5.3 \pm 0.1$ mJ/molK^2 and 5.8 ± 0.1 mJ/molK^2 leading to values for $\Delta C(T_c)/\gamma T_c$ of between 1.39 ± 0.13 and 1.18 ± 0.14. The rather large spread of these values is due to the uncertainty of γ which depend on the fitting range used (400 to 225 and 100 K^2) and the estimate for the magnitude of the jump in C. Using the largest value for the jump in C and Eq. 2.31, α values were estimated to range from 1.74 ± 0.31 to 1.70 ± 0.28 which is slightly smaller than the $\alpha < \alpha_{BCS}$ value of 1.76. This means that the electron-phonon coupling strength is weaker than a conventional material. For $x = 0.18$, α was estimated to be between 1.84 and 2.04 which is slightly higher than expected for a conventional BCS material [2]. However, the reduced α values are in good agreement with those reported in Ref. [28].

The thermodynamic critical field, B_c in the α-model when temperature is zero is given by

$$B_c(0) = \sqrt{\frac{6}{\pi}}\alpha\left(\gamma_n V T_c^2\right)^{\frac{1}{2}}. \tag{4.6}$$

Fitted to T^2 (K^2)	400	225	100
γ (mJ/molK^2)	4.00 ± 0.03	4.49 ± 0.02	4.67 ± 0.03
β (mJ/molK^4)	0.06 ± 0.01	0.05 ± 0.01	0.04 ± 0.01
δ (mJ/molK^6)	$1.01 \pm 0.001 \times 10^{-4}$	$1.64 \pm 0.001 \times 10^{-4}$	$2.26 \pm 0.001 \times 10^{-4}$
Θ_D (K)	319 ± 2	339 ± 2	365 ± 3
$D_C(E_F)$ (states/eVf.u)	1.69 ± 0.02	1.90 ± 0.03	1.98 ± 0.02
$\Delta C(T_c)/\gamma T_c$ (no units) when $\Delta C/T = 4.4 \pm 0.1$ mJ/molK^2	1.10 ± 0.13	0.98 ± 0.12	0.94 ± 0.14
$\Delta C(T_c)/\gamma T_c$ (no units) when $\Delta C/T = 5.5 \pm 0.1$ mJ/molK^2	1.38 ± 0.13	1.23 ± 0.12	1.18 ± 0.13
α (no units)	1.73 ± 0.26	1.63 ± 0.24	1.60 ± 0.26
B_c (G)	1155 ± 220	1153 ± 217	1154 ± 234
l (nm)	0.69 ± 0.08	0.55 ± 0.05	0.50 ± 0.12

Table 4.6: The Sommerfeld electronic γ, the Debye T^3-law lattice β and additional δ heat capacity coefficients with measured and derived superconducting and relevant normal-state parameters for the as-cast polycrystalline $Nb_{0.22}Re_{0.78}$ sample corresponding to the data fitted at 400, 225 and 100 K^2. Θ_D: Debye temperature; $D_C(E_F)$: density of states at the Fermi velocity; ΔC: heat capacity jump at T_c; $\alpha = \Delta_0 k_B T_c$; B_c: thermodynamic critical field; l: mean free path.

where $\gamma_n V$ can be calculated using,

$$\gamma_n V = \frac{\gamma}{V_M}, \tag{4.7}$$

where V_M is the molar mass volume [73, 94]. Using Eq. 4.6 and the α values, the thermodynamic critical field, B_c was found to be 1155 ± 220, 1153 ± 217 and 1154 ± 234 G when the data fitted to 400, 225 and 100 K^2, respectively. The normal state parameters obtained from the above analysis of the specific heat capacity data for the polycrystalline as-cast $Nb_{0.22}Re_{0.78}$ sample are summarized in Table 4.6. The mean free path, l for conduction carrier scattering at low temperatures depends on the values of $D_C(E_F)$ and ρ_0 according to equation

$$l = \frac{3 m_e^2 V_{f.u}^2}{e^2 \rho_0 \pi^2 \hbar^3 D_C(E_F)^2}, \tag{4.8}$$

where $V_{f.u} = V_{cell}/2$, $\hbar = h/2\pi$ and h is the Planck's constant. Using the density of states at Fermi velocity, $D_C(E_F)$ and the resistivity values at $T = 0$, ρ_0 the mean free path l was calculated and its values vary between 0.69 ± 0.08 to 0.50 ± 0.12 nm (see Table 4.6).

The specific heat capacity data below T_c were forced to fit a simple single isotropic gap BCS model. The energy gap is given by Eq. 2.21. The entropy of the superconducting state is then calculated using Eq. 2.29. Finally, the electronic contribution

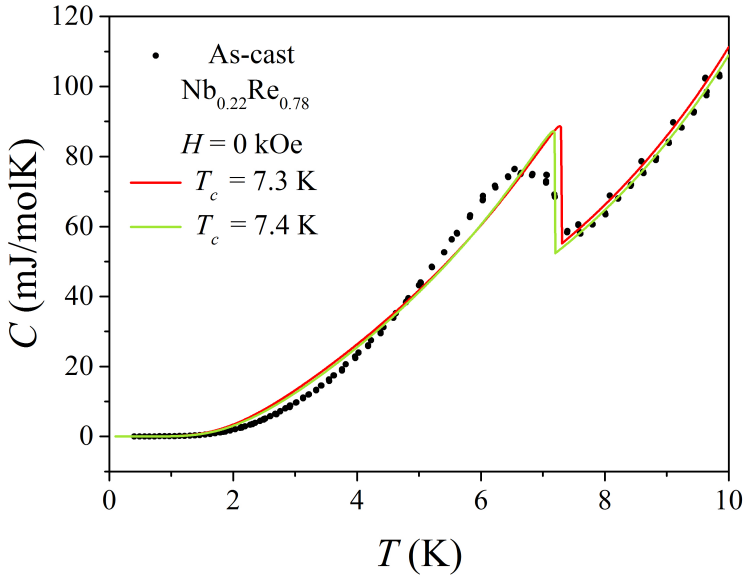

Figure 4.19: Temperature dependence of the specific heat capacity of a polycrystalline as-cast $Nb_{0.22}Re_{0.78}$ sample for $0 \leq T \leq 10$ K in zero magnetic field applied. The data were forced to fit the a simple single isotropic gap BCS model. The green line shows the fitting using γ, β and δ values obtained from the normal state data between 10 K and T_c. The red line shows the fitting using a sightly reduced value for T_c of 7.3 K.

to the heat capacity is derived using Eq. 2.30. Fig. 4.19 shows the fits to a simple single isotropic gap BCS model for the data collected in zero applied field. In this work, the heat capacity was fitted firstly using the γ, β and δ values obtained from the normal state data between 10 K and T_c (green line on Fig. 4.19). A slightly reduced value for T_c of 7.3 K was used to try to take into account the breadth of the transition (red line on Fig. 4.19). This led to a BCS parameter of 1.46 ± 0.02. If we allow the parameters γ, β, δ and T_c to vary the BCS parameter increases to 1.53 ± 0.02 but T_c is reduced to 7.2 K and δ to $1.20 \pm 0.01 \times 10^{-4}$ mJ/mol[6]. In both cases, there is a significant differences between the data and a single gap model which merit further investigation. The deviation maybe due to small deviations from the single gap BCS model.

Previous work by Smidman on $x = 0.18$ sample, revealed that this composition follows the expected behaviour for a simple BCS model [2]. However, this fitting required a small background term to be included to take account of a non-superconducting fraction of around 0.3%. Chen *et al.* also reported that $C(T)$ can

be nicely described by the one gap BCS model where $\Delta_0 = 1.93T_c$. They showed that the temperature dependence of the penetration depth, $\Delta\lambda(T)$ and the superfluid density $\rho_s(T)$ are also consistent with the BCS model. However, they only confirmed this behaviour for the $Nb_{0.18}Re_{0.82}$ composition and it is clear from their work that the temperature dependence of the heat capacity below T_c for compositions with higher Niobium content also differ from a simple BCS model.

Chapter 5

Conclusions and future work

5.1 Summary and conclusions

Unconventional superconductivity has been observed in different classes of compounds and intense studies of these materials have been carried out. Non-centrosymmetric superconductors are possible candidates for studying unconventional superconductivity. Non-centrosymmetric superconductors exhibiting mixed parity pairing are interesting system to study because in the superconducting state, an admixture of spin singlet or triplet pairing may exist. There has been particular focus on non-centrosymmetric superconductors in Niobium-Rhenium system. These compounds appear to be conventional type-II superconductors. This thesis presents magnetic, thermal and transport superconducting properties of several non-centrosymmetric compositions in Nb_xRe_{1-x} for $0.22 \leq x \leq 0.34$.

In Chapter 4, polycrystalline annealed and as-cast samples of the non-centrosymmetric compositions of Nb_xRe_{1-x} when $x = 0.22$, 0.29 and 0.34, were studied. The compositions were characterised using composition analysis (EDAX). From the measurements collected, it is obvious that the polycrystalline annealed and as-cast samples of compositions $Nb_{0.22}Re_{0.78}$, $Nb_{0.29}Re_{0.71}$ and $Nb_{0.34}Re_{0.66}$ were formed with the correct stoichiometry. The structure of the as-cast polycrystalline $Nb_{0.22}Re_{0.78}$ sample was investigated using powder x-ray diffraction (XRD) in order to observe the lattice parameter of the compound. Using the space group of this composition which is $I\bar{4}3m$ (No. 217) and the wavelength of K_α radiation, the experimental data were analysed by profile matching method. The analysis confirmed the sample has a single phase with a cubic α-Mn structure. The lattice parameter calculated from peak position is 9.67 ± 0.01 Å which agrees with the value 9.65 ± 0.01 Å cited in literature [28].

Magnetic susceptibility measurements were made using a SQUID magnetometer in order to identify the nature of superconducting phase transitions. For polycrystalline annealed and as-cast $Nb_{0.22}Re_{0.78}$ samples, the transition temperature is 7.5 ± 0.2 K, while for the polycrystalline as-cast $Nb_{0.29}Re_{0.71}$ and $Nb_{0.34}Re_{0.66}$, the transition temperatures were found to be 5.1 ± 0.2 and 4.2 ± 0.2 K, respectively. These values are in good agreement with the values reported in Ref. [28]. The experimental data show that as x increases, the transition temperature, (T_c) decreases with a maximum at 8.8 K for $x = 0.18$ reported to date. When the demagnetization factors applied, the annealed and as-cast polycrystalline $Nb_{0.22}Re_{0.78}$ samples showed complete flux expulsion at 1.8 K which agrees with Refs. [2, 59] while the as-cast $Nb_{0.29}Re_{0.71}$ and $Nb_{0.34}Re_{0.66}$ samples showed nearly complete flux expulsion at 1.8 K which is in good agreement with Ref. [28] (see Table 5.1).

From the field dependence curves of magnetization when low fields applied at several temperatures, the lower critical field values were extracted for each of the four compositions. The magnetization curves showed similar behaviour with the figure presented in Ref. [2]. The experimental data were fitted to the Ginzburg-Landau theory. The applied field values were corrected using demagnetization factors. When these factors applied, the annealed polycrystalline $Nb_{0.22}Re_{0.78}$ sample has greater lower critical field value at 0 K, $B_{c1}(0)$ than the value obtained for the as-cast sample. As x increases, the lower critical field at 0 K, $B_{c1}(0)$ decreases. From the fits, it is obvious that the lower critical field follows the behaviour expected for a superconductor with a single gap structure. The same statement was reported in Ref. [2]. The upper critical field values are presented in Table 5.1 and are in good agreement with the values cited in literature [2, 28, 59]. Magnetization loops as a function of field at 5, 6, 6.5 and 7 K, up to 50 kOe reveal that the magnetization becomes reversible above 5 kOe. In Ref. [2], similar magnetization loops were presented for single crystal of $Nb_{0.18}Re_{0.82}$ sample which in turn agrees with the present work.

The transition temperatures, T_c obtained from resistivity, magnetic susceptibility and magnetization measurements were in good agreement for the four polycrystalline compounds reported [28]. The transition temperature decreases as the applied field increases which shows an inverted symmetry between these two parameters. The residual resistivity ratios for the annealed and as-cast polycrystalline $Nb_{0.22}Re_{0.78}$ samples were 1.1 and 1.08, respectively. In this class of materials the residual resistivity ratio (RRR) is approximately 1 and as a result the RRR values estimated are in good agreement with the value cited in Ref. [59]. Consequently, the samples

are poor metals with a lot of disorder scattering. A calculation of orbital limiting field estimates a higher value for the upper critical field at lower temperatures. As a result, this value indicates that Pauli paramagnetic limiting appears to be reduced. The data were initially fitted to the Ginzburg-Landau theory. A good fit could not be obtained and as a result the WHH model in the presence of Pauli paramagnetic limiting when $\lambda = 0$ and $\alpha = 0$ was used. Unfortunately, a good fit could not be obtained although these theories describe one-gap type-II superconductors. This suggested that the reduction of the Pauli limiting field due to spin-orbit scattering should be considered. The maximum field which could be applied was 90 kOe. In order to determine more accurately the role of Pauli paramagnetic limiting and the suitability of the Ginzburg-Landau theory or the WHH model, it would be a good suggestion to perform measurements in higher applied fields or in single crystals. Also, the theory for limits of the upper critical field in dirty two-gap superconductors could be used to analyse the results in order to investigate which model is more suitable. Consequently, the experimental data may be analysed using a theory suitable for two-gap superconductors like the one introduced in 2007 by A. Gurevich [95]. From the above measurements, the annealed and as-cast polycrystalline Nb_xRe_{1-x} samples when $x = 0.22$, 0.29 and 0.34 were found to be type-II superconductors with $\kappa = 70 \pm 1$ (annealed $x = 0.22$), 72 ± 3 (as-cast $x = 0.22$), 66 ± 2 ($x = 0.29$) and 55 ± 3 ($x = 0.34$) which agrees with the κ values cited in Refs. [2, 28]. Table 5.1 shows the parameters evaluated for the compositions investigated in this project along with those cited for the composition $Nb_{0.18}Re_{0.82}$ in literature. It was observed that the parameters, κ. ξ and λ increase with increasing Niobium content. These values suggested that the non-centrosymmetric compositions of Nb_xRe_{1-x} for $x = 0.22$, 0.29 and 0.34 are s-wave superconductors.

The specific heat capacity of the as-cast polycrystalline $Nb_{0.22}Re_{0.78}$ sample was investigated. The onset of bulk superconductivity was observed at $T_c = 7.4 \pm 0.3$ K which agrees with magnetization and resistivity measurements. Linear behaviour is observed above the transition temperature for each of the fields applied. The γ values vary from 4.0 to around 4.7 mJ/molK^2 which are in good agreement with the value 4.6 mJ/molK^2 cited in Ref. [28]. The Debye temperature observed from the fitting of the C/T versus T data for $1.5 \leq T \leq 300$ K was found to be in reasonable agreement with the values obtained from the low temperature data. The heat capacity jump at transition temperature in zero-field applied, ΔC was not that sharp which allowed ambiguous analysis of the derived contribution in the superconducting state. The $\Delta C(T_c)/\gamma T_c$ varies between 1.38 ± 0.13 and 0.94 ± 0.14 which are smaller that the

x	0.18 (as-cast) single crystal	0.18 (as-cast) polycrystal	0.22 (annealed)	0.22 (as-cast)	0.29 (as-cast)	0.34 (as-cast)
α ($\mathring{A}$)	9.65 ± 0.07	9.65 ± 0.07	9.69 ± 0.01	9.67 ± 0.01	9.73 ± 0.01	9.76 ± 0.01
V ($\mathring{A}^3$)	899 ± 2.23	899 ± 2.23	910 ± 2.83	904 ± 2.83	920 ± 2.86	930 ± 2.89
T_c (K)	8.8 ± 0.2	8.8 ± 0.2	7.5 ± 0.2	7.5 ± 0.2	5.1 ± 0.2	4.2 ± 0.2
$4\pi\chi$ at 1.8K	-1.00 ± 0.01	-0.95 ± 0.04	-1.03 ± 0.02	-1.03 ± 0.02	-0.92 ± 0.07	-0.94 ± 0.06
$B_{c1}(0)$ (G)	55 ± 2	56 ± 1	78 ± 1	66 ± 2	47 ± 1	42 ± 1
$B_{c2}(0)$ (kG)	not reported	230 ± 2	181 ± 1	160 ± 2	97 ± 1	64 ± 2
$B_{c2}^{orb}(0)$ (kG)	148 ± 1	161 ± 2	153 ± 17	144 ± 14	88 ± 17	60 ± 10
ξ (nm)	4.00 ± 0.02	4.00 ± 0.02	4.27 ± 0.02	4.54 ± 0.06	5.83 ± 0.06	7.17 ± 0.22
κ (no units)	76 ± 1	79 ± 2	70 ± 1	72 ± 3	66 ± 2	55 ± 3
λ (nm)	304 ± 2	318 ± 2	300 ± 6	327 ± 7	383 ± 5	397 ± 4

Table 5.1: Superconducting and normal-state parameters derived using magnetization and resistivity measurements for the annealed and as-cast polycrystalline Nb_xRe_{1-x} samples when $0.22 \leq x \leq 0.34$ and the reported superconducting and normal-state parameters for the single crystal and polycrystalline $Nb_{0.18}Re_{0.82}$ samples. V: volume per unit cell, α: lattice parameter, T_c: transition temperature, $4\pi\chi$: magnetic susceptibility, $B_{c1}(0)$: lower critical field, $B_{c2}(0)$: upper critical field using Ginzburg-Landau theory, $B_{c2}^{orb}(0)$: upper critical field using WHH model simulation for $\alpha = 0$ and $\lambda = 0$, ξ: coherence length, κ: Ginzburg-Landau parameter, λ: penetration depth. The data for the single crystal composition of $Nb_{0.18}Re_{0.82}$ were reported in Ref. [2] and the data for the polycrystalline composition were reporten in Ref. [28].

BCS prediction of 1.43 [94]. It was previously reported that the $\Delta C(T_c)/\gamma T_c$ varies from 1.86 to about 0.5 for $x = 0.18$ to 0.31 and as a consequence the observed values agree with the literature. Using the largest value for the jump in specific heat capacity, α values were in the range $1.60 \leq \alpha \leq 1.73$ which are smaller that the BCS value (α_{BCS}) of 1.76 and as a result it was suggested that the electron-phonon coupling strength is weaker than a conventional material. In comparison with the conclusions made in Ref. [28], these compounds are unconventional s-wave superconductors with evidence of spin singlet pairing in spite of the heavy atomic mass of Rhenium residing on the non-centrosymmetric sites.

5.2 Future work

A research is never done until you indicate the fields that need improvements or further investigation. The presented work contains magnetization, resistivity and specific heat capacity studies of a few non-centrosymmetric polycrystalline Nb_xRe_{1-x} compounds in the range $0.22 \leq x \leq 0.34$. A comparison of the measurements collected for polycrystalline and single crystal samples would give additional information about the compounds and lead to better conclusions. Additionally, in order to investigate and check the presence of superconducting gaps, it would be a

good idea to carry out muon spectroscopy (μSR) and small angle neutron scattering (SANS) experiments.

Bibliography

[1] M. Sigrist. In *Lectures on the Physics of Highly Correlated Electron Systems IX*, volume 789, 2005.

[2] M. Smidman. *Superconducting and magnetic properties of non- centrosymmetric system.* PhD thesis, Physics Department, University of Warwick, 2013.

[3] D. V. Delft. *Physica C: Superconductivity*, 479:30, 2012.

[4] H. Frohlich. *Phys. Rev.*, 79:845, 1950.

[5] L. N. Cooper J. R. Schrieffer J. R., Bardeen. *Phys. Rev*, 106:162, 1957.

[6] E. Maxwell. *Phys.Rev.*, 78:477, 1950.

[7] B. Serin W. H. Wright L. B. Nesbitt C. A., Reynolds. *Phys. Rev.*, 78:487, 1950.

[8] L. N. Cooper J. R. Schrieffer J. R., Bardeen. *Phys. Rev.*, 108:1175, 1957.

[9] D. Pines. *Phys. Rev.*, 109:280, 1958.

[10] B. T. Matthias et al. *J. Phys. Chem. Solids*, 19:130, 1961.

[11] V. B. Compton B. T. Matthias and E. Corenzwit. *J. Phys. Chem. Solids*, 19: 130, 1961.

[12] K. H. Bennemann and J. B. Ketterson. In K. H. Bennemann and J. B. Ketterson, editors, *Superconductivity: Conventional and Unconventional Superconductors*, chapter 1. Springer Berlin Heidelberg, 2008.

[13] M. Cyrot and D. Pavuna. *Introduction to Superconductivity and High-T_c materials.* World Scientific Publishing, Singapore, 2010.

[14] M. R. Norman. *e-prints, arXiv:1302.3176.*

[15] A. B. Migdal. *Sov. Phys. JETP*, 34:996, 1958.

[16] L. N. Cooper. *Phys. Rev.*, 104:1189, 1956.

[17] M. R. Schafroth. *Phys. Rev.*, 100:463, 1955.

[18] P. Morel and P. W. Anderson. *Phys. Rev.*, 125:1263, 1962.

[19] R. Balian and N. R. Werthamer. *Phys. Rev.*, 131, 1963.

[20] J. R. Schrieffer, D. J. Scalapino, and J. W. Wilkins. *Phys. Rev. Lett.*, 10:336, 1963.

[21] W. L. McMillan and J. M. Rowell. *Phys. Rev. Lett.*, 14:108, 1965.

[22] W. L. McMillan. *Phys. Rev.*, 167:331, 1968.

[23] J. G. Bednorz and K. A. Müller. *Z. Phys. B*, 64:189, 1986.

[24] D. J. Scalapino. *Phys. Rep.*, 250:329–365, 1995.

[25] N. P. Armitage, P. Fournier, and R. L. Greene. *Rev. Mod. Phys.*, 82:2421, 2010.

[26] Y. Sungkit. *Ann. Rev. Condens. Matter Phys.*, 5:15, 2014.

[27] R. P. Singh, M. Smidman, M. R. Lees, D. McK Paul, and G. Balakrishnan. *J. Cryst. Growth*, 361:129, 2012.

[28] J. Chen, L. Jiao, J. L. Zhang, Y. Chen, L. Yang, M. Nicklas, F. Steglich, and H. Q. Yuan. *Phys. Rev. B*, 88:144510, 2013.

[29] C. S. Lue, T. H. Su, H. F. Liu, and B. L. Young. *Phys. Rev. B*, 84:052509, 2011.

[30] E. Bauer and M. Sigrist. *Non-Centrosymmetric Superconductors: Introduction and Overview*, volume 847. Springer-Verlag Berlin Heidelberg, 2012.

[31] Z. Fiskt, J. L. Sarraot, J. L. Smitht, and J. D. Thompsonx. *Proc. Natl. Acad. Sci.*, 92:6663, 1995.

[32] S. Uji T. Sugawara N. Kimura H. Aoki T. Terashima, M. Kimata and H. Harima. *Phys Rev. B*, 78:205107, 2008.

[33] S. Fujimoto. *J. Phys. Soc. Jp.*, 75:083704, 2006.

[34] S. Fujimoto. *J. Phys. Soc. Jp.*, 76:051008, 2007.

[35] H. Takeya, M. ElMassalami, S. Kasahara, and K. Hirata. *Phys. Rev. B*, 76: 104506, 2007.

[36] H. Q. Yuan, D. F. Agterberg, N. Hayashi, P. Badica, D. Vandervelde, K. Togano, M. Sigrist, and M. B. Salamon. *Phys. Rev. Lett.*, 97:017006, 2006.

[37] W. H. Lee, H. K. Zeng, Y. D. Yao, and Y. Y. Chen. *Physica C: Superconductivity*, 266:138, 1996.

[38] I. Bonalde, R. L. Ribeiro, K. J. Syu, H. H. Sung, and W. H. Lee. *New J. Phys.*, 13:123022, 2011.

[39] J. Chen, L. Jiao, J. L. Zhang, Y. Chen, L. Yang, M. Nicklas, F. Steglich, and H. Q. Yuan. *New J. Phys.*, 15:053005, 2013.

[40] J. Chen and H. Q. Yuan. *J. Phys.: Conf. Ser.*, 400:022010, 2012.

[41] R. L. Ribeiro, I. Bonalde, Y. Haga, R. Settai, and Y. Onuki. *J. Phys. Soc. Jp.*, 78:115002, 2009.

[42] P. K. Biswas, M. R. Lees, A. D. Hillier, R. I. Smith, W. G. Marshall, and D. McK. Paul. *Phys. Rev. B*, 84:184529, 2011.

[43] C. S. Lue, H. F. Liu, C. N. Kuo, P. S. Shih, J. Y. Lin, Y. K. Kuo, M. W. Chu, T. L. Hung, and Y. Y. Chen. *Supercond. Sci. Technol.*, 26:055011, 2013.

[44] T. Shibayama, M. Nohara, H. A. Katori, Y. Okamoto, Z. Hiroi, and H. Takagi. *J. Phys. Soc. Jp.*, 76:073708, 2007.

[45] K. Wakui, S. Akutagawa, N. Kase, K. Kawashima, T. Muranaka, Y. Iwahori, J. Abe, and J. Akimitsu. *J. Phys. Soc. Jp*, 78:034710, 2009.

[46] K. Miliyanchuk, F. Kneidinger, C. Blaas-Schenner, D. Reith, R. Podloucky, P. Rogl, T. Khan, L. Salamakha, G. Hilscher, H. Michor, E. Bauer, and A. D. Hillier. *J. Phys.: Conf. Series*, 273:012078, 2011.

[47] E. Bauer, R. T. Khan, H. Michor, E. Royanian, A. Grytsiv, N. Melnychenko-Koblyuk, P. Rogl, D. Reith, R. Podloucky, E.-W. Scheidt, W. Wolf, and M. Marsman. *Phys. Rev. B*, 80:064504, 2009.

[48] G. Eguchi, D. C. Peets, M. Kriener, Y. Maeno, E. Nishibori, Y. Kumazawa, K. Banno, S. Maki, and H. Sawa. *Phys. Rev. B*, 83:024512, 2011.

[49] Y. Okuda, Y. Miyauchi, Y. Ida, Y. Takeda, C. Tonohiro, Y. Oduchi, T. Yamada, N. D. Dung, T. D. Matsuda, Y. Haga, T. Takeuchi, M. Hagiwara, K. Kindo, H. Harima, K. Sugiyama, R. Settai, and Y. Onuki. *J. Phys. Soc. Jp.*, 76:044708, 2007.

[50] R. P. Singh, A. D. Hillier, B. Mazidian, J. Quintanilla, J. F. Annet, D. McK Paul, G. Balakrishnan, and M. R. Lees. *Phys. Rev. Lett.*, 112:107002, 2014.

[51] J. Quintanilla, A. D. Hillier, J. F. Annett, and R. Cywinski. *Phys. Rev. B*, 82: 174511, 2010.

[52] J. A. T. Barker, D. Singh, A. Thamizhavel, A. D. Hillier, M. R. Lees, G. Balakrishnan, D. McK. Paul, and Singh R. P. *Phys. Rev. Lett.*, 115:267001, 2015.

[53] M. Sigrist. *AIP Conf. Proc.*, 789:165, 2005.

[54] A. D. Hillier, J. Quintanilla, and R. Cywinski. *Phys. Rev. Lett.*, 102:117007, 2009.

[55] D. Pines. *Phys. Rev.*, 109:280, 1958.

[56] A. G. Knapton. *J. Less-Common Met.*, 1:480, 1959.

[57] A. Westgren and G. Phragmen. *Ztschr. Physik.*, 33:777, 1925.

[58] J. Thewlis A. J. Bradley. *R. Soc. London*, 1:456, 1927.

[59] A. B. Karki, Y. M. Xiong, N. Haldolaarachchige, S. Stadler, I. Vekhter, P. W. Adams, D. P. Young, W. A. Phelan, and Julia Y. Chan. *Phys. Rev. B*, 83: 144525, 2011.

[60] J. G. Daunt and T. S. Smith. *Phys. Rev.*, 88:309, 1952.

[61] C. Cirillo, R. Fittipaldi, M. Smidman, G. Carapella, C. Attanasio, A. Vecchione, R. P. Singh, M. R. Lees, G. Balakrishnan, and M. Cuoco. *Phys. Rev. B*, 91: 134508, 2015.

[62] J. R. Bardeen. *Phys. Rev.*, 97:1724, 1955.

[63] E. H. Brandt. *Physica C: Superconductivity*, 404:74, 2004.

[64] F. and H. London. *R. Soc. London*, 149:71, 1935.

[65] S. Blundell. *Magnetism in Condensed Matter*. Oxford Univ. Press, 2001.

[66] J. R. Waldram. *Superconductiviy of Metals and Cuprates*. Institute of Physics Publishing, Boston, 1996.

[67] M. Tinkham. *Introduction to Superconductivity*. McGraw-Hill, New York, 2nd edition, 1996.

[68] V. Moshchalkov, M. Menghini, T. Nishio, Q. H. Chen, A. V. Silhanek, V. H. Dao, L. F. Chibotaru, N. D. Zhigadlo, and J. Karpinski. *Phys. Rev. Lett.*, 102: 117001, 2009.

[69] A. Aharoni. *J. Appl. Phys.*, 83:3432, 1998.

[70] W. H. Kleiner, L. M. Roth, and S. H. Autler. *Phys Rev.*, 133:A1226, 1964.

[71] A. A. Abrikosov. *Sov. Phys. JETP*, 5:1174, 1957.

[72] H. A. Farach C. P. Poole, Jr. and R. J. Creswick. *Superconductivity.* Academic Press, San Diego, CA, 1995.

[73] G. Balakrishnan, L. Bawden, S. Cavendish, and M. R. Lees, 2013.

[74] L. P. Gor'kov. *Sov. Phys. JETP*, 36(6):1364, 1959.

[75] L. P. Lévy. *Magnetism and Superconductivity.* Springer Science & Business Media, 2013.

[76] L. N. Cooper. *Phys. Rev.*, 104:1189, 1956.

[77] A. Carrington and F. Manzano. *Physica C: Superconductivity*, 385:205, 2003.

[78] C. J. David. *Supercond. Sci. Technol.*, 26:115011, 2013.

[79] W. L. McMillan. *Phys. Rev.*, 167:331, 1968.

[80] A. P. Mackenzie and Y. Maeno. *Physica B: Condensed Matter*, 280:2148, 2000.

[81] C. C. Tsuei and J. R. Kirtley. *Rev. Mod. Phys.*, 72:969, 2000.

[82] M. Sigrist, D. Agterberg, P. Frigeri, N. Hayashi, R. Kaur, A. Koga, I. Milat, K. Wakebayashi, and Y. Yanase. *J. Magn. Matter.*, 310:536, 2007.

[83] F. Bouquet, Y. Wang, R. A Fisher, D. G. Hinks, J. D. Jorgensen, A. Junod, and N. E. Phillips. *Europhys. Lett.*, 56:856, 2001.

[84] D. C. Johnston. *Supercond. Sci. Technol.*, 26:115011, 2013.

[85] E. Helfand and N. R. Werthamer. *Phys. Rev. Lett.*, 13:686, 1964.

[86] N. R. Werthamer, E. Helfand, and P. C. Hohenberg. *Phys. Rev.*, 147:295, 1966.

[87] Quantum Design. *MPMS MultiVu Application User's Manual.* Quantum Design, San Diego, USA, 2004.

[88] Quantum Design. *PPMS Manual*, 11, 1999.

[89] J. G. Daunt and T. S. Smith. *Phys. Rev.*, 88:309–311, 1952.

[90] R. A. Klemm and J. R. Clem. *Phys. Rev. B*, 21:1868, 1980.

[91] D. Singh, A. D. Hillier, A. Thamizhavel, and R. P. Singh. *Phys. Rev. B*, 94: 054515, 2016.

[92] Y. Kagan and V. N. Flerov. *Sov. Phys. JETP*, 39:673, 1974.

[93] W. F. Meggers, A. S. King, and R. F. Bacher. *Phys. Rev.*, 38:1258, 1931.

[94] V. K. Anand, H. Kim, M. A. Tanatar, R. Prozorov, and D. C. Johnston. *Phys. Rev. B*, 87:224510, 2013.

[95] A. Gurevich. *Physica C: Superconductivity*, 456:160, 2007.